The Molecular Weight Effects of Poly(acrylic acid) on Calcium Carbonate Inhibition in the Kraft Pulping Process

A DISSERTATION
SUBMITTED TO THE FACULTY OF THE GRADUATE SCHOOL
OF THE UNIVERSITY OF MINNESOTA
BY

Matthew Richard Dubay

IN PARTIAL FULFILLMENT OF THE REQUIREMENTS
FOR THE DEGREE OF
DOCTOR OF PHILOSOPHY

Steven J. Severtson, Advisor

May, 2011

© Matthew R. Dubay 2011

Acknowledgements

First and foremost, I want to thank the Creator, my Savior, and the Comforter for their priceless influences on my life.

Also, I hold an enormous amount of gratitude and respect for all of the people responsible for helping and guiding me as a graduate student. In particular, I would like to sincerely thank Dr. Steve Severtson for his seemingly unending supply of experiential wisdom and genuine concern for my progress not only as a student but also as a teacher, independent researcher, and leader. Beyond the classroom, he has been my mentor (and friend) in innumerable ways. All the members of his research group have been instrumental in my success as a graduate student –especially Dr. Gang Pu for the massive amount of time he generously donated while helping me organize this thesis and Dr. Jiguang Zhang for his help and guidance with polymerization techniques.

I would also like to thank Dr. Andreas Stein and his group members (particularly Melissa Fierke) for their continual support and help with many of the issues that sprung up during this research. The other members of my thesis committee, Dr. William Tze and Dr. Shri Ramaswamy, were instrumental in their support and review of this thesis, of which I am grateful for. In addition, I would like to acknowledge Kemira Chemicals, Inc. for providing financial support.

I would also like to mention that I never would have pursued this degree in the first place without the initial encouragement of William Hintze. Also, he generously opened his doors to me and even after my acceptance into graduate school, he and his entire family have supported me and provided not just a house to go to after work, but a *home*. I can not thank them enough for their love and support.

Dedication

This Ph. D. thesis is dedicated to my parents and sisters for their unending love, support, and prayers throughout all the seasons of my life and particularly during my graduate school career.

Abstract

Calcium carbonate scale reduces process efficiency and control in kraft pulping operations. The formation of scale can be alleviated or at least reduced by the addition of antiscalant chemicals into the process line. A number of different antiscalants are commercially available but still little is known about their mechanism of inhibiting scale formation. This project focused on one class of antiscalants, the polymeric antiscalants, which are carboxylic acid containing copolymers, with the majority of their monomer residues being poly(acrylic acid). Scale inhibition performance at high pH and temperatures was characterized using a number of different experimental setups and the mechanisms involved were investigated.

Performance tests yielded that the most influential characteristic of the polymeric antiscalants was the molecular weight (MW), and consequently, the molecular weight distribution (MWD) of the polymer species. Since commercial poly(acrylic acid) (PAA) samples have a broad MWD, atom transfer radical polymerization (ATRP) was utilized to create relatively monodisperse samples of PAA. These PAA samples synthesized via ATRP were used to investigate the effects of MW and MWD on antiscalant performance along with the mechanisms responsible for the observed optimal MW range of ~10,000 under laboratory kraft pulping conditions. The information presented here is useful both in identifying important properties of polymeric antiscalants and in understanding the mechanisms by which they inhibit the formation of calcium carbonate crystalline deposits in kraft pulping.

Table of Contents

Acknowledgements i
Dedication ii
Abstract iii
Table of Contents iv
List of Tables vi
List of Figures vii
List of Schemes xii
List of Abbreviations xiii
Chapter 1 - Introduction 1
History 1
Industry nomenclature 3
Stoichiometric-based classification 4
Small molecule antiscalant adsorption 6
Figures 11
Chapter 2 – Testing of Currently Available Antiscalants 14
Introduction 14
Materials and Methods 17
Chemicals and Materials 17
Laboratory Kraft Digester 17
Parr Bomb Reactions 18
Temperature degradation 19
Results & Discussion 21
Laboratory Kraft Digester 21
Parr Bomb Reactor 26
Degradation 31
Conclusions 33
Tables 34
Figures 35
Chapter 3 – Commercial PAA Inhibition of $CaCO_3$ 47
Introduction 47
Materials and Methods 48
Chemicals and Materials 48
Solutions 49
Experimental setup 49
Results & Discussion 49
Particle concentration 51
CLD analysis 53
Conclusions 60
Tables 62
Figures 63
Chapter 4 – Synthesis of Relatively Monodisperse PAA 80

Introduction 80
Materials and Methods 82
Chemicals and Materials 82
Equipment 82
Experimental setup 82
Results & Discussion 84
Synthesis of low PDI ATRP Poly(*tert*-butyl acrylate) 84
Synthesis of low PDI PAA via the hydrolysis of PtBA 85
Conclusions 89
Tables 91
Schemes 92
Figures 94
Chapter 5 – Adsorption of PAA onto Calcite 99
Introduction 99
Materials and Methods 100
Chemicals and Materials 100
Experimental 101
Equipment 101
Results & Discussion 102
Conclusions 110
Figures 112
Chapter 6 - Inhibition of $CaCO_3$ Formation by Monodisperse PAA 123
Introduction 123
Materials and Methods 125
Chemicals and Materials 125
Solutions 125
Experimental setup 126
Results & Discussion 127
Critical Ca^{2+} Determination & Analysis 127
Post-nucleation Results & Discussion 131
Conclusions 140
Figures 141
Chapter 7 – Final Conclusions and Future Work 155
Summary 155
Future work 157
Bibliography 159

List of Tables

Page 34.....**Table 1.1** Listing of the sample compositions, weight average molecular weights, and kraft digester and Parr reactor results (for 10 ppm dosages).

Page 62.....**Table 3.1** The number and weight average molecular weights along with the polydispersity indices (PDIs) of the PAA and Na-PAA samples as measured via SEC.

Page 91.....**Table 4.1** List of ingredients for the various degrees of polymerization (DP) of PtBA samples synthesized via ATRP. Molar ratios were calculated using *x*:1:1:0.05:1.05 (tBA:MBP:CuBr:$CuBr_2$:PMDETA) with *x* representing the degree of polymerization (DP).

Page 91.....**Table 4.2** Synthesized PAA samples via the hydrolysis of ATRP PtBA with TFA/DCM with molecular weight averages characterized via NMR and SEC.

List of Figures

Page 11.....**Figure 1.1** A schematic outline of the chemical recovery process involved in the kraft pulping process.

Page 12.....**Figure 1.2** A schematic outline depicting the various phases of scale formation along with how antiscalants can prevent the system from progressing forward towards deposition.

Page 13.....**Figure 1.3** Chemical structures of four common antiscalants.

Page 35.....**Figure 2.1** Solubility curves for calcite at various temperatures pertinent to the kraft pulping process.

Page 36.....**Figure 2.2** Total, dissolved, and suspended calcium levels in a typical control kraft digestion experiment (with no inhibitor).

Page 37.....**Figure 2.3** Solubility curves alongside kraft digester nucleation points at various temperatures.

Page 38.....**Figure 2.4** Solution concentrations of dissolved Ca^{2+} during a kraft cook experiment with varying concentrations of EDTA used to inhibit $CaCO_3$ precipitation.

Page 39.....**Figure 2.5** The direct correlation between the molar concentrations of residual Ca^{2+} left in kraft liquor after digestion and the concentration of EDTA added before digestion.

Page 40.....**Figure 2.6** Solution concentrations of Ca^{2+} during a kraft cook experiment with varying concentrations of the industry benchmark, C-24, used to inhibit $CaCO_3$ precipitation.

Page 41.....**Figure 2.7** Correlation between kraft digester Ca^{2+} fitting constants kA and c_∞ with respect to the molecular weight (M_w) of commercial samples tested at 10 mg/L.

Page 42.....**Figure 2.8** Total, dissolved, and suspended calcium levels in a typical Parr reactor experiment (with no inhibitor).

Page 43.....**Figure 2.9** Dissolved calcium as a function of time/temperature in a Parr reactor experiment with various concentrations of C-20. Non-linear fits based on a 2^{nd} order rate law for crystal growth with a temperature dependent rate constant were used to determine nucleation points.

Page 44.....**Figure 2.10** Nucleation temperatures and residual calcium amounts at 150 °C relative to the molecular weight of the inhibitor used.

Page 45.....**Figure 2.11** The slight change in the molecular weight distribution of ~20,000 MW Na-PAA before and after degradation under kraft-like

conditions and the drastic degradation of ~90,000 MW PAA in more moderate conditions.

Page 46.....**Figure 2.12** The change in M_w for the 90,000 MW PAA and 20,000 MW Na-PAA samples with respect to degradation time in pH 7 solution void of sulfide and kraft-like conditions and the nucleation temperatures when the degraded samples were used in $CaCO_3$ inhibition studies.

Page 63.....**Figure 3.1** Schematic representation of an FBRM probe and how it determines measures the different chord lengths of particles.

Page 64.....**Figure 3.2** A typical plot of $CaCO_3$ particle count as monitored by FBRM with respect to the formal calcium concentration of the solution.

Page 65.....**Figure 3.3** The solubility of $CaCO_3$ (calcite phase) at various temperatures along with the critical points where $CaCO_3$ precipitation occurs at 25 °C and pH of 12.

Page 66.....**Figure 3.4** Total chord length counts via FBRM for $CaCO_3$ crystals at various temperatures as Ca^{2+} solution was added to a $NaCO_3$ and NaOH (pH ~12) solution.

Page 67.....**Figure 3.5** The linear dependence of $T^{-3/2}$ upon the natural logarithm of $[Ca^{2+}][CO_3^{2-}]$.

Page 68.....**Figure 3.6** Molecular weight distributions of commercially available poly(acrylic acid) and sodium polyacrylate samples.

Page 69.....**Figure 3.7** showing the curves produced by summing all chord length counts from FBRM for varying concentrations of 10k-Na-PAA.

Page 70.....**Figure 3.8** The critical calcium concentrations for various MW PAA samples with respect to their initial dosages as determined via FBRM total chord length counts.

Page 71.....**Figure 3.9** The critical calcium concentrations for various MW Na-PAA samples with respect to their initial dosages as determined via FBRM total chord length counts.

Page 72.....**Figure 3.10** The molecular weight dependence of PAA and Na-PAA samples upon the critical calcium concentration for FBRM experiments.

Page 73.....**Figure 3.11** Crystal growth experiment employing 20 mg/L of 10k-Na-PAA showing FBRM chord length histograms over time.

Page 74.....**Figure 3.12** Crystal growth experiment employing 5 mg/L of 10k-Na-PAA showing FBRM chord length histograms over time.

Page 75.....**Figure 3.13** Chord length distributions at the critical points for initial 10k-Na-PAA concentrations of 5 mg/L and 20 mg/L.

Page 76.....**Figure 3.14** The MWDs of 5k-PAA and 90k-PAA samples and the calculated MWDs of their various mixtures at quarter mass fraction intervals and the critical calcium levels when implementing these various mixtures at a total initial concentration of 10 mg/L.

Page 77.....**Figure 3.15** SEM images of $CaCO_3$ particles after 1 hour when precipitated from supersaturated solutions containing a range of 5k and 90k PAA mixtures as the inhibitor.

Page 78.....**Figure 3.16** SEM images of $CaCO_3$ particles after 2 hours when precipitated from supersaturated solutions containing a range of 5k and 90k PAA mixtures as the inhibitor.

Page 79.....**Figure 3.17** SEM images of $CaCO_3$ particles after 2½ hours when precipitated from supersaturated solutions containing a range of 5k and 90k PAA mixtures as the inhibitor.

Page 94.....**Figure 4.1** ^1H NMR spectra showing the progress of a second hydrolysis of the 500 DP ATRP PtBA sample with TFA.

Page 95.....**Figure 4.2** The calculated % conversion of *t*-butyl acrylate mers to acrylic acid mers during the 2nd hydrolysis of a ~500 DP ATRP PtBA sample along with the number average molecular weights of the samples.

Page 96.....**Figure 4.3** NMR spectra showing the progressive conversion of 500 DP ATRP PtBA to PAA via the hydrolysis of the t-butyl acrylate groups.

Page 97.....**Figure 4.4** NMR spectra for some of the PAA samples hydrolyzed from ATRP synthesized PtBA samples.

Page 98.....**Figure 4.5** Molecular weight distributions of poly(acrylic acid) samples prepared via the hydrolysis of ATRP synthesized poly(*tert*-butyl acrylate) alongside the commercially prepared 20k-Na-PAA sample.

Page 112....**Figure 5.1** Molecular weight distributions of PAA and Na-PAA samples synthesized using various techniques.

Page 113....**Figure 5.2** SEC UV detector response showing the amount and MWD of 20k-Na-PAA sample before and after adsorption to calcite at pH 12 for 24 hours.

Page 114....**Figure 5.3** Calibration line using the UV absorbance of 20k-Na-PAA concentration with respect to area under the SEC elution curve.

Page 115....**Figure 5.4** Single day adsorption isotherms of Na-PAA and PAA from various sources onto calcite at pH 12.

Page 116....**Figure 5.5** Adsorption rates of various PAA samples.

Page 117....**Figure 5.6** Individual isotherms at various sample times for the polydisperse mixture of ATRP PAA samples.

Page 118....**Figure 5.7** SEC spectra of solution phase PAA (mixture of four ATRP PAA samples) for the isotherm slurry with initial concentration at ~175 mg/L as adsorption time increases.

Page 119....**Figure 5.8** SEC spectra of solution phase PAA (mixture of four ATRP PAA samples) for the isotherm slurry with initial concentration at ~300 mg/L as adsorption time increases.

Page 120....**Figure 5.9** Relative solution concentrations (along with their logarithmic fits) of the four major mass fractions with respect to adsorption time.

Page 121....**Figure 5.10** The relative PAA molecules in solution after 4 days of adsorption according to experimental data and theoretical extrapolation based on the initial 3 hours adsorption.

Page 122....**Figure 5.11** Schematic representation of PAA adsorption and conformation at the pH 12 calcite surface.

Page 141....**Figure 6.1** Schematic of modular quartz crystal microbalance system built.

Page 142....**Figure 6.2** Diagram of quartz crystal microbalance mechanism.

Page 143....**Figure 6.3** A typical plot of $CaCO_3$ growth on the Au coated QCM crystal and particle count as monitored by FBRM with respect to the formal calcium concentration of the solution.

Page 144....**Figure 6.4** $CaCO_3$ scale inhibition performance curves for varying initial concentrations of 3,400 M_w ATRP PAA via FBRM and QCM monitoring techniques.

Page 145....**Figure 6.5** Critical calcium levels (as determined via FBRM) relative to the initial polymer concentration for the lower MW PAA and Na-PAA low PDI samples.

Page 146....**Figure 6.6** Critical calcium levels (as determined via FBRM) relative to the initial polymer concentration for the higher MW ATRP PAA (low PDI) samples.

Page 147....**Figure 6.7** Efficacies of the various low PDI PAA/Na-PAA antiscalants in FBRM experiments.

Page 148....**Figure 6.8** FBRM collected CLDs during crystallization experiment using 75,000 M_w ATRP PAA at 10 ppm as inhibitor.

Page 149....**Figure 6.9** The FBRM total chord length counts/sec and QCM thickness during crystallization experiment using 75,000 M_w ATRP PAA at 10 ppm as inhibitor.

Page 150....**Figure 6.10** Dose-performance curves for ATRP PAA mixtures, their components, and the referenced commercial ~20k Na-PAA sample.

Page 151....**Figure 6.11** Dissolved Ca^{2+} concentration as determined via the ISE probe in a crystal growth experiment using 8ppm of 50:50 3,400:75,000 M_w ATRP PAA mixture as inhibitor.

Page 152....**Figure 6.12** Dissolved PAA concentrations as determined via SEC in a crystal growth experiment using 8ppm of 50:50 3,400:75,000 M_w ATRP PAA mixture as inhibitor.

Page 153....**Figure 6.13** SEM images of $CaCO_3$ crystals present at various Ca^{2+} formal concentrations from Figures 6.12 & 6.13.

Page 154....**Figure 6.14** Proposed schematic of nucleation and growth of calcite phase at the expense of the ACC phase.

List of Schemes

Page 92.....**Scheme 4.1** The Atom Transfer Radical Polymerization (ATRP) of poly(*tert*-butyl acrylate).

Page 93.....**Scheme 4.2** Hydrolysis scheme for the conversion of PtBA to PAA. Possible effect of moisture creating *t*-butanol is also shown.

List of Abbreviations

AA ..... atomic absorbance
ACC ..... amorphous calcium carbonate
ACC/PAA ..... poly(acrylic acid) stabilized amorphous calcium carbonate
ATRP ..... atom transfer radical polymerization
BET ..... Brunauer-Emmett-Teller
CD ..... charge density
CLD ..... chord length distribution
DCM ..... dichloromethane
DDI ..... doubly de-ionized
DP ..... degree of polymerization
DMM ..... digital multimeter
EDTA ..... ethylenediaminetetraacetic acid
FBRM ..... focused beam reflectance measurement
IC ..... integrated circuit
ISE ..... ion selective electrode
LMW ..... low molecular weight
MBP ..... methyl 2-bromopropionate
M_n ..... number-average molecular weight
MW ..... molecular weight
M_w ..... weight-average molecular weight
MWD ..... molecular weight distribution
Na-PAA ..... sodium polyacrylate
NMR ..... nuclear magnetic resonance
PAA ..... poly(acrylic acid)
PDI ..... polydispersity index
PMA ..... poly(maleic acid)
PMDETA ..... N,N,N',N',N''-pentamethyldietheylentriamine
PSD ..... particle size distribution
PtBA ..... poly(*tert*-butyl acrylate)
QCM ..... quartz crystal microbalance
RAFT ..... reversible addition fragmentation transfer
rms ..... root-mean-square
SEC ..... size exclusion chromatography
SEM ..... scanning electron microscope
tBA ..... *tert*-butyl acrylate
TFA ..... trifluoroacetic acid
UV ..... ultraviolet
XRD ..... x-ray diffraction

Chapter 1 - Introduction

History

The kraft pulping process was first developed and implemented in Europe during the later part of the 19th century. It made its way to North America by the first decade of the 20th century. Since the 1940's, it has surpassed sulfite pulping methods and by 1989, 78% of wood pulp came from the kraft pulping process.[1,2] Today, the kraft pulping process is still the dominant method used to produce paper-making fibers. Among the many advantages of the kraft process are the increased fiber strength, fiber length, and cellulose content of its resulting fibers along with the ability to reuse up to 98% of the cooking chemicals through the alkaline recovery process as outlined in Figure 1.1. Although, with any established industrial process, there are always some nagging concerns to be addressed in order to make the process more efficient, less costly, or more environmentally healthy.

In the case of kraft mills, the deposition of unwanted scale in undesirable locations remains a concern for those engineers responsible for keeping the process efficient and profitable. Calcium carbonate deposits remain as a particular frequent problem when forming on heat exchange surfaces of the digester and liquor evaporators.[3-8] Due to the inverse relationship between temperature and $CaCO_3$ solubility,[9] the high temperatures of the kraft process (~165 °C) produce ideal circumstances for $CaCO_3$ precipitation with substantial growth where the temperatures are the highest, namely the heat transfer surfaces. This tendency for $CaCO_3$ scale to deposit on heat transfer surfaces manifests itself financially in the increased energy consumption required to heat solutions through the insulating layer of scale. Since the white liquor used for digestion of the wood chips is already supersaturated with $CaCO_3$, the added calcium from the wood material only exacerbates the precipitation issue by increasing the supersaturation levels within the cooking liquor. It should be noted that, although the chemical recovery cycle is a closed loop, calcium cannot be considered a non-processed element in the system. As shown in Figure 1.1, the re-causticizing process uses the addition of $Ca(OH)_2$ (in the form of CaO

from the lime kiln) to react with the $NaCO_3$ in the green liquor and replenish the NaOH levels in the liquor. The obvious side product of this reaction is precipitated $CaCO_3$ which is then separated from the liquor. Thus, any extra calcium from previous digestions is removed before the liquor is mixed with the new wood chips. Due to the reaction equilibrium, the subsequently saturated (in $CaCO_3$) white liquor is orders of magnitude higher in CO_3^{2-} anions than it is in Ca^{2+} cations. This saturation (or even supersaturation due to the temperature increase) implies that any calcium extracted from the wood chips immediately brings the solution out of equilibrium and increases supersaturation. To compound this effect, in the evaporators, the black liquor is concentrated to at least 75% solids content, increasing the supersaturation even more. Thus the two positions at highest risk for $CaCO_3$ scale deposits are both the heat transfer surfaces in the digester and evaporators.

Current practices employed to combat the growing deposits are two-fold. The first step involves adding a small amount of any chemical (an antiscalant) that will inhibit the deposition of scale during long periods of digester run-time. The antiscalant treatments are used to keep the scale growth down to manageable amounts until a scheduled shut-down period. The second step is then employed during these regularly scheduled down times and usually allows for a thorough removal of scale deposits. Typically, either hydroblasing is used to mechanically remove the scale from surfaces or acid washing is used to chemically remove the $CaCO_3$ (via dissolution and conversion to CO_2 gas). This manuscript's focus is on the former step and seeks to enhance the efficiency of antiscalants in order to allow for cheaper operational costs between shut-down cleanings.

While scale formation and the battles which ensue forth from it are not necessarily new (even the Romans fought scale in their aqueducts[10]), antiscalants are a relatively new advancement. Payen may have been the first to use an additive (starch) for the sole purpose of reducing scale deposition[11] and less than a century ago, Hall first used sodium hexametaphosphate as a scale inhibitor in boilers.[10] Even with over 70 years of research in the area, additives and impurities are known to retard scale growth, but still little is known with regards to the mechanism responsible for inhibition.[10] For the majority of

scale situations, empirically derived antiscalant formulations suffice despite actual mechanisms being fully understood. In the conditions particularly favorable for $CaCO_3$ such as the kraft pulping process, the accumulation of high temperature and extremely caustic pH levels has prevented the emergence of a suitable antiscalant (capable of completely shutting down scale formation) which is inexpensive and efficient enough to be used profitably with the large amounts of liquor solution processed per kilogram of pulp produced.

Before continuing on, some notes on the classification of antiscalant chemicals are in order. The same difficulties arise when trying to classify antiscalants as do when trying to classify the majority of things –there is more than one way to do it. For antiscalants, an understanding of the different methods of classification and nomenclature allows for a quick overview of some of the dynamic, and often times overlapping, aspects of scale inhibition.

Industry nomenclature

The antiscalant industry uses a number of terms to describe scale inhibitors *roughly* based on the chemical's inhibition mechanism. A schematic outline of the scale deposition process along with the general names given to antiscalants which are thought to stop the process of scale formation at that stage is given in Figure 1.2. For most chemicals, the mechanism changes depending on the conditions it is used in.[10] An example would be hexametaphosphate which may act as a sequestrant or a dispersant.[12] Noting that antiscalants are used for a number of different types of scale and in an even larger number of specific environments, chemicals are typically classified once (for a specific condition) and then they may be used for a different application (via another mechanism). This observation of one antiscalant inhibiting crystal growth via different mechanisms is also supported on a fundamental level by McKenna and his colleagues.[13] All of this adds to the confusion of nomenclature when it comes to pinning down a classification (by mechanism) for a specific scale inhibitor. As a result, in most cases these classifications are used interchangeably and are not meant to refer to a specific mechanism.

The category with the most defined boundaries is undoubtedly "sequestrants" which are also referred to as "chelating agents." These chemicals chelate with (or "sequester") the metal cations in solution, effectively eliminating the sequestered ions from participation in the precipitation process. Antiscalants falling under this category rarely show signs of different mechanisms. The typical example, introduced and utilized in any analytical chemistry lab, would be EDTA (ethylenediaminetetraacetic acid) as shown in Figure 1.3.

The stage of precipitation posing the most difficulties in direct observation would be the nuclei stage due to its nano-scale solid phases. In addition, these small solid phases are often dynamic and otherwise short lived, quickly transitioning towards the more energetically favorable larger crystals. As can be imagined, the mechanisms by which the antiscalants (as proposed by "threshold inhibitors" in Figure 1.2) stop (or slow) scale formation in this stage are little known.

Antiscalants used to stabilize solid crystal precipitates within the solution and therefore prevent aggregation and deposit on surfaces can be referred to as dispersants. A typical anionic polymer often times qualifies as a dispersant with its negatively charged functional groups repelling each other and the crystals it is adsorbed to. Clearly, a change in the pH of the solution with respect to the pK_a value of a polyanion will change the effectiveness of the antiscalant as a dispersant. This is one of the reasons for the numerous types of antiscalants on the market today; the mechanism (and therefore performance) of a given antiscalant is highly dependent on the nature of both the conditions of use and the chemical structure of the antiscalant itself. Of course, for polymeric antiscalants, the molecular weight is an important factor within the umbrella of chemical structure factors.

Stoichiometric-based classification

For a more scientific classification system with a concrete difference between inhibition via solution interactions and surface interactions along with a quantitative description of surface effects for antiscalants is needed. The concept between stoichiometric and sub-stoichiometric antiscalants is often a useful one but is rarely seen

outside the research literature. Of importance for industry is the fact that all other things being equal, a sub-stoichiometric additive is preferential because less of it is required to inhibit the problematic scale. Unfortunately, the assumption of all other things being equal is not a justified assumption. A method for distinguishing stoichiometric from sub-stoichiometric inhibition was introduced by Guo and Severtson following classical nucleation theory.[14]

In chemistry, stoichiometry is the quantitative relationship between products and reactants and/or their constituents. In the case of scale inhibition, the end result is the scale precipitate (i.e. $CaCO_3$) produced from ions (i.e., Ca^{2+} and CO_3^{2-}) and inhibitor (i.e., EDTA). As one can imagine, the quantitative relationship is not for the inhibitor and the amount of scale produced, but rather for relating the amount of inhibitor used and the amount of scale which is *not* precipitated (with respect to the same reaction in absence of the inhibitor). In other words, stoichiometry is the quantitative relationship between the amount of inhibitor and the ions it holds in solution. This holds particularly well when discussing chelating agents like EDTA. It should be noted that as with EDTA, using "stoichiometric" for other antiscalants usually implies a 1-to-1 ratio. That is, one mole of EDTA is required to inhibit one mole of Ca^{2+} ions from precipitating as $CaCO_3$.

The single most advantageous property of stoichiometric antiscalants derives from their reaction within the solution. Most stoichiometric antiscalants, when used at appropriate levels, produce a system which is thermodynamically stable and void of precipitate. This means that the system is equilibrated and will not produce scale even if given an exorbitant amount of time.

The most efficient scale inhibitors, on the other hand, work on a sub-stoichiometric level, implying that a mole of scale can be prevented by less than a mole of inhibitor. In reality, sub-stoichiometric antiscalants do not show a definitive ratio between the amount of chemical added to a system and the amount of scale reduction observed. This is mostly due to surface interactions rather than solution reactions. It is typical for crystals formed in sub-stoichiometric antiscalant systems to exhibit unordinary morphologies

and/or unclean surfaces. It is also typical of sub-stoichiometric antiscalants to exhibit a performance plateau as concentration is increased.

In comparison to stoichiometric antiscalants, sub-stoichiometric inhibitors have the advantage of being more efficient (lower concentrations are needed), but they have their own disadvantages as well. Working via surface interactions, they merely slow down the kinetics of scale formation. Whether, by reducing the nucleation rate or actively slowing the growth rates of crystal surfaces, the formation of scale is not stopped entirely. In most cases this is not a serious drawback since the goal is merely to prevent precipitation in localized troublesome areas within a chemical process line.

Small molecule antiscalant adsorption

Although this thesis focuses on the antiscalant mechanisms of polymeric antiscalants (with polyacrylic acid (PAA) being the major component) the mechanisms involved in smaller molecule inhibition of scale are an important starting point. The first compound quoted in the literature as an antiscalant was sodium hexametaphosphate, as shown in Figure 1.3. As mentioned by Cowan and Weintritt, sodium hexametaphosphate was still a common phosphate antiscalant in the 1970's despite its actual mechanism of inhibition being uncertain.[10] Some work has been done since then to understand the actual mechanism, but it is still not completely understood. Stephen Mann has helped elucidate how molecular functional groups interact with crystal surfaces. Although his publications are usually centered on crystal growth and morphology,[15-19] his attention to detail yields priceless information on the mechanisms involved in crystal inhibition and are useful in bridging the gap between the mechanisms involved with small molecule antiscalants and their larger polymeric counterparts. For molecules containing various acid functional groups such as carbonic, phosphonic, and even sulfonic groups, there are two basic trends in which the mechanism falls.

The first trend is the non-specific inhibition of crystal growth as characterized by the retarding of the growth rates of many or even all of the structurally different faces upon a crystal. In contrast, the second trend, stereochemical inhibition, reflects a much more specialized role which the antiscalants play with particular scale compounds.

Stereochemical effects are generally noticeable when specific crystal surfaces are inhibited when compared to the other faces. If the spacing between multiple functional acid groups is appropriately matched up with the repeating atoms or anions in a given crystal plane, there is the possibility for the molecules to bind to (or take the place of) these repeating units and therefore inhibit or seriously impede the growth process. As one can imagine this implies that a given molecule cannot act as a stereochemical inhibitor towards all scale compounds and can even have different efficacy levels when applied to different polymorphs of the same compound.[20, 21]

Adsorbance of dicarboxylate molecules onto calcite have been investigated along with their effects on crystal morphology.[15] It is evident that in the case of carboxylate functional groups and $CaCO_3$ crystal faces, the molecules adsorb in such a manner as to allow carboxylic acid groups access to the carbonate spots within the crystal lattice. Other molecules have also been experimented with almost always inhibiting the expression of calcite faces where the carbonate ions are lying perpendicular to the plane.[16-19]

It is interesting to match up the fundamental findings of Mann and his colleagues with the empirical trends of polymeric antiscalants. For decades, PAA and its copolymer relatives have been used as the primary ingredient in antiscalants. In particular, homopolymers and copolymers composed of many carboxylic acid functional groups have been used to inhibit calcium carbonate scale especially in kraft pulping mills. In general, copolymers synthesized by radical polymerization inhabit the antiscalant marketplace. Typically, the main monomer residues are of either acrylic acid or maleic acid origins which are both sources of the carboxylic acid functional groups (shown in Figure 1.3). Empirically, it has become practice over the years to also incorporate small percentages (by mole) of other monomers to the resulting polymeric antiscalant products. Though the presence of extra mers in antiscalant products is clear, their effect on inhibition (beyond simply improving efficiency over analogous homopolymers) is not understood. In addition, the importance of the chemical structure of the filler monomer residues is unclear. Using Mann's results on matching dicarboxylic acid groups with

calcite faces, glutaric acid (with the same chemical structure between –COOH groups as PAA homopolymer) shows a significant increase in $CaCO_3$ inhibition over chemicals with larger distances between carboxylic acid functional groups.[15] This suggests that a typical PAA homopolymer does not gain additional inhibition qualities by the increased distance between –COOH groups offered by inserting other mers between the acrylic acid mers. Although, at the same time, replacing an acrylic acid mer with another mer consisting of two backbone carbons does not decrease the lattice matching ability of the copolymer either, it only decreases the frequency of matching sites. The mechanistic advantages of the filler mers most likely have to do with factors other than lattice matching.

This thesis is focused on the effects of the molecular weight of the antiscalants rather than the chemical components. In order to separate the two dependencies, PAA homopolymers are used for the majority of testing conditions (after Ch. 2). This was decided upon due to the fact that acrylic acid is used as the base (and majority) monomer in almost all commercial polymeric antiscalants. It is assumed that as molecular weight dependencies are investigated and better understood, results and mechanistic qualities will be easily transferred to copolymers, although this portion is outside the scope of this thesis.

The role and tendencies of the molecular weight (MW) of PAA antiscalants is somewhat unclear seeing as studies typically use free-radical polymerized PAAs. PAA prepared by free-radical polymerization has a broad molecular weight distribution. In addition, specific MW effects on inhibition mechanisms such as morphology modification and adsorption tend to be reported and discussed at most as secondary interests[13] with MW distribution effects being completely ignored. As far as general antiscalant behavior goes, results have been reported suggesting a general optimal MW range being less than 20,000 g/mol but dependant upon antiscalant structure, inhibited salt, and reaction conditions.[22-24]

On a final topic, it is important to note some relationships between the major subject of the MW dependency of PAA on $CaCO_3$ in kraft conditions and those of other subjects,

particularly biomineralization. As both antiscalant and biomineralization research, at a fundamental mechanistic level, refer to the practical interactions of polyelectrolytes and sparingly soluble salts, it is important to note that calcium salts (and $CaCO_3$ in particular) find themselves playing important roles in both subjects. Cowan and Weintritt[10] sum up the dichotomy of $CaCO_3$ when they wrote:

> When the system calcium oxide-carbon dioxide-water manifests itself in the chalk cliffs of Dover or the architecture of Carlsbad Caverns, it arouses emotions in the observer which may be more lofty but are no more intense than those produced in an engineer by unseen workings of this same system when it converts a 12-inch into an 8-inch pipeline or reduces the heat transfer of a heat exchanger to 40 percent of its design value.

Where antiscalant research and implementation is usually concerned with preventing $CaCO_3$ precipitation and deposition, biomineralization research investigates how living organisms can so delicately (and precisely) control the precipitation of $CaCO_3$ with biomimetics intending to use that knowledge to design new materials. It is not at all difficult to believe that the three fields will have synergistic ties between their investigative research efforts. The previous observations by investigators researching scale inhibition are often built upon by those researching biomineralization. The converse would also be beneficial. Where antiscalant research is mainly focused on the final inhibition of $CaCO_3$, it is wise to use the invaluable information gathered during biomineralization experiments as they will often times focus on the extremely complex (and influential) interplay between the transformations between the various $CaCO_3$ polymorphs. From a chemical and structural standpoint, the three possible crystalline phases: calcite, aragonite, and vaterite, (in decreasing stability at 25 °C) are all characterized fairly well as outlined by Plummer and Busenberg.[25] With the addition of additives, whether they be inorganic, organic, or polymeric, the thermodynamic stability, kinetics, and transformation mechanisms between the three phases become more complex than inherently expected from such systems. In addition, amorphous calcium carbonate (ACC) has also been shown to be stable at ambient conditions (with the help of different types of stabilizers)[26] and intimately related to the biomineralization of calcite and aragonite (if not a precursor in the strictest sense of the word) with little being known

about the actual mechanism involved in the transformation.[27, 28] This ACC phase could be important to the design of new antiscalant technologies as even organisms use this (stabilized) phase as a carrier form in order to transport calcium to areas of $CaCO_3$ and hydroxyapatite growth/formation.[29, 30] Ideally, an antiscalant operating in an environment where the supersaturation level of $CaCO_3$ is too high for complete inhibition of nucleation/precipitation to occur would be able to stabilize ACC in a similar fashion as organisms and allow for the calcium to be swept away with the process stream without a chance to aggregate into deposits. The extremely favorable conditions for $CaCO_3$ precipitation within the kraft digestion and subsequent condensing processes of the liquor yields an excellent opportunity for the design of such an ideal antiscalant. Of course, the elegant methods in which living organisms have been designed to stabilize and transport calcium are both unnecessary and impractical in such a caustic environment as the kraft process, but the principles remain.

The goal of this manuscript is to outline some of the investigations used on current polymeric antiscalants in kraft pulping environments along with results from additional experimental techniques and specifically designed polymeric samples to investigate the influence which molecular weight has upon the antiscalant performance with additional emphasis put on the mechanisms responsible for the performance behavior.

Figures

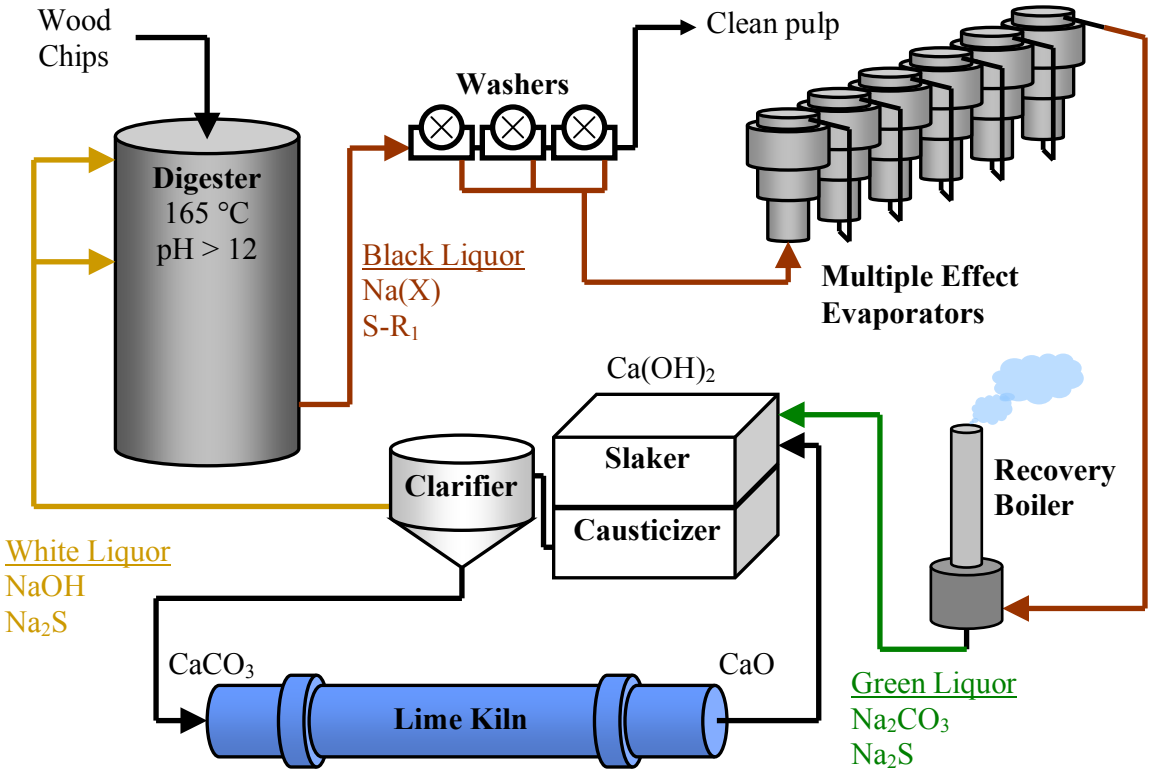

Figure 1.1 A schematic outline of the chemical recovery process involved in the kraft pulping process is shown. Wood chips enter the digester where they are added to the white liquor. After digesting, the black liquor is washed off of the pulp, condensed to >75% solids in the evaporators, and burned. The solids remaining from the recovery boiler are dissolved and re-causticized to produce white liquor to be used in further digestions. The re-causticizing process is part of an adjacent process loop with CaO being hydrolyzed into $Ca(OH)_2$ and reacted with the Na_2CO_3 of the green liquor to form $CaCO_3$ deposits which are precipitated in the clarifier. The $CaCO_3$ solids are then calcined in the lime kiln to recover the CaO required for subsequent loops.

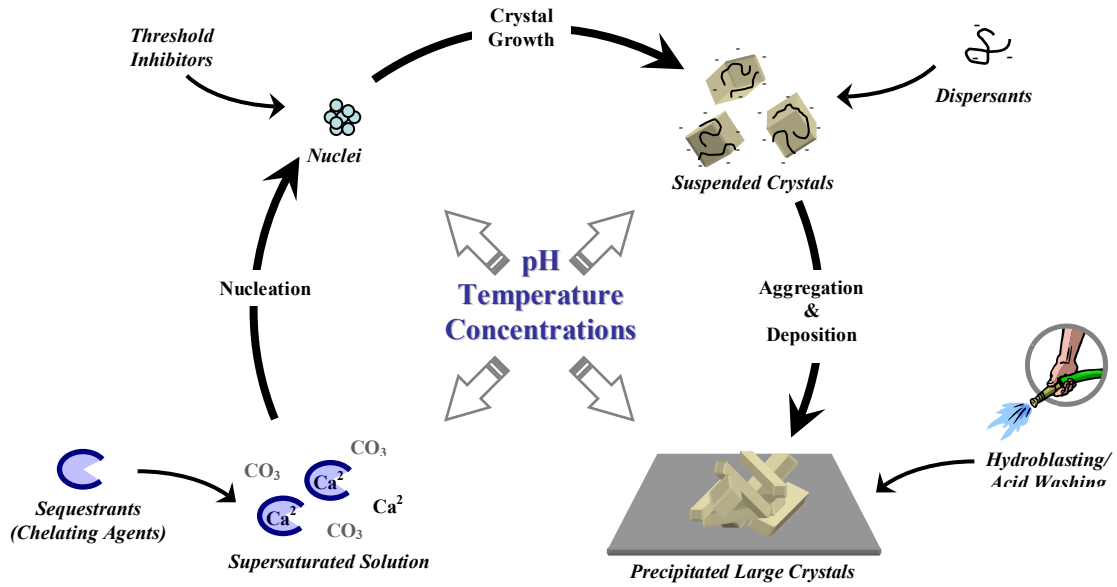

Figure 1.2 A schematic outline depicting the various phases of scale formation beginning with a supersaturated solution and moving through nucleation and crystal growth to end with deposited scale surfaces. Also shown are the schematic representations of how antiscalants can prevent the system from progressing forward towards deposition noting that the methods involved in scale inhibition are determined by a number of things such as pH, temperature, and concentrations (of antiscalant and the slightly soluble components).

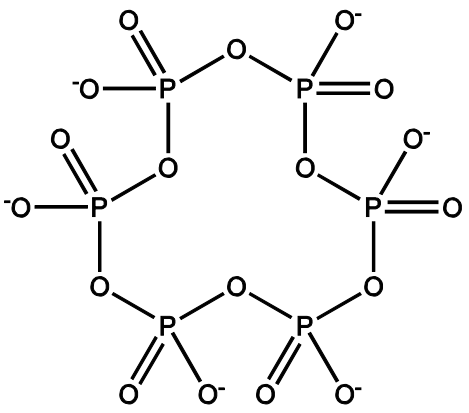

Sodium hexametaphosphate

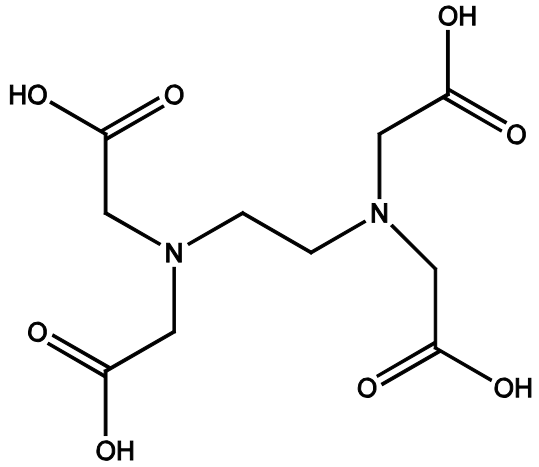

Ethylenediaminetetraacetic acid
(EDTA)

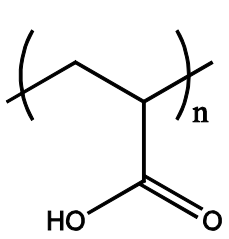

poly(acrylic acid)
(PAA)

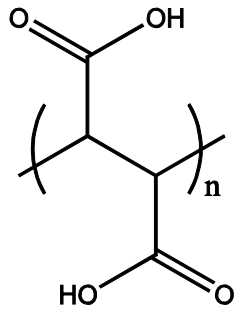

poly(maleic acid)
(PMA)

Figure 1.3 Chemical structures of two common small molecule antiscalants, sodium hexametaphosphate (upper-left), ethylenediaminetetraacetic acid (EDTA, upper-right), and two polymeric antiscalants, poly(acrylic acid) (PAA, lower-left), and poly(maleic acid) (PMA, lower-right).

Chapter 2 – Testing of Currently Available Antiscalants

Introduction

As with any precipitation process, whether it is desired or not, the precipitate formed during the kraft pulping process is a result of the supersaturation of the component species resulting in scale formation and buildup. In this case, the scale is predominantly calcium carbonate[31] forming mainly on the heat exchange surfaces of the digester and the black liquor evaporators resulting in reduced heat flow, increased energy consumption, and increased monetary losses due to unscheduled shutdowns. $CaCO_3$ also deposits on conduits, valves, screens, and pumps thereby decreasing the efficiency (and sometimes the safety) of the entire system. Factors that influence the point where nucleation occurs, the place where the deposit forms, and the amount of scale deposited include supersaturation levels, temperature, fluid shear, and the stability of the developing crystalline phase.[10, 32] Another important aspect, particularly with respect to where deposits form, concerns the effects which other chemicals present in the process liquors have upon the nucleation and growth kinetics of the forming $CaCO_3$.[33, 34] These chemicals are mostly introduced into the liquor with the specific objective of inhibiting the scale deposition rate, but can also originate from the delignification reactions occurring within the kraft digestion.[24, 35]

The importance of additives designed to limit the malign effects of scale deposition in the kraft process is exacerbated by the conditions present at the mill. Due to the recausticizing process, the white liquor enters the digestion reactor already saturated in $CaCO_3$.[2] The level of supersaturation quickly rises as the liquor is heated to ~165 °C and calcium ions are introduced via the wood chips. The solubility curves for calcite[25] up to digester temperatures are shown in Figure 2.1. Since most incoming white liquors are already saturated in $CaCO_3$ with around 70 g of Na_2CO_3 per liter of liquor (~0.7 M CO_3^{2-}), any increase in temperature immediately supersaturates the solution.[2] Alongside this, the calcium ions extracted from the wood (1-2 ppt Ca/dry wood)[36, 37] have a more severe effect on the supersaturation than the rise in temperature. Compounding these

factors, the spent (black) liquor is then concentrated (to at least 75% solids) in the evaporators, increasing the supersaturation all the more.[2] Fortunately, observable $CaCO_3$ precipitation is not usually recognized until the system is well beyond its solubility limit. This region between the solubility limit where all calcium and carbonate ions are thermodynamically stable in solution, and the point where precipitation (nucleation and growth) occurs rather quickly is termed metastable. This metastable region is often used to explain the dynamics of the supersaturation levels in digester scaling studies.[31] The result of any effective antiscalant is clearly to extend this metastable region and inhibit the kinetics of $CaCO_3$ deposition.

Classical nucleation theory can be used to model the distinction between the metastable region and the stable region beyond which calcium carbonate exists as a stable separate phase.[14, 38, 39] Accordingly, the steady-state nucleation rate, J, can be expressed as,[40, 41]

$$J = J_{\max} \exp\left[-\frac{4\beta_a^{\,3} v_m^{\,2} \gamma^3}{27\beta_v^{\,2} (k_B T)^3 (\ln S)^2} \right] = J_{\max} \exp\left[-\frac{\beta}{T^3 (\ln S)^2} \right] \qquad (1)$$

where J is the number of nuclei formed per unit volume per unit time, J_{max} is the frequency factor, T denotes temperature (in degrees Kelvin), and β is a conglomerate of variables used to combine constants for simplification, namely $\beta = \frac{4\beta_a^{\,3} v_m^{\,2} \gamma^3}{27\beta_v^{\,2} k_B}$. Here, β_a and β_v are respectively the area and volume conversion factors (which for a sphere are 4π and $4\pi/3$, respectively), while v_m is the molecular volume of the precipitated nuclei, γ is the surface free energy per unit area, and k_B is the usual Boltzmann constant. The variable S is the supersaturation (or supersaturation ratio) which can be defined in terms of the component activities, $a_{Ca^{2+}}$ and $a_{CO_3^{2+}}$, and the solubility product of $CaCO_3$, K_{sp} as follows.

$$S = \frac{a_{Ca^{2+}} a_{CO_3^{2-}}}{K_{sp}} = \frac{\gamma_{Ca^{2+}} C_{Ca^{2+}} \gamma_{CO_3^{2-}} C_{CO_3^{2-}}}{K_{sp}} = \frac{\gamma_{Ca^{2+}} [Ca^{2+}] \gamma_{CO_3^{2-}} [CO_3^{2-}]}{K_{sp}} \quad (2)$$

Here, the liberty has been taken to separate the activities of the numerator into their constituent products of activity coefficients, $\gamma_{Ca^{2+}}$ and $\gamma_{CO_3^{2-}}$, and concentrations, either $C_{Ca^{2+}}$ and $C_{CO_3^{2-}}$ or [Ca^{2+}] and [CO_3^{2-}]. For the case of $CaCO_3$, nucleation often remains close to zero until critical values of either temperature or calcium levels are reached whereby nucleation rises asymptotically before reaching its maximum value. After nucleation, the nuclei continue to grow in the supersaturated solution. A second order rate law has been reported to describe the growth kinetics for sparingly soluble calcium salts in seeded solutions.[42, 43] For the case of $CaCO_3$, the change in dissolved calcium concentration with respect to time takes the form,

$$-\frac{dc}{dt} = kA(c - c_\infty)^2 \quad (3)$$

where k and A represent the usual rate constant and effective surface area of the crystals, respectively, while c and c_∞ are the concentrations of dissolved calcium at time t and at equilibrium respectively. By no means do equations 1-3 cover the entirety of the mechanism involved in deposition of scale, but they do provide an understanding of the processes most likely responsible for most deposits. In this section, the effectiveness and efficiency of a number of commercial polymeric antiscalants will be analyzed using these principles to help determine how the molecular weight affects performance. Two methods were utilized; 1) a laboratory kraft digester was implemented similar to the method Hartler and Libert[31] used, which emulates mill situations on a small batch scale and 2) a simplified reaction scheme performed in a Parr bomb autoclave system representative of the multiple effect condensers used at mills to concentrate the strong black liquor.

Materials and Methods

Chemicals and Materials

Inorganic materials including anhydrous Na_2CO (CAS# 497-19-8), NaOH (50% $^{w}/_{w}$ CAS# 1310-73-2), anhydrous $CaCl_2$ (CAS# 10043-52-4), anhydrous NaOH (CAS# 1310-73-2), $Na_2S{\cdot}9H_2O$ (CAS# 1313-84-4), H_2SO_4 (CAS# 7664-93-9), and HCl (CAS# 7647-01-0) were purchased from Sigma-Aldrich (St. Louis, MO) as reagent grade chemicals. Poly(acrylic acid) and its neutralized salt form, sodium polyacrylate, were purchased from Polysciences Incorporated (Warrington, PA) as solutions with concentrations ranging from 20 to 63% $^{w}/_{w}$. Commercial polymeric antiscalants originated from Kemira Chemicals, Incorporated (Atlanta, GA), Ashland Incorporated (Covington, KY), and Houghton Chemical Corporation (Allston, MA). Wood chips were provided by the SAPPI paper mill located in Cloquet, MN in bulk and kept refrigerated until use.

Laboratory Kraft Digester

Wood chips

Wood chips, as attained from the SAPPI mill, were sorted and only 1"×1" or smaller chips free of visible knots and imperfections were used. Chips were oven dried at 65 °C and then 800 g were massed out for each individual experiment yielding a 5:1 liquor-to-wood ratio.

White liquor

Fresh white liquor was prepared using 164 g $Na_2S{\cdot}9H_2O$, 164 g NaOH, nominally 20 g Na_2CO_3, and from 0 to 200 mg/L (solids content) inhibitor sample. 4 L of liquid was produced and used for each individual experiment with calculated effective alkalinity, sulfidity, and causticity at 48 g/L, 25%, and nominally 92% respectively.

Kraft Pulping Process

Batch kraft pulping reactions were carried out in a 6 L digester from MK Systems (Danvers, MA) modified with an extractor port connected to a condenser in order to remove samples of the circulating liquor while the system was under high temperatures and pressures. Prior to each experiment, the system was flushed with 10% (v/v) sulfuric

acid solution for at least 10 minutes in order to remove any existing $CaCO_3$ deposits followed by rinses with copious amounts of deionized water. The extractor port and condenser contained no more than 10 mL of volume which was purged before each sample was collected.

For each experiment the 800 g of wood chips was added to the clean digester vessel. The 4 L of white liquor was then added to the wood chips and the vessel was sealed off and heating was initiated. The digestion temperature was ramped up and then held at 180 °C for 3 hours. Samples were taken in ~15 mL aliquots initially and every 15 minutes for the first two hours and then every half-hour for the third hour. 1 mL of unfiltered black liquor samples were quantitatively added to 5 mL of ~5% (w/w) HCl solution. Additionally, 1 mL of filtered (through a 0.45 μm PTFE syringe filter) black liquor samples were also quantitatively added to 5 mL of ~5% (w/w) HCl solution. The set of samples were then centrifuged to separate the lignin and other solids from the solution phase. Calcium concentrations of the solution phase were determined using a PerkinElmer (Shelton, CT) 100 AAnalyst Absorption spectrometer.

Parr Bomb Reactions

Reaction mixture

For each experiment, 2 L of a metastable solution consisting of 50 mg/L Ca^{2+} (1.25 mM), 1 g/L Na_2CO_3 (9.43 mM CO_3^{2-}), and 5 g/L NaOH (pH > 13) along with anywhere from 0 to 50 mg/L polymer antiscalant was prepared by combining two stable solutions just prior to the autoclaved run. Anhydrous sodium carbonate, NaOH, and any antiscalant sample were first dissolved in ~1.8 L of 18 MΩ water before 100 mL of a 1000 mg/L Ca^{2+} (introduced as anhydrous $CaCl_2$) solution was quantitatively added and the solution was diluted to 2 L. Ten minutes were allowed to pass between the addition of the Ca^{2+} solution and the beginning of the experiment to ensure consistency between individual runs.

Parr reaction

The autoclave vessel used was a model 4522, stirred, 2-L Parr (Moline, IL) reactor with a sample extraction port leading to a water-cooled condenser. The reaction solution was sealed into the autoclave vessel with an initial temperature of ~25 °C. The vessel was heated to 150 °C in 25 °C intervals with 10 minute plateaus between heating ramps. The rate of heating was ~2 °C/min. Samples of the reaction mixture were taken before and after every plateau temperature. For each sample, 1 mL of the unfiltered reaction mixture sample was added to 5 mL of ~5% HCl solution to give the total calcium concentration while another 1 mL of the filtered (through a 0.45 μm PTFE syringe filter) sample was added to a separate 5 mL of ~5% HCl solution to yield the dissolved calcium concentration. Sample sets were then analyzed via atomic absorbance (AA) to determine the concentration of calcium associated with solution and solid phases. Concentrations for "Dissolved" (filtered samples), "Total" (un-filtered samples), and "Suspended" (total – dissolved) or dispersed calcium were then plotted against time (along with the reactor temperature).

Temperature degradation

Solutions

Two solution types were used during degradation experiments: pH 7 and a "mock kraft" solution. The pH 7 solution mixture was prepared as 2 L of a 1000 ppm polymer sample (active acids), and adjusted to pH 7.0 with NaOH and HCl. The mock kraft solutions were also prepared as 1000 mg/L polymer samples (active acids), but also with 40 g of $Na_2S \cdot 9H_2O$, 40 g NaOH, and 5 g Na_2CO_3 in 2 liters yielding a slightly dilute white liquor composition of 23 g/L effective alkali and 25% sulfidity.

Degradation

For the degradation of Na-PAA and PAA samples, solutions were prepared as above and degraded using a model 4522, stirred, 2-L Parr (Moline, IL) reactor with a sample extraction port leading to a water-cooled condenser. Approximately 1.6 L of the reaction solution was sealed into the autoclave vessel with an initial temperature of ~25 °C. The

vessel was heated to 160 °C as quickly as possible, typically reaching its target temperature in less than an hour. Approximately 130 mL samples were removed from the vessel at 60 minute increments and allowed to further cool to room temperature to be used for size exclusion chromatography (SEC) analysis and $CaCO_3$ inhibition experiments. Smaller, 20 mL, samples were also taken half way in between the 1 hour samples for the sole purpose of SEC samples. SEC samples were produced by filtering 1 mL of sample through a 0.45 μm PTFE syringe filter and mixing with another 1 mL of doubly concentrated SEC eluent. The remainder of each sample was stored until used for inhibition studies.

$CaCO_3$ Inhibition

A similar method to the Parr bomb reactions described above was used to examine the inhibition of the degraded polymer samples, the only difference being the source of the polymer itself. Solutions were all 50 mg/L of polymer (active acids), but for the samples degraded in mock kraft conditions, the portion of NaOH and sulfide present in the 100 mL of sample used was diluted into the 2 L of solution prepared for the inhibition experiments. Thus, the final solution composition resembled dilute white liquor characterized as 6.2 g/L effective alkali, 88% causticity, and 5% sulfidity or in more fundamental units: 1.25 mM Ca^{2+}, 10.6 mM CO_3^{2-}, and 12 g/L NaOH (pH > 14). From this point on, the rest of the method was identical to the Parr bomb reactions above.

Size Exclusion Chromatography (SEC)

The equipment used was made up of a Waters In-Line Degasser AF, Waters 1525 Binary HPLC Pump, Waters 717plus Autosampler, Waters Column Heater Module, Waters 2487 Dual λ Absorbance Detector, and Waters 2414 Refractive Index Detector all controlled via the Breeze version 3.30 SPA software package. A guard column and two GPC columns (Waters 250 & 120 Hydrogel columns) were connected in series and heated to 30°C for consistency. The estimated volume between the sample injector port and the RI detector was 10.75 mL (as determined by the onset of RI change for a 323,000 MW Na-PAA sample. The UV absorbance detector was monitoring λ values of 243 nm and/or 210 nm.

Samples were mixed with an equal volume of doubly concentrated eluent solution to minimize the difference between injected samples and eluent compositions. SEC eluent was adjusted to pH 7.0 with NaOH or HCl and was either 0.2 M $NaNO_3$ and 0.01 M NaH_2PO_4 or 0.3 M NaCl and 0.1 M NaH_2PO_4 (for UV transparency). Eluent was prepared in 4 L batches and then used for both standards and samples to avoid discrepancies produced from minor differences in salt concentrations and pH between batches. Flow rates were varied in order to keep back pressures below 1200 psi but kept constant for an entire use of an eluent batch.

Results & Discussion

Laboratory Kraft Digester

The results of a typical kraft digester experiment without any added inhibitor is shown in Figure 2.2 where the recorded temperature of the cooking liquor is plotted as the dashed line according to the secondary axis while the total, dissolved, and suspended amounts of calcium in the liquor are shown. It can be seen that as the temperature rises, the amount of calcium leached out of the wood chips increases until it reaches a maximum value at around 45 minutes (~160 °C) where the calcium levels begin to drop down to a constant value around 6 mg/L. In agreement with Hartler and Libert,[31] the results express the idea of a metastable region where the system exists in a supersaturated state but precipitation of $CaCO_3$ is prolonged until a critical point, both in temperature and supersaturation, is reached where upon deposits nucleate and grow quickly. In an effort to investigate this upper limit of the metastable region, classical nucleation theory is applied as follows.

Substituting Equation 2 into Equation 1 and solving for the temperature yields,

$$T^{-3/2} = \left[\frac{\ln\left(J_{max}/J\right)}{\beta}\right]^{1/2} \ln\left(\frac{\gamma_{Ca^{2+}}\gamma_{CO_3^{2-}}}{K_{sp}}\right) + \left[\frac{\ln\left(J_{max}/J\right)}{\beta}\right]^{1/2} \ln\left(C_{Ca^{2+}}C_{CO_3^{2-}}\right) \qquad (4)$$

which allows for the linear fit of temperature values with respect to the product of both calcium and carbonate concentrations. Since both temperature and calcium levels are dependent variables in a kraft cook, the carbonate level was varied in order to produce enough data for a linear fit. Simultaneously, solving Equation 4 again for the calcium concentration with respect to the carbonate concentration at a given temperature yields,

$$C_{Ca^{2+}} = \exp\left(\left[\frac{\beta}{\ln\left(J_{max}/J\right)}\right]^{1/2} T^{-3/2} - \ln\left[\frac{\gamma_{Ca^{2+}}\gamma_{CO_3^{2-}}}{K_{sp}}\right] - \ln\left[C_{CO_3^{2-}}\right]\right) \quad (5)$$

with the temperature term's coefficient being simply the inverse of the slope from Equation 4 while the second logarithmic term is the dividend of the y-intercept and the slope from Equation 4. The edge of the metastable and stable $CaCO_3$ precipitate regions has been plotted for different temperatures in this kraft digester system in Figure 2.3 along with the solubility limits as calculated in the Introduction section (Figure 2.1). Although a seemingly large amount of information has been estimated from a few data points, considering the limitations of the system, it is still reasonable to draw at least one important conclusion from Figure 2.3. At any given temperature, the critical point at which rapid nucleation of $CaCO_3$ sets in during a kraft cook is orders of magnitude higher, with respect to calcium concentrations, than the solubility limit of calcite would suggest. As previously mentioned, the presence of compounds resulting from the delignification process most likely plays a part in this limited inhibition of $CaCO_3$ precipitation. Although the system is complex with respect to the sheer number of reactions and chemical compounds, at least one set of chemicals, namely the lignin fragments, have previously been noted to have such a limited effect on scale inhibition.[24] Pragmatically, this realization does not ease the pain of the paper mill engineers responsible for keeping the system clear of scale though, because what ever inhibition may be influencing the system through delignification alone does not fully prevent the problem. It is clear that the implementation of a small amount of antiscalant capable of

extending this metastable region is abundantly advantageous. Since so many products already exist for use as antiscalants in kraft digesters, a broad range of commercial antiscalants were tested, as listed in Table 1.1, in order to elucidate the more important factors in an effective scale control agent.

In order to normalize the test results of the commercial products, a clear picture of the amount and availability of the calcium within the wood chips was sought after. On a previous batch of wood chips, the calcium levels during kraft cooks were monitored while increasing amounts of a chelating agent, EDTA, were added to the initial white liquor until all calcium leached from the wood chips remained in solution. The dissolved calcium levels with respect to time and temperature are shown in Figure 2.4. The resulting maximum amount of calcium available to be leached out of the wood chips is shown to be approximately 135 mg per liter of liquor. The residual molar amount of calcium left dissolved in solution (after any nucleation) is plotted against the initial molar amount of EDTA used in preparing the white liquor in Figure 2.5. The essentially stoichiometric match (1.01:1) between the molar amounts of calcium and EDTA in the solution provide solid evidence that EDTA still functions as a stoichiometric chelating agent under these harsh conditions and that the total amount of dissolved calcium observed under the maximum loading of EDTA is an accurate representation of the typical amount of calcium actually leached from the wood chips during any given experiment. Another interesting piece of information gathered from Figure 2.4 is the confirmation that calcium ions are continuously pulled from the wood chips in a similar fashion to the other divalent metal cations such as manganese and magnesium, but the rate at which the Ca^{2+} is leached decreases to a much larger extent than Mn^{2+} and Mg^{2+} once the temperature is kept constant.[31] For the present experiments, the maximum concentration of calcium was 135.4 ppm in the final black liquor after 3 hours of digestion suggesting a total leachable amount of calcium in the wood chips to be at least 677 ppm. For the sake of consistency, all other batches of wood chips were checked using a similar method to ensure comparable results. All batches of wood chips were found to be within 7% of this value.

Commercial Polymer Samples

The more commonly used products were tested under kraft digestion conditions at dosages of 10, 50, 100, and 200 mg/L for their effects on $CaCO_3$ scale inhibition. Dosages for any products that were known to be sodium salts were adjusted to represent the effective acid portion. The dissolved calcium levels in the cooking liquor for kraft cooks dosed with various concentrations of the industry benchmark, labeled C-24, are shown in Figure 2.6. The "tail" portions of the curves (after maximum Ca^{2+} concentrations) were analyzed in order to detail some of the crystal growth kinetic ramifications of various doses. Differentiating the 2nd order rate law from Equation 3 yields,

$$-\int (c - c_\infty)^{-2}\, dc = \int kA\, dt \Rightarrow \frac{1}{c - c_\infty} = kAt + C_{\text{int}} \tag{6}$$

with C_{int} being the constant of integration. Using the data point immediately after the maximum Ca^{2+} concentration the "initial" point over which the differential equation was valid allows for the integration constant to be solved for,

$$C_{\text{int}} = \frac{1}{c - c_\infty} - kAt = \frac{1}{c_i - c_\infty} - kAt_i \tag{7}$$

with t_i and c_i indicating the time and Ca^{2+} concentration for the "initial" point, respectively. Substituting C_{int} from Equation 7 back into the solution from Equation 6 and solving for the dissolved calcium concentration as a function of time, t, yields,

$$c = c_\infty + \frac{1}{kA(t - t_i) + \dfrac{1}{c_i - c_\infty}} \tag{8}$$

which can be used to fit all data points after nucleation. There are a few nuances worth mentioning though, at least briefly. Firstly, with respect to the kA fitting constant; the 2nd order rate constant, k, is assumed to be constant throughout the crystal growth

process despite its obvious dependence on temperature. This is a safe assumption here since the temperature of the digester, and the cooking liquor has reached its maximum value of 180 °C and is kept constant by the time the "tail" region has been reached. The surface area, A, of the crystals however, is not expected to remain constant throughout the growth process, but presumed to have a minimal effect on the overall value of kA and allowed to remain modeled as such since an accurate measurement of this is implausible via small liquor samples where the majority of the calcium deposits are inaccessible within the wood chips.[35] Secondly, and perhaps more obvious, is that the equilibrium concentration, c_∞, is not ever represented in the data explicitly since calcium is continuing to be leached from the wood chips as discussed earlier. It is however, accurate to suggest that c_∞ would be reached if the system was denied its calcium source at some point and worth noting that Equation 8 does allow for the addition of calcium to the system since it simply represents the differential at each point. Lastly, during the fitting procedure, the "initial" point was used solely for the initial guesses for t_i and c_i and then regarded as another sample point thereafter. This kept the fitted line from being forced through the initial sample point. MATLAB software from The MathWorks, Inc. (Natick, MA) was used to perform all the non-linear regression fits using nominal starting guesses of 10^4 $L \cdot mg^{-1} \cdot min^{-1}$ and 3.0 $mg \cdot L^{-1}$ for kA and c_∞ respectively, while typically using the data from sample times within 60 and 90 minutes for t_i and c_i.

The accumulated kA and c_∞ results for the 10 mg/L dosages are shown in Figure 2.7 with respect to the weight average molecular weight of the product (as determined via SEC). The dashed line represents a parabolic fit of the kA values with respect to the logarithm of the MW of the polymer samples. It is not intended to represent a model explaining the decrease in kA around 5,000 – 20,000 M_w, but with an R^2 value at nearly ½, it does help emphasize the reality of the optimal MW range as shown considering the range of chemical structures represented by the sampling. The fitting parameter kA, made up partly by the rate of crystal growth, decreased significantly as the MW increased through the optimal range with the rate of growth once again increasing as MW increased past the region. In conjunction, the equilibrium value for the dissolved calcium left in solution, c_∞, decreased as the MW increased but remained consistently low as the MW

increased through and beyond the optimal range. With respect to these two trends, it is interesting to note their change with respect to sample concentration changes. The *kA* parameters did not show a significant change in their values as the concentration increased and actually began to lose their distinction for the optimal range. This in part can easily be explained as the polydispersity of the samples is taken into account. As the overall dosage of the sample was increased, the effectiveness of only the species falling within the optimal MW range is counterbalanced by outlying species with less inhibition effectiveness.[44] As for the c_∞ values, with increasing polymer concentration, the equilibrium concentration of dissolved Ca^{2+} remained close to 4 mg/L for the optimal MW range and higher with an increase in scattering surrounding the same value for the lower MW samples. This suggests that the polymer antiscalants show a limited (if any) ability to chelate the free calcium in the system and therefore act as inhibitors by primarily slowing the kinetics of $CaCO_3$ growth.

Parr Bomb Reactor

The complex chemical and physical conditions inherent with the kraft pulping process can easily complicate the testing of antiscalant efficiencies and mechanisms. A more controlled laboratory environment is often sought after. Replacing the wood chips with a controlled dosage of Ca^{2+} and mimicking a kraft digest in a Parr bomb (autoclave vessel) is an exceptionally versatile method of analysis. Na_2S can be eliminated to further the simplification of the system under investigation while a temperature ramp mimics the conditions seen in the multiple effect evaporators (condensers) of the kraft chemical recovery process. Here, the supersaturation levels of $CaCO_3$ are increased not by the addition of calcium to the strong black liquor, but by decreasing the solubility (and metastable) limit via the increase in temperature.

Shown in Figure 2.8 are the typical calcium concentrations for a Parr reaction without any inhibitor added. As can be seen by the drop in dissolved calcium levels, nucleation occurs quickly and growth continues un-inhibited until the $[Ca^{2+}]$ reaches its solubility limit for $CaCO_3$. The temperature at which nucleation is deemed to have occurred, T_{nucl}, is calculated by finding the corresponding temperature at the point at which the dissolved

calcium concentration drops 15% from the initial value. The total calcium in the reaction mixture also drops with time and temperature most likely due to the formation of crystals too large to remain suspended and deposit formation on the metal surfaces of the reaction container and stirrer.

Similarly to the kraft digester results, the dissolved calcium in solution can be modeled using the second-order rate law from Equation 3 and outlined in Equations 6-8. In addition, the change in temperature must be accounted for as it is the source of the increased supersaturation here. Rather than leaving the 2nd order rate constant, k, as a constant, its temperature dependence can be expressed by the Arrhenius equation:

$$\mathrm{k}(T) = A_1 \exp\left(\frac{-E_a}{RT}\right) \tag{9}$$

where k(T) represents the rate constant now as a function of temperature, while A_1 and E_a are the pre-exponential factor and activation energy respectively with R and T as the usual gas constant and temperature in Kelvin.[45] If the time dependence of the temperature during the Parr reactions is considered to be of the linear form $\mathrm{T}(t) = mt + b$ with m and b representing the slope and intercept respectively, the rate constant can then be recast as a function of time for these purposes.

$$\mathrm{k}(t) = A_1 \exp\left[\frac{-E_a}{R(mt+b)}\right] = A_1 \exp\left[\frac{-\left(E_a/Rm\right)}{\left(t+b/m\right)}\right] \tag{10}$$

Finally, substituting Equation 10 into Equation 8 for the rate constant yields

$$c = c_\infty + \frac{1}{A_1 \exp\left[\frac{-\left(E_a/Rm\right)}{\left(t+b/m\right)}\right] A(t-t_i) + \frac{1}{c_i - c_\infty}} \tag{11.a}$$

Or
$$c = c_\infty + \frac{1}{A_k \exp\left(\frac{-E_R}{t+t_0}\right)(t-t_i) + \frac{1}{c_i - c_\infty}} \qquad (11.b)$$

with A_k and E_R used as the fitting constants representing the product of the pre-exponential factor and the area of the growing crystals, A_1A, and a transformed activation energy time, E_a/Rm, respectively. In addition, Equation 11.b also takes the liberty of defining a new constant, $t_0 \equiv b/m$ used to simplify the equation but providing no physical meaning. As with the temperature independent rate law fitting used for the kraft digester fitting, MATLAB software was again used to perform all the non-linear regression fits of Equation 11.b using nominal starting guesses of 1.7×10^6 L·mg^{-1}·min^{-1}, 8×10^3 min, and 5 mg·L^{-1} for A_k, E_R, and c_∞ respectively. The starting point over which Equation 3 was originally said to apply to (the "tail"), was nominally guessed as the sample point at 10 minutes. Thus, the initial guess for c_i was set to the dissolved calcium concentration at 10 minutes (t_i), but set up as a value to be found during the non-linear fitting. This allowed for an optimal fitting of the equation to the data. Shown in Figure 2.9 are the dissolved calcium concentrations for various concentrations of a well established antiscalant product, C-20, with respect to time (and temperature). As expected, the time (and therefore temperature) at which the calcium precipitated out from the solution phase increased with increasing antiscalant dosage. Unfortunately, as less and less of the [Ca^{2+}] curve fit within the time/temperature frame of the experimental setup, the accuracy of the non-linear fit also became less and less. In some cases (like the 50 mg/L dose of C-20), the "best" fit used only the last couple of data points as the most important "tail" region. This is entirely correct, but created a vast amount of room for error. In this case, the fitting program "found" an impossible value of -1,700 mg/L as the value for c_∞ to fit the data the best. With c_∞ being drastically out of range, A_k and E_R were also compromised in order to maintain an optimal correlation between the fitted line and the data. Needless to say, as the effectiveness of the added inhibitor increased, whether through a high dosage or high efficiency, the validity of the individual fitting parameters decreased

regardless of any high correlation between the fit and the data. All data presented here was well-fit except for the 50 mg/L dose of C-20 shown in Figure 2.9 which is given an example of poorly-fit data. For well-fit data, two trends were shown: the activation energy (on the order of 100 kJ/mol) increased with concentration as did the calculated equilibrium dissolved calcium concentration, c_∞ (ranging from 3 to 10 mg/L). The increasing activation energy for producing the solid phase $CaCO_3$ suggests that the polymer antiscalants inhibit growth via a surface mechanism resulting in a slowing of the growth kinetics. This has been previously described as the sub-stoichiometric relationship between the polymer concentration and the amount of $CaCO_3$ inhibited.[14] On the other hand, if the c_∞ values predicted via the non-linear fitting are correct, the increase in final equilibrium Ca^{2+} levels would suggest a mechanism more in resemblance of chelation as the solubility of $CaCO_3$ is increased, but the increase itself was *not* always linear and often more representative of a logarithmic function, suggesting that a strict stoichiometric chelation effect was not responsible for the concentration effects on c_∞. More likely is the concept that the polyelectrolytes are capable of working both in the solution phase (increasing c_∞) and on the growing surfaces (increasing E_a). Since the increase in c_∞ was much less significant in terms of inhibiting scale, the surface effects responsible for the decrease in growth kinetics was assumed to be the more beneficial parameter for investigating the efficiency of antiscalants. This was also backed by the circumstances of scale formation in the present study, since precipitation and growth are instigated and exacerbated via the increase in temperature, the available thermal energy in respect to the activation energy required to sustain growth is of utmost importance.

In an effort to relate the temperature based kinetics of deposition formation and growth to the molecular weight of the polymer antiscalant, it was found that T_{nucl}, the calculated temperature at which the dissolved calcium dropped by 15%, and f_{120}, the fraction of residual calcium (at 2 hours, 150 °C) with respect to the initial concentration, were a more reliable indicator of performance since they did not rely so heavily on the availability of data points representing the later half (tail) of the $[Ca^{2+}]$ S-curve. Plotted in Figure 2.10 are the T_{nucl} values and residual calcium levels with respect to the polymer

MW at a concentration of 10 mg/L. In general, the T_{nucl} values tend to decrease as MW increases but with an increase in the variability of the data also associated with an increase in MW. This general trend extended through all concentrations tested and even for the homopolymers themselves to a lesser extent. Poly(acrylic acid) samples, denoted with a + sign within the square data points (□), did not show as steep a dependence as the whole sample set, but still expressed the same general trend of increased performance with lower MW. Additionally, it should be noted that some of the highest T_{nucl} values from the lowest MWs represented the three maleic acid homopolymer samples, shown in Figure 2.10 with a × sign within the square data points (□). The fraction of calcium left in solution after 120 minutes (150 °C) is also plotted in Figure 2.10 with respect to the secondary axis. In contrast to the T_{nucl} data, f_{120} expressed a local minimum around the molecular weight range of 10,000. This trend resembles the c_{∞} response to MW during the kraft digester experiments. Again, the overall low residual amount of calcium remaining in solution after nucleation seems to suggest that the polymers are either not acting as chelating agents or are being removed from solution along with the Ca^{2+} during the precipitation stage.

As a clearer picture of the mechanisms involved in $CaCO_3$ inhibition due to polyelectrolytes is developed, it is apparent here that a couple of factors influence the effectiveness of polymer antiscalants. Firstly, the presence of different functional groups along the polymer chain influences performance. This, for the most part, is apparent simply by the nature of the polyelectrolytes empirically chosen as antiscalants by the chemical companies. The patent literature almost always uses poly(acrylic acid) or poly(maleic acid) as the base for any copolymer antiscalant designed for kraft pulping applications.[46-50] The addition of extra monomers is simply used to enhance the base performance of carboxylic acid containing homopolymers. Secondly, the charge density (CD) of the polymer also influences scale control performance and is intimately connected to the first factor, the present functional groups, along with use conditions such as pH. This is apparent as the distinction between the performance of PMA separates itself from that of the PAA during the Parr reactions. It has been shown previously to have a definitively increasing effect on inhibition with increased CD for ozonized kraft

lignin, although not to the full extent desired for a feasible product.[24] Lastly, the molecular weight of the polymer antiscalants has been shown here to play a significant role in performance. At least here, with the Parr reactions and a wide variant of samples, increasing molecular weight results in a general decrease in the temperature required to induce rapid nucleation of $CaCO_3$. Chelation was *not* a sufficient explanation for the residual calcium levels, f_{120}, for higher molecular weight samples, at least at these lower concentrations. In order to design a more efficient $CaCO_3$ inhibitor it seems pertinent to investigate and isolate the molecular weight effects of the typical carboxylic acid containing homopolymer base, poly(acrylic acid) and its conjugate sodium salt, sodium polyacrylate, before developing new copolymers with a wide variety of additional monomers.

Degradation

For those in the industry involved with antiscalants used in kraft digester (and condenser) conditions, the question of antiscalant stability under these high temperature scenarios is a common question. In order to ensure that any MW effects upon inhibition performance were *not* linked to degradation of the polymer sample upon exposure to the extreme conditions of the kraft-digester, a quick study was used to investigate the implications of degradation on scale control. Gurkaynak and colleagues were the only ones found in the literature documenting thermal degradation of poly(acrylic acid) in aqueous solution, rather than in the bulk solid form.[51] As expected, they found that 2 different decarboxylation reactions were present depending on the ionization state of the carboxylic acid and that cleavage of the backbone was not responsible for the lowering of MW of the degraded PAA. For the ionized conjugate base form, their studies showed that the rate of decarboxylation increased with temperature and a decrease with salt concentration. Although pH and ionic strength values were not increased high enough to mimic kraft digestion conditions, their data does suggest an extremely low rate of decarboxylation of the polymer antiscalants throughout a kraft cook. In order to confirm that polymer degradation was not responsible for any MW effects on performance, a

couple of experiments were performed to show both degradation at low pH conditions and then no degradation at kraft conditions.

Upon degradation of a relatively large poly(acrylic acid) sample with a M_w of ~90,000 (90k PAA) in an aqueous pH 7 solution heated up to 160 °C, obvious degradation was observed. In Figure 2.11, the MWD of the PAA sample is shown just prior to and after 5 hours of heating. The distribution shifts drastically to the lower MWs. Figure 2.12 shows the degradation of the weight average molecular weight with respect to the amount of heating time. Only a slight degradation was observed while the reaction vessel was heating up, and then a drastic change in M_w occurred as the polymer underwent decarboxylation as the temperature was kept at 160 °C. Plotted as dashed lines in Figure 2.12 are the results for $CaCO_3$ inhibition studies using the degraded 90k PAA as the antiscalant. Once again, the drop in dissolved calcium with respect to vessel temperature was fit using Equation 11.b and the temperature at which the calcium in solution dropped by 15% was deemed the nucleation temperature, T_{nucl}. Surprisingly enough, despite a significant decrease in the MWD of the polymer as it was degraded, there was not a significant change in the nucleation temperature with respect to the degradation time of the polymer sample. Noting that the decarboxylation reaction was responsible for the decrease in MW while the backbone chain length remained constant suggests that the later has a stronger influence on $CaCO_3$ inhibition than the former. This in turn, helps explain why the chemical composition is less important than the MW of the antiscalant; the length of the backbone chain is highly related to the MW and plays the dominant role in performance (as long as *most* of the mers have carboxylic acid groups).

Once degradation was observed for these moderate solution conditions (pH 7, low ionic strength) the degradation conditions were changed to more closely resemble conditions present at a kraft pulping mill. In addition, the ~20,000 M_w sodium polyacrylate (20k Na-PAA) used was more representative of actual inhibitors used in mills. Degradation was conducted in a solution of dilute white liquor (92% causticity, 23 g/L effective alkali, and 25% sulfidity) at, again, 160 °C. Shown in Figure 2.11 are the MWDs of the 20k Na-PAA before and after heating for 5 hours. No significant change

occurred with degradation in the mock kraft conditions. This stability is also expressed in Figure 2.12 where the M_w dropped only slightly throughout the entire degradation experiment. Interestingly, as the slightly degraded samples were used in Parr $CaCO_3$ inhibition studies, the resulting T_{nucl} values seemed to remain constant although subject to more error. This is not representative of a nucleation temperature trend with degradation, but rather an unavoidable consequence of using un-processed solutions from the degradation experiment as the source of the antiscalant. Since the degradation samples introduced sulfide and extra NaOH alongside the polymer antiscalant, the resulting solutions used for the inhibition studies were not comparable to the previous studies using much cleaner initial conditions. Since separation of the degraded polymers from the degradation solution would have introduced an excess of unnecessary variables, the overall trend (or lack there of) was used to gauge whether or not degradation influenced inhibition performance. It can be concluded that degradation (in the form of decarboxylation) is not present to a significant extent and therefore not responsible for changes in MW and antiscalant performance during the kraft pulping process.

Conclusions

It has been shown through kraft digester and Parr bomb reactions, intended to mimic mill conditions for the digester and condensers respectively, that the molecular weight of the polymer antiscalant used to inhibit the growth of $CaCO_3$ deposits is important. The exact mechanism by which the antiscalants perform their scale control duties is still unclear as the complexity of the chemical processes occurring within the mill obstruct any decisive conclusions. In addition, the broad molecular weight distributions and presence of different, and often times multiple, functional monomers in commercial antiscalants increases the number of variables between experiment sets. It is clear that a carefully planned, simpler, experimental procedure eventually coupled with a more controlled sample set is required to illuminate the underlying mechanisms responsible for efficient polymeric antiscalants and the further design thereof. The next couple of chapters will outline some further methods intended to reduce the complexity of the system and the synthesis of a much more controlled set of poly(acrylic acid) samples.

Tables

Table 1.1 Listing of the sample compositions, weight average molecular weights, and kraft digester and Parr reactor results (for 10 ppm dosages).

		Kraft (10 ppm)		**Parr (10 ppm)**		
Sample Name	**M_w (g/mol)**	***kA***	**c_∞**	**T_{nucl} (°C)**	**f_{120} (%)**	**General Composition**
C-1	1,540			83	4%	Poly(acrylic) Acid
C-2	1,600			84	6%	Poly(acrylic) Acid
C-3	2,700			78	7%	Poly(acrylic) Acid
C-4	3,900			77	4%	Poly(acrylic) Acid
C-5	4,500			79	4%	Poly(acrylic) Acid
C-6	6,000			60	5%	Poly(acrylic) Acid
C-7	10,000	0.0021	2.5072	78	7%	Poly(acrylic) Acid
C-8	12,600			75	5%	Poly(acrylic) Acid
C-9	237,000			67	8%	Poly(acrylic) Acid
C-10	1,600			73	14%	Sodium polyacrylate
C-11	1,600			59	2%	Sodium polyacrylate
C-12	5,100			59	3%	Sodium polyacrylate
C-13	5,800			82	7%	Sodium polyacrylate
C-14	6,400			77	6%	Sodium polyacrylate
C-15	38,100	0.0053	4.0074	56	10%	Sodium polyacrylate
C-16	67,700	0.0050	4.1087	55	13%	Sodium polyacrylate
C-17	105,000			80	8%	Sodium polyacrylate
C-18	3,500			74	4%	Ammonium polyacrylate
C-19	6,900			58	2%	Acrylic acid & Sulfonic acid & nonionic terpolymer
C-20	2,500	0.0029	8.9566	101	12%	Acrylic acid & Sulfonic acid & nonionic terpolymer, Na salt
C-21	15,500			58	3%	Acrylic acid & Sulfonic acid copolymer
C-22	25,500			42	5%	Acrylic acid & Sulfonic acid copolymer
C-23	3,000	0.0037	3.4022	83	13%	Maleic acid terpolymer, Na salt
C-24	3,500	0.0035	2.5654	64	13%	Maleic & acrylic acid terpolymer, Na salt
C-25	460	0.0059	11.7013	99	25%	Poly(maleic) Acid
C-26	590	0.0056	0.0034	112	26%	Poly(maleic) Acid
C-27	1,400	0.0075	4.3890	98	23%	Poly(maleic) Acid
C-28	3,500	0.0014	2.5567	83	2%	Phosphinocarboxylic acid
C-29	3,700	0.0036	10.4059	71	5%	Phosphinocarboxylic acid
C-30	2,900			83	-1%	Sodium phosphino polyacrylate
C-31	17,600			45	3%	Sodium polymethacrylate
C-32	15,000			57	4%	Ammonium polymethacrylate
C-33	12,500			77	7%	Copolymer, Na salt
C-34	17,500	0.0014	2.5195	33	13%	Copolymer, Na salt
C-35	3,700	0.0014	1.6362	69	5%	Proprietary
C-36	4,200	0.0036	6.0364	64	3%	Proprietary
C-37	95,100	0.0048	3.1390			Proprietary

Figures

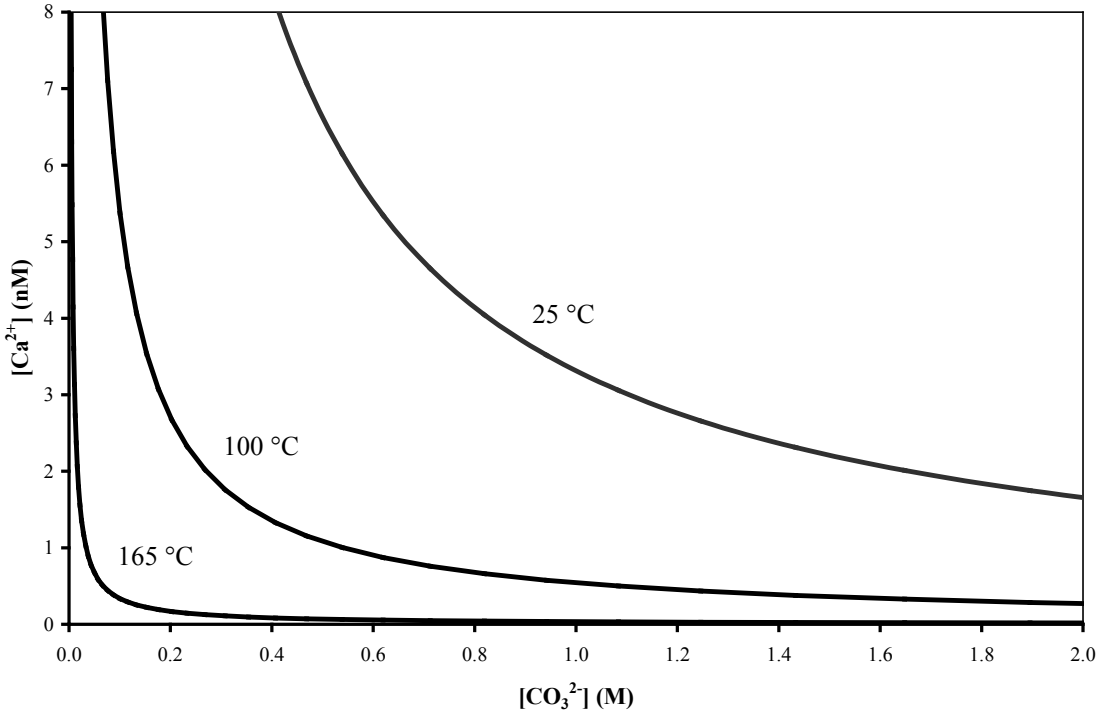

Figure 2.1 Solubility curves for calcite at various temperatures pertinent to the kraft pulping process. Solubility constants as a function of temperature were generated from the literature.[9]

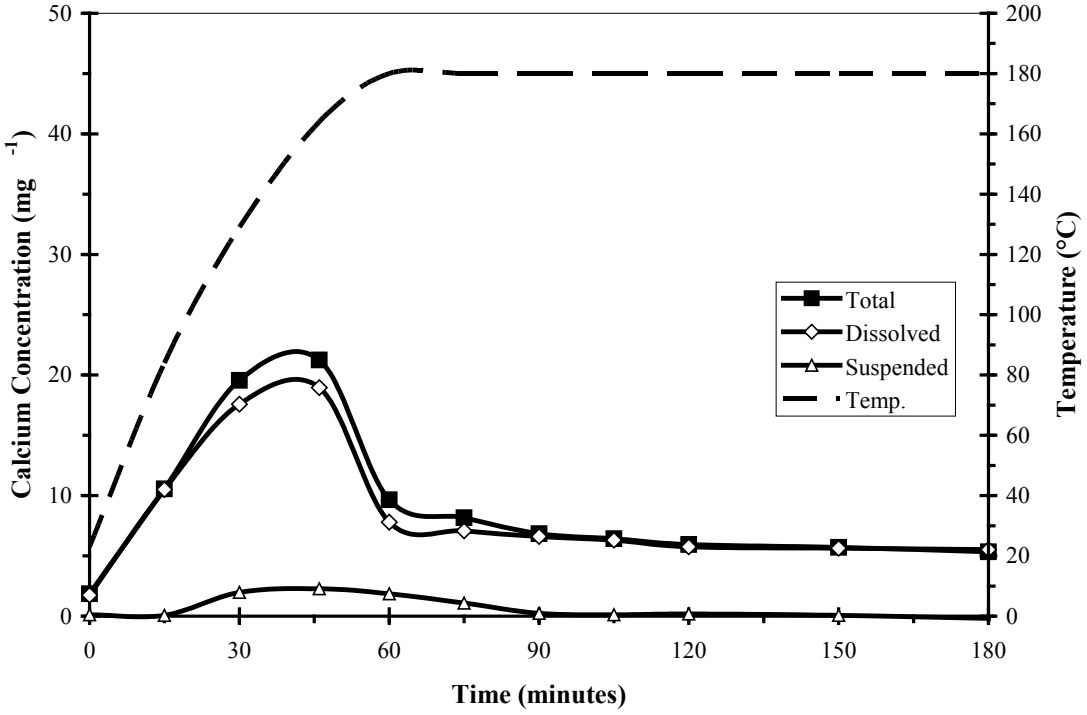

Figure 2.2 Total (■), dissolved (◊), and suspended (Δ) calcium levels in a typical control kraft digestion (no inhibitor) with temperature ramping up to 180 °C shown as dashed line.

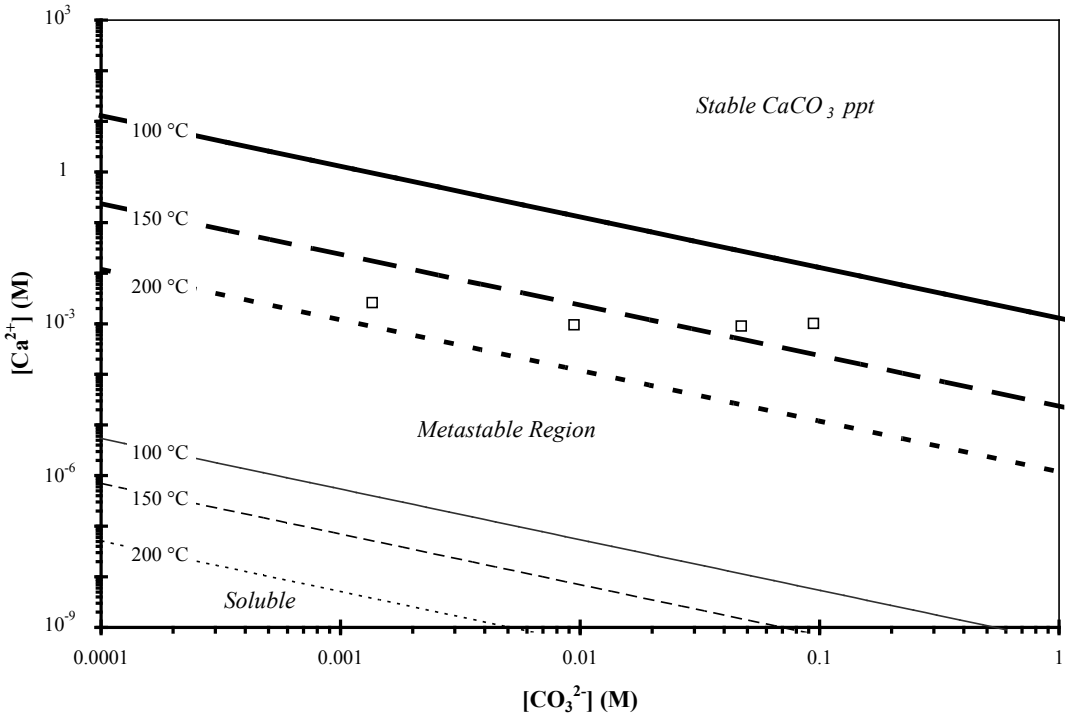

Figure 2.3 Solubility curves (in log-log form) alongside kraft digester nucleation points with various CO_3^{2-} concentrations representing the estimation for the metastable regions of Ca^{2+} and CO_3^{2-} ions at various temperatures.

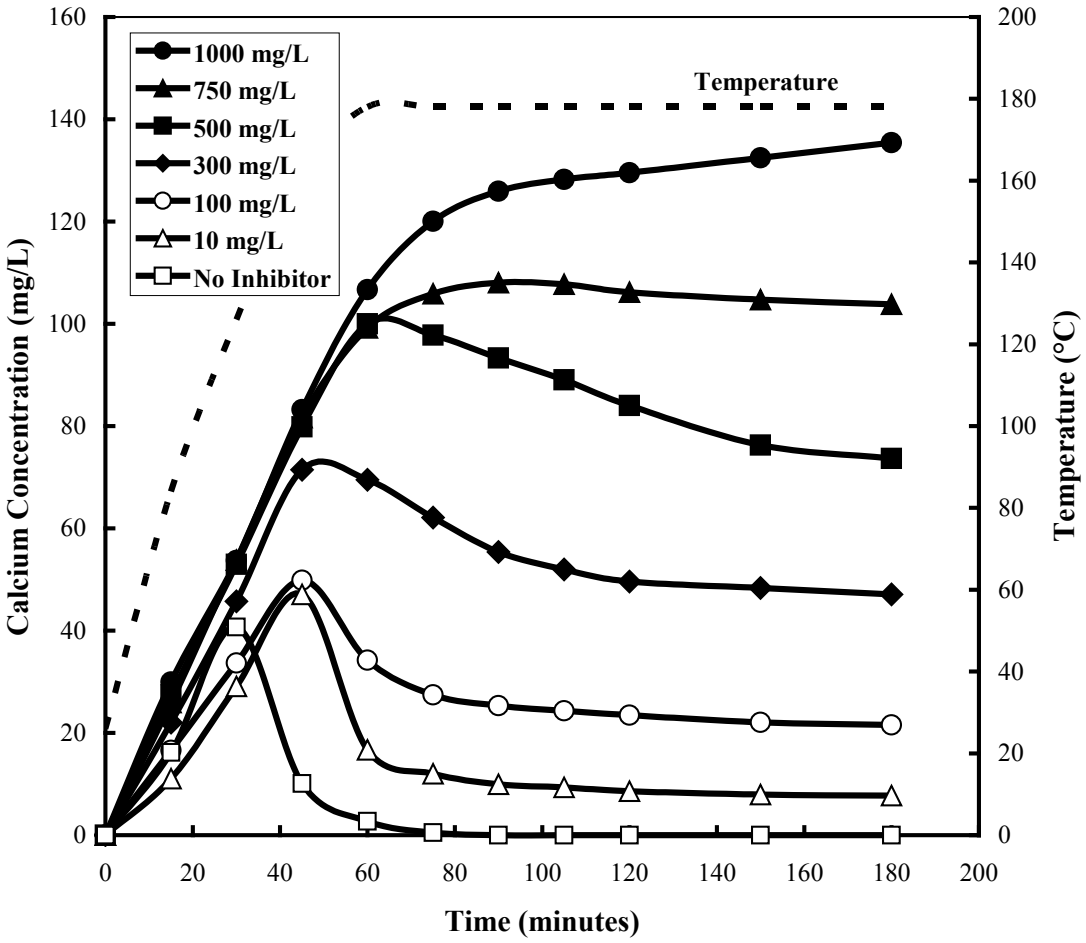

Figure 2.4 Solution concentrations of dissolved Ca^{2+} during a kraft cook experiment with varying concentrations of EDTA used to inhibit $CaCO_3$ precipitation.

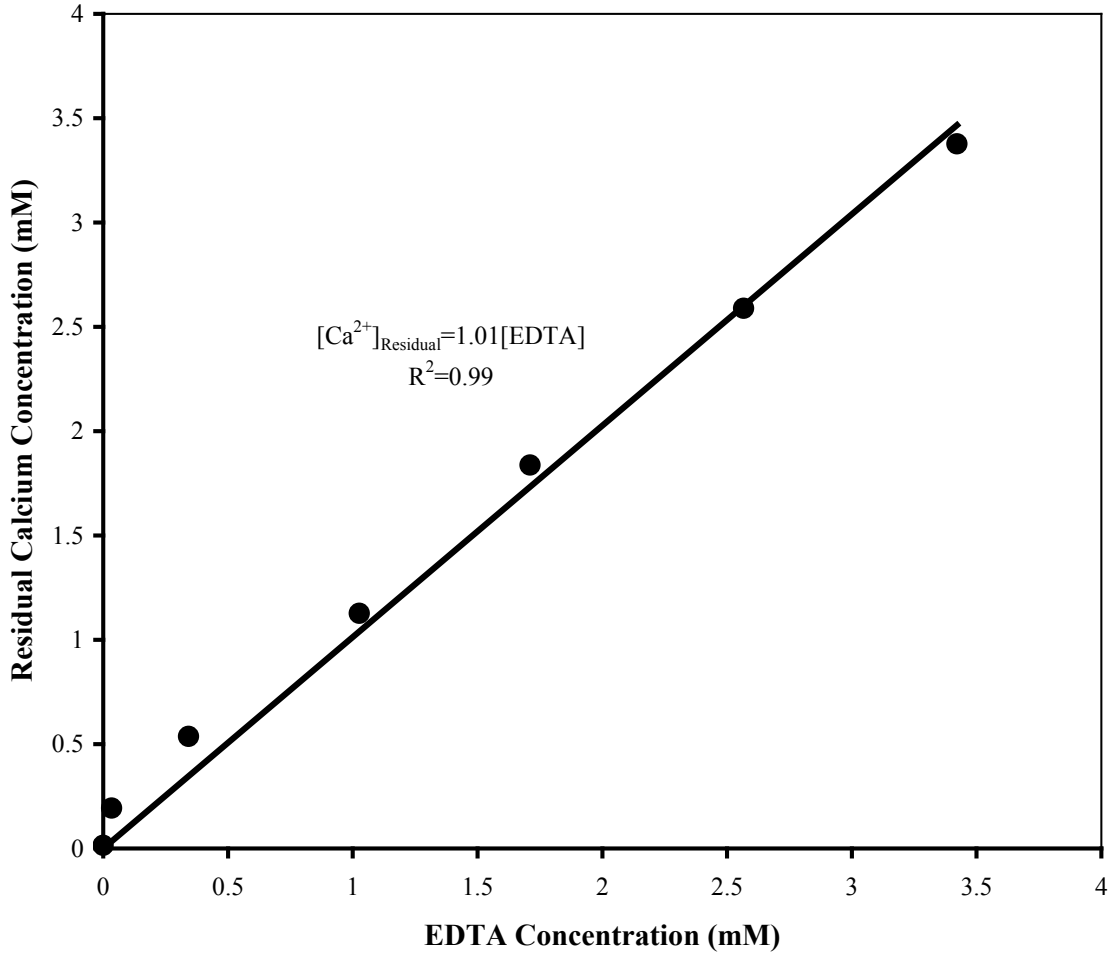

Figure 2.5 The direct correlation between the molar concentrations of residual Ca^{2+} left in kraft liquor after digestion and the concentration of EDTA added before digestion.

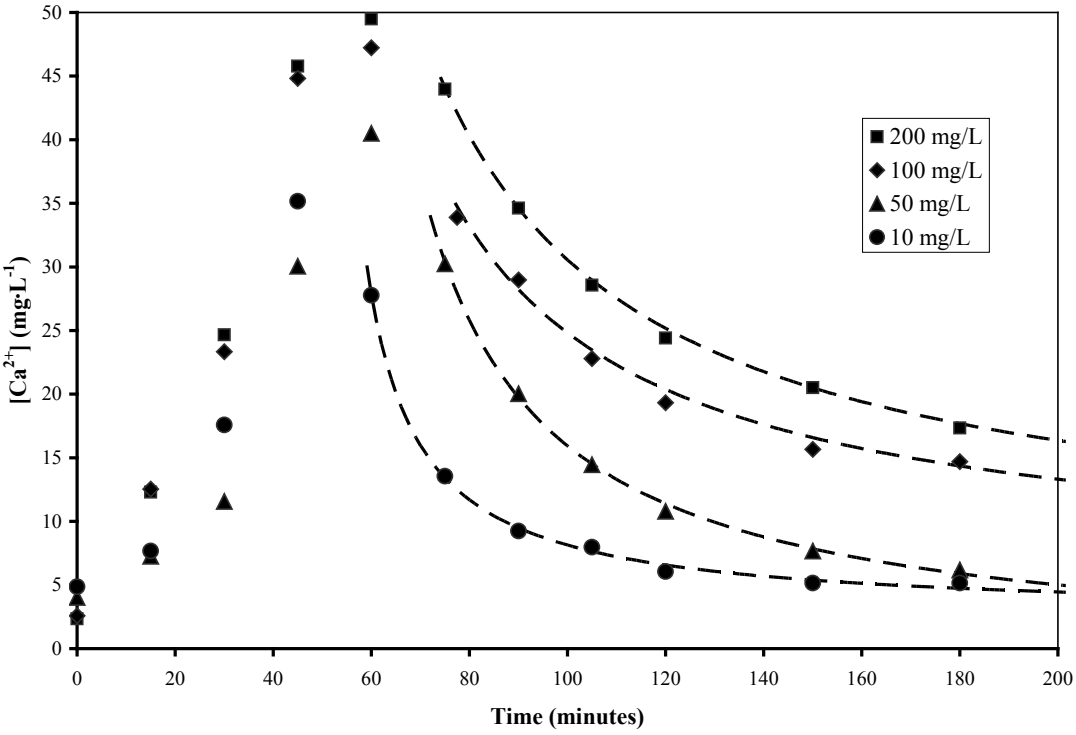

Figure 2.6 Solution concentrations of Ca^{2+} during a kraft cook experiment with varying concentrations of the industry benchmark, C-24, used to inhibit $CaCO_3$ precipitation. Dashed lines indicate the 2nd order rate fits.

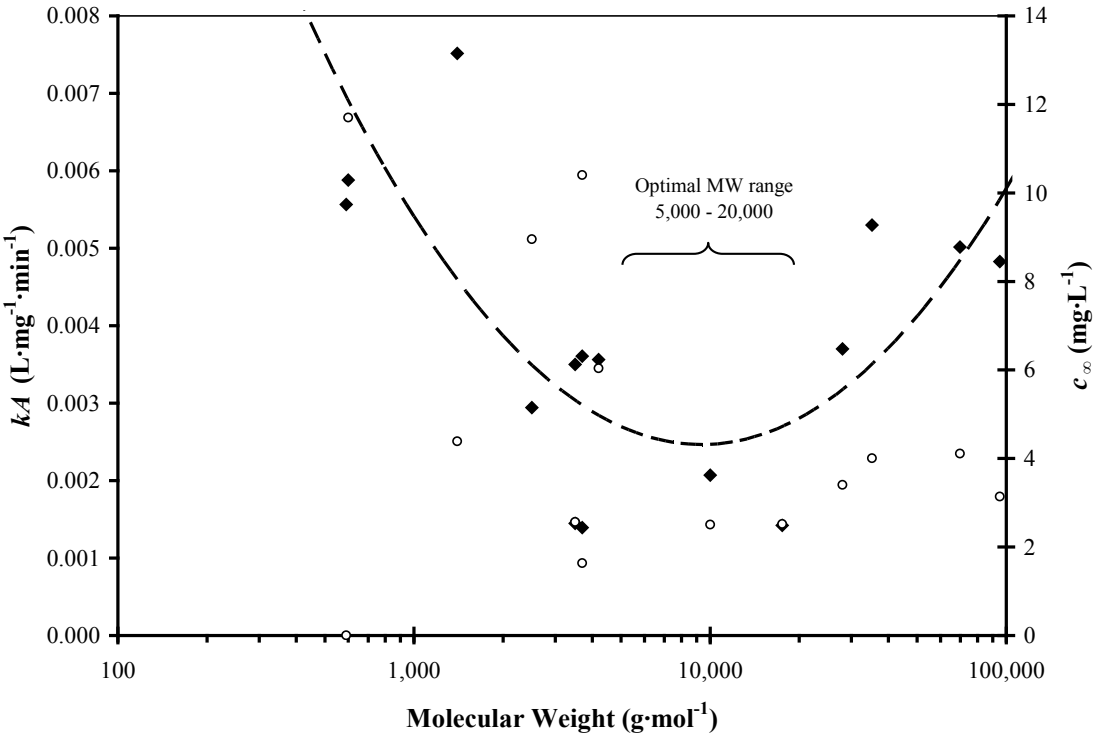

Figure 2.7 Correlation between kraft digester Ca^{2+} fitting constants *kA* (♦) and c_∞ (○) with respect to the molecular weight (M_w) of commercial samples tested at 10 mg/L.

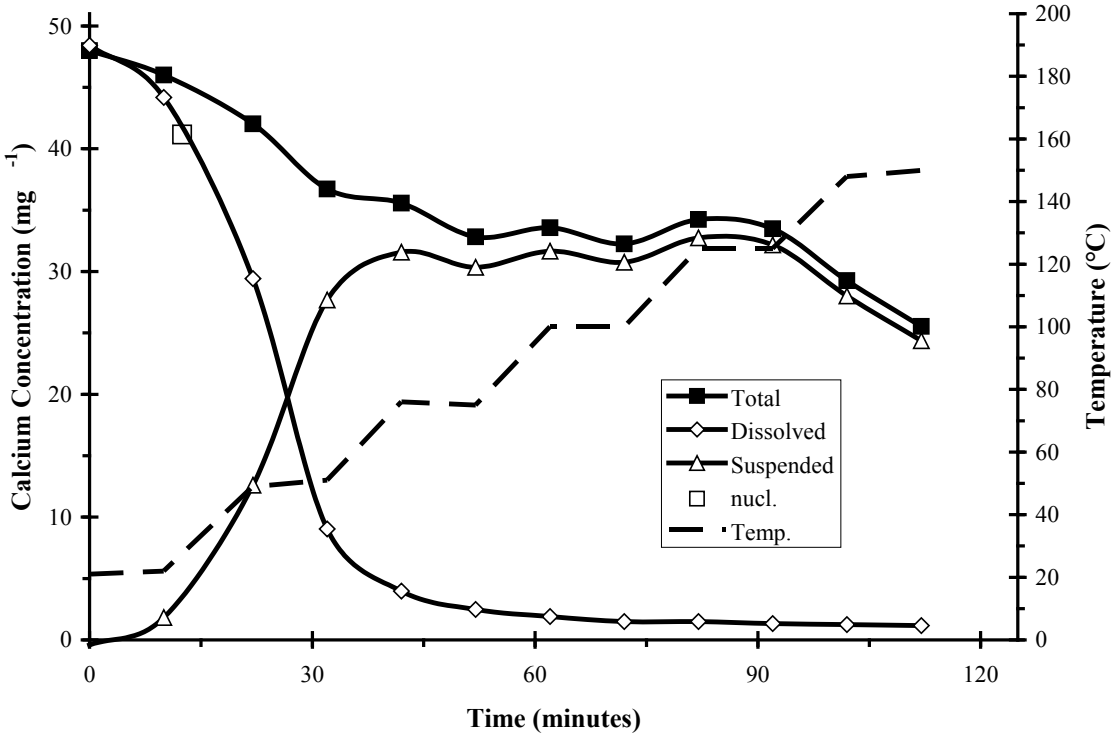

Figure 2.8 Total (■), dissolved (◊), and suspended (Δ) calcium levels in a typical control Parr reactor (with no inhibitor) initially containing 50 mg/L of calcium (as $CaCl_2$), 1 g/L Na_2CO_3, and 5 g/L NaOH. The heating sequence (shown as a dashed line) involved heating the liquor by ~2 °C/min and then keeping temperature constant (at 25, 50, 75, 100, 125, and 150 °C) for 10 minutes before ramping up again. The point at which dissolved calcium levels dropped by 15% is shown as the nucleation point (□).

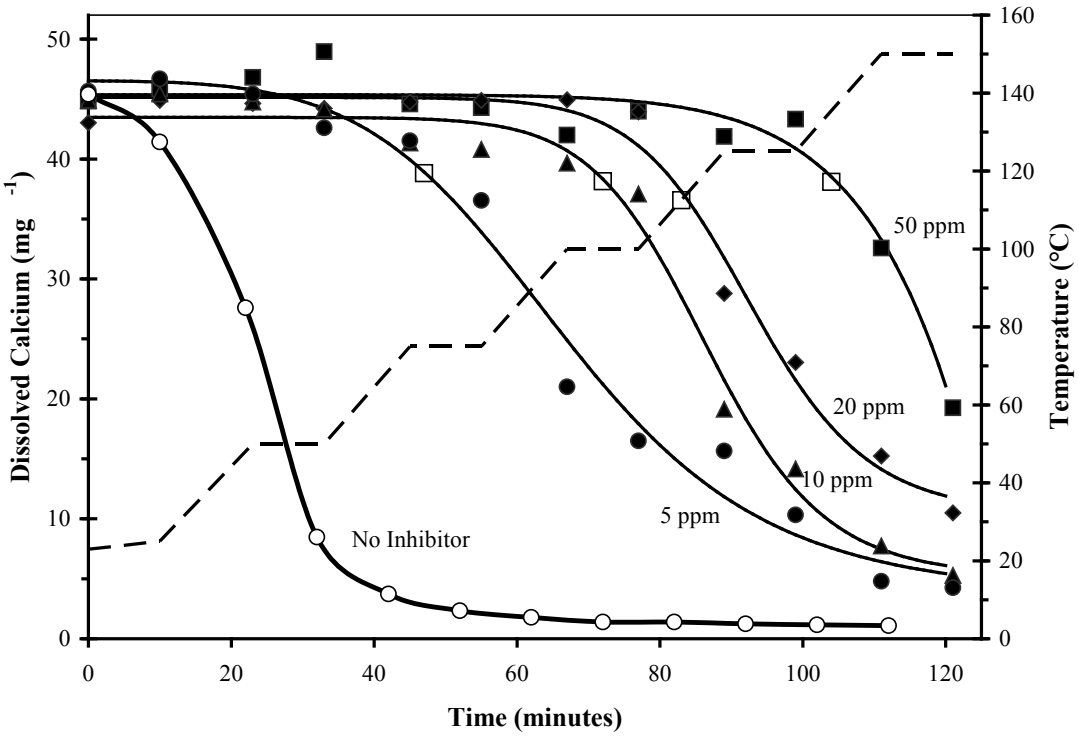

Figure 2.9 Dissolved calcium as a function of time/temperature in a Parr reactor initially containing 50 mg/L of calcium (from $CaCl_2$), 1 g/L Na_2CO_3, and 5 g/L NaOH with no inhibitor and various concentrations of C-20. Reactor temperature is shown as a dashed line with respect to time. Non-linear fits based on a 2nd order rate law for crystal growth with a temperature dependent rate constant are shown as solid lines for the various concentrations of inhibitor with nucleation points (□) where dissolved calcium levels dropped by 15%. The 50 ppm dose curve is shown as an example of an absence of a "tail" portion yielded a poor-fit of the data.

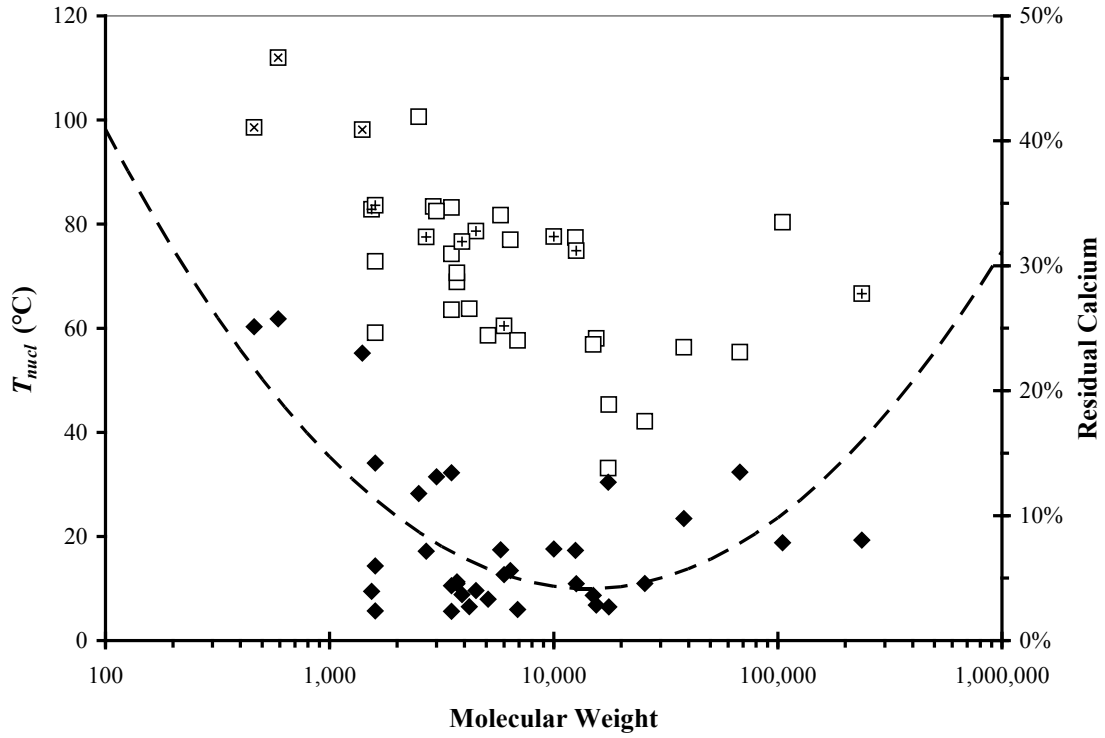

Figure 2.10 Nucleation temperatures (□) and residual calcium amounts at 150 °C (♦) relative to the molecular weight of the inhibitor used. A simple second order polynomial fit (with respect to the logarithm of MW) is shown as a dashed line suggesting an optimal MW range surrounding 10,000 g/mol. T_{nucl} values for poly(maleic acid) and poly(acrylic acid) samples are expressed with × and + marks respectively.

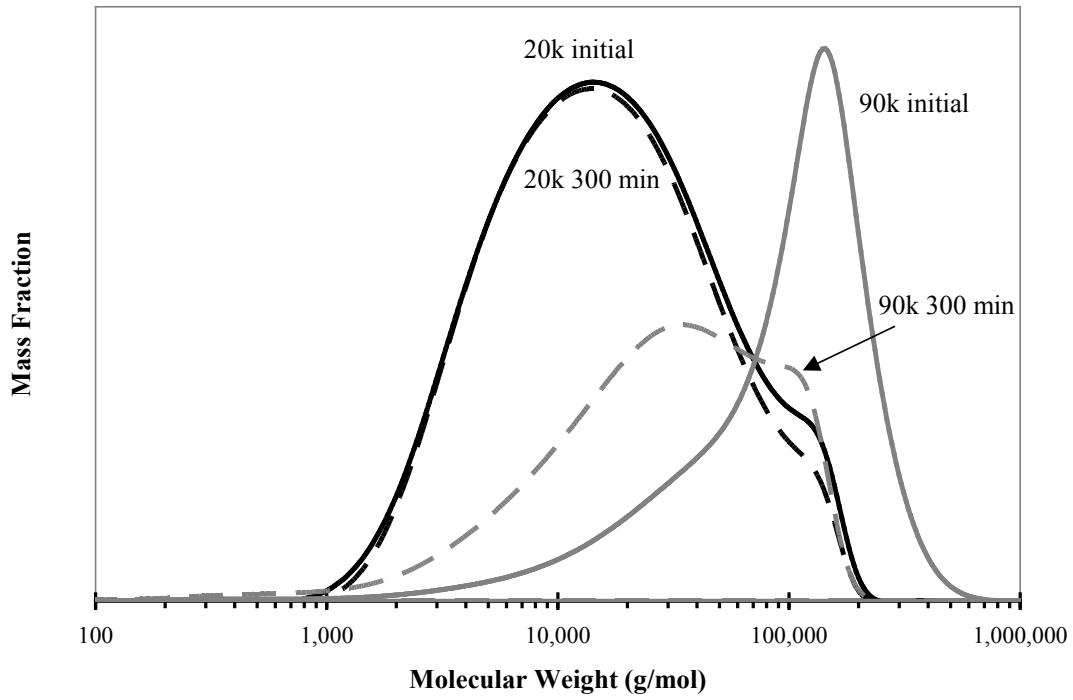

Figure 2.11 The slight change in the molecular weight distribution of ~20,000 MW Na-PAA before (solid line) and after (dashed line) degradation under kraft-like conditions (160 °C, pH > 14, and 25% sulfidity). Also, the drastic degradation of ~90,000 MW PAA before (solid gray line) and after (dashed gray line) degradation in more moderate conditions (pH 7, no Sulfide).

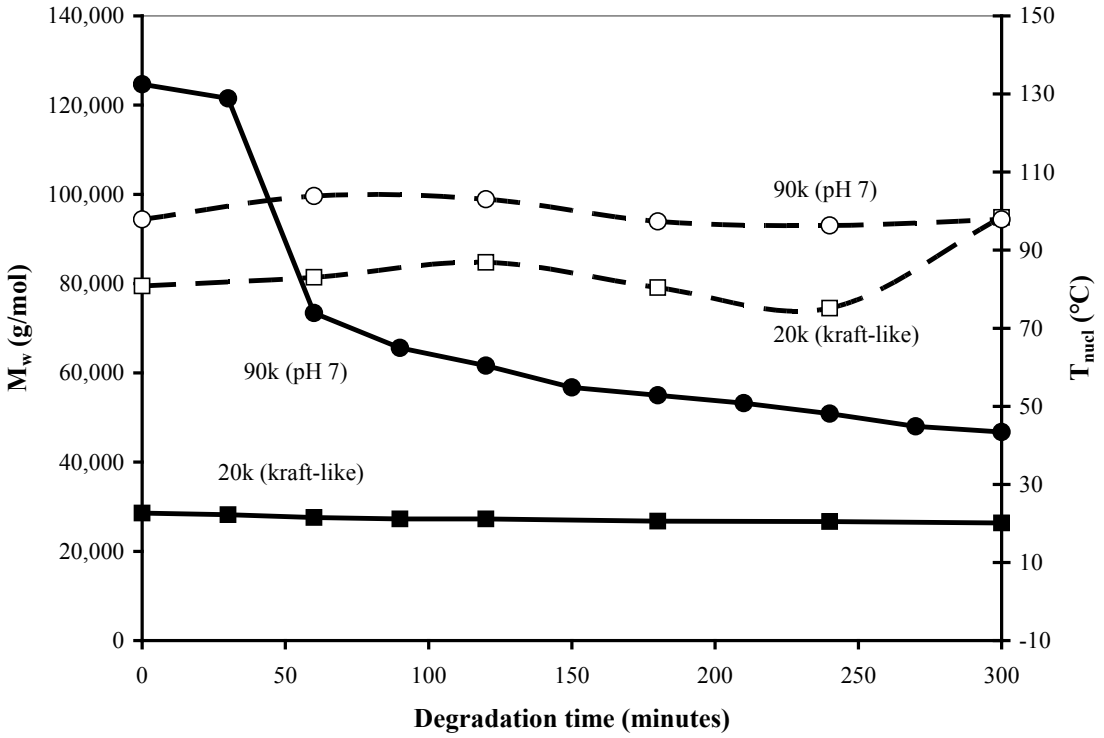

Figure 2.12 The change in M_w for the 90,000 MW PAA (solid line with ●) and 20,000 MW Na-PAA (solid line with ■) samples with respect to degradation time in pH 7 solution void of sulfide and kraft-like conditions, respectively. Dashed lines show the nucleation temperatures when the same degraded samples (90k ○, 20k □) were used in $CaCO_3$ inhibition studies.

Chapter 3 – Commercial PAA Inhibition of $CaCO_3$

Introduction

The formation of $CaCO_3$ scale in kraft digesters and black liquor evaporators has always been an issue for kraft pulping mills.[31] It has been well documented that the $CaCO_3$ scale is formed by precipitation from the supersaturated liquor with calcium and carbonate species predominantly originating from the wood chips and white liquor, respectively, and not from unsettled lime mud carried over from the re-causticizing process of the white liquor.[7, 31] Scale deposits on the heat transfer surfaces of both digesters and evaporators act as an insulator in terms of heat transfer rates, ultimately requiring increased energy consumption in order to maintain a constant temperature.[3] This increase in operational costs along with unscheduled shutdowns and cleaning costs forces mills to seek dependable methods for scale prevention or reduction. Antiscalants have certainly been used to effectively eliminate deposited mineral salts in other industrial process waters,[10, 52, 53] and sodium polyacrylate based dispersants in particular have been used with limited efficiency for the case of kraft digesters and evaporators for more than 40 years.[24]

Even though polyacrylate based polymers have been investigated for their antiscalant properties for some time now, their mechanism of inhibiting nucleation and growth is still uncertain.[23] Currently, the effects of molecular weight are of interest. An optimum molecular weight with regards to inhibition efficacy has been suggested[23, 54] and documented[24, 44] as a balance of increasing adsorption amounts and decreasing adsorption rates of polymer additives with increasing molecular weight. Ideally, mechanistic investigations would be held under kraft digestion conditions, but the complexity of the system makes this possibility unreasonable. It has been attempted here to simplify the system in which $CaCO_3$ scale is forming in order to elucidate some of the mechanisms responsible for the efficacy of poly(acrylic acid) (PAA) and sodium polyacrylate (Na-PAA). In order to limit the number of factors influencing the inhibition efficacy of the polymers' molecular weight (MW), a simple sample set composed of homopolymers of

PAA and Na-PAA ranging from less than 2,000 M_w to nearly 300,000 M_w was employed. In addition, the conditions were brought down to more moderate conditions while the nucleation and growth of the $CaCO_3$ was monitored with an in-situ technique. Nucleation and crystal growth were monitored using focused beam reflectance measurement (FBRM) where a beam of laser light is focused out in the solution a certain distance (nominally 20 μm) from the probe window and spun at 75 Hz (2 m/s velocity). A schematic drawing of the FBRM probe is shown in Figure 3.1. The spinning of the optics allows the focused point to move through a circle in a plane parallel to the sapphire probe window. As the beam moves through the solution, any backscatter is detected from particles it passes over. The FBRM hardware analyzes the backscatter signal to determine the number of particles observed and the distance the beam has traveled over each particle, thus measuring a chord length for each particle observed. Thus, FBRM can only provide a chord length distribution (CLD) and not an actual particle size distribution (PSD). A number of researchers have worked to enhance the conversion of CLDs into PSDs but the overall issue of requiring fairly well defined particle geometry in order to calculate the PSDs from the CLDs remains.[55-60] In contrast, the overriding advantage to the FBRM setup is the ability to gather in-situ measurements of crystal growth. In this case, nucleation of $CaCO_3$ can accurately be gauged by setting an arbitrary (but relatively low) number of chord lengths counted per second as the point where nucleation is deemed to occur. This is reasonable since crystal growth progresses rather quickly after stable nuclei have been formed.

Materials and Methods

Chemicals and Materials

Inorganic materials including anhydrous Na_2CO (CAS #497-19-8), NaOH (50% $^w/_w$ CAS #1310-73-2), anhydrous $CaCl_2$ (CAS #10043-52-4), and HCl (CAS #7647-01-0) were purchased from Sigma-Aldrich (St. Louis, MO) as reagent grade chemicals. Poly(acrylic acid) and its neutralized salt form, sodium polyacrylate, were purchased from Polysciences Incorporated (Warrington, PA) as solutions with concentrations ranging from 20 to 63% $^w/_w$.

Solutions

The initial solutions were prepared as 1 g/L Na_2CO_3 (9.4 mM CO_3^{2-}), 1 g/L NaOH (25 mM, pH 12), and varying concentrations of polymer additives from 1 to 50 mg/L (active acids). The calcium solution used was prepared from $CaCl_2$ to produce a concentration of 1 g/L Ca^{2+} (2.77 g/L $CaCl_2$, 25 mM Ca^{2+}). All solutions were prepared using 18 MΩ "doubly" de-ionized water (DDI H_2O).

Experimental setup

The temperature controlled experiments were conducted in an 800 mL jacketed beaker with a Neslab RTE-111 water cooler used to maintain experimental temperatures within 0.1°C.

500 mL of the initial solution was added to an 800 mL beaker and the various probes were submerged while stirring was commenced at 400 rpm via an overhead stirrer. The calcium solution was dripped into the stirred solution at 0.6 mL/min via a 7550-90 Masterflex (Cole-Parmer Instrument Company, Vernon Hills, IL) peristaltic pump. Chord length distributions of $CaCO_3$ particles were gathered using FBRM. A Lasentec D600L (Mettler-Toledo Inc., Columbus, OH) FBRM probe and hardware were used to collect all chord length distribution data (0–100 μm in 200 linear channels) until the total sum of chord length counts was at least 2000. Scanning electron microscope (SEM) images were collected (using a nominal accelerating voltage of 5 kV and an initial working distance of 8 mm) on a JEOL (Tokyo, Japan) 6500 Field Emission Gun – Scanning Electron Microscope. Crystal samples were collected during the crystallization experiments by extracting 1 mL of the solution and centrifuging for approximately 10 minutes before preparing the SEM sample.

Results & Discussion

Where chapter 2 discussed the Parr reaction experiments which varied supersaturation levels by increasing the temperature and holding the formal calcium concentration constant, this chapter increases the $CaCO_3$ supersaturation level by increasing the calcium concentration while holding the temperature constant.

Shown in Figure 3.2 is the FBRM monitored particle count as a function of the calculated formal Ca^{2+} concentration for a typical experiment with no inhibitor added. It should be noted that the FBRM count does not represent the total number of particles in the system, rather a time concentration of particles passing through the laser's field of view. An arbitrary level of 200 counts/sec was used to signify the critical calcium concentration and is denoted in the figure as an open circle (○). The calcium level at which the FBRM read 200 counts/sec is used throughout this chapter as the critical calcium level required to induce nucleation of $CaCO_3$. Varying the original CO_3^{2-} concentration from 0.1 to 3.0 g/L Na_2CO_3 and measuring the point at which nucleation occurs expresses the existence of a metastable region similar to that seen for the kraft digester and Parr experiments of chapter 2. The metastable region where Ca^{2+} and CO_3^{2-} ions exist at levels above supersaturation for $CaCO_3$ is shown in Figure 3.3. As with the more complex systems in chapter 2, the critical point at which nucleation occurs at a rapid rate is orders of magnitude higher in concentration than where the solubility curve lies. As before, the extent of this metastable region where a separate $CaCO_3$ phase is thermodynamically favorable but the system lacks the thermal energy required to overcome the energy created by the surface of the new phase, is dependent on temperature. To express this more fully, Figure 3.4 shows the relative particle concentration vs. calcium concentration for varying temperatures. Here, the initial solution CO_3^{2-} concentration remained at a constant 9.4 mM (1 g/L Na_2CO_3) but the temperature was held at a different value for each experiment expressing the dependence of the nucleation concentration of Ca^{2+}, c_{nucl}, upon temperature. Using the temperatures at which each experiment was held along with the concentrations of Ca^{2+} and CO_3^{2-} at the nucleation point and classical nucleation theory, the data can be modeled by Equation 4 from Chapter 2. Expectedly, plotting $T^{-3/2}$ versus the natural logarithm of the product of calcium and carbonate concentrations, a linear relationship is found as shown in Figure 3.5.

Figure 3.6 shows the molecular weight distributions (MWDs) for the homopolymer sample set chosen in this chapter for its simplicity over the commonly implemented copolymers currently used to inhibit scale in mills, which were examined in Chapter 2.

Since most polymeric antiscalants are produced via the free radical polymerization of multiple monomers (typically including large molar fractions of acrylic acid and/or maleic acid), their polydispersity indices (PDIs) are rather large with their MWDs lacking a unimodal distribution. The MWs and PDIs tabulated in Table 3.1, along with the SEC spectra from Figure 3.6, show these commercial samples to represent typical polydispersity trends for PAA and its sodium salt counterpart when polymerized via free radical polymerization.

As described above, the in-situ observation of nucleation and growth processes via FBRM allow for a precise measurement when using the simple sum of counted particles as the nucleation determinant. Monitoring the chord length distributions (via FBRM) of the $CaCO_3$ crystals precipitated upon the addition of Ca^{2+}, provided an abundance of data which was consolidated in two adjacent methods.

Particle concentration

The first method encompassed a simple sum of all counts over all the channels (histogram bins for recorded chord lengths) that the FBRM was monitoring. This sum was plotted against time, or formal Ca^{2+} concentration, for all polymers tested over a broad range of initial polymer concentrations (nominally 1 – 50 mg/L). This total sum can be thought of as a relative particle concentration with an example of a single polymer sample as characterized at different concentrations being shown in Figure 3.7 for the 10k-Na-PAA sample. Overall, the concentration of polymer added increased the amount of Ca^{2+} required for nucleation to occur at 25 °C. The discrepancy to the overall trend occurs in the Na-PAA concentration range of 8 to 20 mg/L where the correlation between concentration and inhibition efficacy is no longer present. In order to isolate and accentuate the relationship between polymer concentration and $CaCO_3$ inhibition, a dosage-performance curve provided a more consolidated view of the results.

Using 200 counts/sec as the deemed critical point of nucleation for all polymer samples, the required Ca^{2+} concentrations to initiate precipitation of $CaCO_3$ were taken and plotted against the initial polymer concentrations to produce *only the positions* of the data points shown in the performance curves of Figure 3.8 and Figure 3.9. It is clear that

the non-injective nature of the correlation between polymer concentration and critical Ca^{2+} concentration is not limited to just the 10k-Na-PAA sample expressed in Figure 3.7. Rather, a local maximum is observed for all PAA and Na-PAA samples with a weight average molecular weight (M_w) of ~25,000 or lower. All samples with higher MWs expressed a more direct relationship between concentration and performance over the tested concentration range. This difference in the shape of the performance curves between different molecular weights of PAA and Na-PAA samples is very convincing evidence that the dominant mechanism for inhibition of $CaCO_3$ depends on the MW of the antiscalant. It should be noted that the peculiar shape for the performance curves for the lower MW samples tested here has been noticed and documented previously by Loy *et al.* for the case of $CaCO_3$ nucleation and growth in the presence of polyacrylates at high pH.[44] Their ordinate plotted nucleation temperature rather than Ca^{2+} concentration but the overall method of increasing the system's supersaturation level remained similar to the experiments described in this chapter. They reasoned that fractionation of the polydisperse Na-PAA samples, with significant mass fractions at 5,000 – 6,000 MW, was responsible for these local maxima around 15 mg/L. For the results shown here, it is reasonable to suggest the same mechanism of fractionation is responsible for the local maxima at ~8 mg/L PAA (and Na-PAA). Re-casting some of the concentrations represented in Figures 3.8 and 3.9 and plotting the critical calcium concentrations with respect to the weight average molecular weight, M_w, of the polymer tested allows for the molecular weight dependence of inhibitor performance to be plotted as shown in Figure 3.10. The higher MW samples (those with $M_w > 40{,}000$) show a slight decrease in performance as the MW was increased at concentrations less than 20 mg/L. At initial polymer concentrations above 20 mg/L, the inhibitory performance showed the converse, an increase with MW. The lower MW samples (those with $M_w < 40{,}000$) which expressed the local maxima in their dosage-performance curves showed a more complicated trend with respect to MW. An optimal weight average molecular weight range from ~3,000 to 10,000 was expressed over all concentrations with the largest increase in $CaCO_3$ inhibition relative to the surrounding M_w's being at 3 mg/L initial concentration. Of course, the local maxima present in the dosage-performance curves in

Figures 3.8 and 3.9 expressed themselves here as overlap and cross-over of the critical calcium curves for 8 and 15 mg/L initial concentrations. The critical calcium levels detected by the FBRM was higher (around the optimal MW range) at 8 mg/L initial concentrations than the critical calcium levels for experiments possessing the higher initial antiscalant concentration of 15 mg/L. Thus, the 5k-PAA sample expressed the largest inhibition effect at its local maxima and lower concentrations. The other low MW samples expressed a decrease in performance as their MWs strayed from this optimal MW represented by the 5k-PAA sample with a MWD yielding an M_w of just under 5,000 and a PDI of nearly 2.5. It is clear from Figure 3.10 that there is a dependency upon the MW of the antiscalant with regards to performance. In addition, from Figures 3.8 and 3.9, it is clear that within this optimal MW range, the efficiency (or the slope of the dosage-performance curve) is highest at dosage levels only up to 8 mg/L. Upon further increases of polymer concentration, the critical calcium levels not only drop (after the local maxima) but require much more polymer to increase the critical calcium level by same amount.

CLD analysis

Consolidating the data collected by the FBRM and using a single point from each experiment implementing a different initial concentration is useful in terms of creating a dosage-performance curve, but the FBRM yields much more information about the system which can also be exploited. At any given time (or formal Ca^{2+} concentration), the FBRM accumulates and records every chord length it detects from the backscattered LASER light. This information is consolidated into histograms (with 100 channels or "bins") for efficient data storage. Thus, the difficulty resides in processing this large amount of data and eventually comes down to discerning the importance of the analyses. In addition to the first method aimed at consolidating the data and generating performance curves, the entire FBRM data set for each polymer concentration was plotted with chord length distributions (CLDs) along the abscissa and time along the ordinate as shown in Figures 3.11 and 3.12. In these intensity charts, the darkness of the plotted data points (pixels) represents the recorded number of chord lengths (or

"intensity") for that particular channel or size range of chord lengths. In Figure 3.11 where data from the experiment using 20 mg/L 10k-Na-PAA is plotted, a skew normal (un-symmetrical Gaussian) distribution emerges, which is characteristic of CLDs plotted on a linear range of chord lengths, and increases in amplitude with time, representing an increase in particle concentration within the solution. Knowing from the first method that the $CaCO_3$ growth proceeds rapidly after nucleation, it comes as no surprise that the amplitude (and over-all sum) of the distribution increases from essentially zero rather quickly. For this reason, the ordinate scale does not begin at time zero, because no relative intensity is recorded before nucleation.

At selective initial concentrations of polymer, entirely different looking intensity charts were observed. A typical example is shown in Figure 3.12 where a lower initial polymer concentration of 5 mg/L 10k-Na-PAA was used. Here, there appears to be an underlying low intensity skew normal distribution base with a number of extremely localized peaks added to it. It could be speculated that these intense peaks originate from the presence of discrete and highly monodispersed crystals within the solution. If this were the case, any decrease in the size of the chord length channel where the peak resides with respect to time would imply that all of the monodispersed particles were decreasing in size at nearly exactly the same rate, which is highly improbable. Also, even a discrete set of monodispersed particles would still exhibit a broad distribution of chord lengths as measured by the FBRM leaving this speculation in error. Another, more consistent postulate comes from the disposal of the assumption that the FBRM data represents solely the CLDs of particles suspended in the solution. Thus, the pixelated CLD plot of Figure 3.12 depicts where single crystals on the FBRM probe window were counted and recorded by the FBRM hardware on every cycle of the optics. As to whether the single crystals nucleated on the window or in solution before adhering to the window is uncertain. It is assumed that surface nucleation at the probe window is responsible since most of the distinct peaks originate at the smaller chord length channels and progress steadily towards the larger chord length channels. It is clear however, that the peaks in the CLDs are *not* a representation of a majority of very monodispersed crystals (of unique size) suspended in solution. The simple sum of the counts/sec of each individual peak

being around 75 (within error) and the knowledge that the optics of the FBRM unit spin at 75 Hz make this coincidence unbelievable. (This was also experimentally shown in separate lengthy experiments where the probe (showing distinct peaks) was removed from the crystal growth beaker, washed with HCl, rinsed clean, and dried before replacing it back in the beaker where it no longer detected distinct peaks but only the broad underlying distribution.) According to the work of Worlitschek and Mazzotti,[61] a non-moving particle detained in the path of the rotating laser yields a distinct signal with exactly the same count number as the frequency of the rotating optics. In addition, they also report a visibility window of up to 2.5 mm from the focal distance as measured parallel to the probe axis. This leaves the sapphire probe window, in this case 20 μm from the focal plane, easily within the detectable region of the FBRM. From the information gathered via the second method, all of the data points in Figures 3.8 and 3.9 could be classified as either "surface" or "solution" nucleation with the designations assuming the location of the observed particles was also that of their initial nucleation. Classification depended on the presence or lack of distinct peaks for the CLD at which nucleation was considered to have begun (>200 counts/sec) at the critical point. Shown in Figure 3.13 are the CLDs over the lower third of the channels monitored at critical Ca^{2+} concentrations for both the initial 10k-Na-PAA concentrations of 5 and 20 mg/L cases. The distribution for the solution nucleation case (20 mg/L) is shown as a solid gray line with a Gaussian distribution fit to the logarithm of the chord lengths as a dashed gray line, which is supported in the literature.[62] The data fits the Gaussian distribution well and expresses an inherent noise with a root-mean-square (rms) of the residuals over all channels to be less than 1.1 counts/sec and less than 2.5 counts/sec over the lower third of the channels. The solid black line in Figure 3.12 is the CLD for the surface nucleation case (5 mg/L) and the dashed line is the Gaussian distribution fit of all the points not representative of the crystals on the FBRM probe window. The points determined to be represented by crystals on the FBRM probe window are shown as squares (□) with vertical lines dropping down to the Gaussian fit of the underlying solution phase particles. Here, each square data point is the actual recorded number of particles per second and their lines representing those particles that are being counted by

the FBRM optics upon every cycle. The sums of these calculated surface particle counts were 79.1 and 82.7 per second for the smaller and larger peak, respectively. Upon noting the reported 75 Hz spinning speed of the FBRM optics yields a calculated rms of 1.0 and 1.3 for the Gaussian fit used in the determination, which are well within the bounds of the error calculated for the case where no surface particles were observed. Thus, the presence of two surface particles on the probe window was confirmed at the critical Ca^{2+} concentration level for the experiment using an initial concentration of 5 mg/L 10k-Na-PAA. Similarly, all of the CLDs being represented by critical concentrations plotted in Figures 3.9 and 3.10 were classified as either of the solution or surface type denoted by open or closed data points (i.e. □ or ■) respectively.

It is apparent from the consistency of both the PAA and Na-PAA plots that the trend for which nucleation type caused the number of FBRM counts/sec to surpass 200 not only depended on the molecular weights of the polymers added but also on their concentrations relative to their local maxima around 8 mg/L on their respective critical Ca^{2+} concentration versus polymer concentration curves. The relatively high MW polymers (M_w > 40,000) expressed a surface type of CLD at critical Ca^{2+} levels while the lower MW samples expressed the same type only at concentrations near or below their local maxima concentrations. Thus a distinction becomes evident in the mechanism responsible for inhibition by the addition of lower MW polymers. Once the concentration of added polymer surpasses the local maxima (at ~8 mg/L), the precipitated $CaCO_3$ crystals are no longer nucleating on nor adhering to the sapphire material of the probe window. It is hypothesized here that the reason for the absence of particles on the window is due to the increased ability of the lower MW polymers to effectively disperse the precipitated $CaCO_3$ particles in the solution phase. In this way, the added information regarding the location of the precipitated $CaCO_3$, as determined by the FBRM data, provides additional insight into the mechanism responsible for the local maxima occurring in the lower MW polymer performance curves. At concentrations less than ~8 mg/L, the lower MW polymers inhibited the nucleation and growth of $CaCO_3$ crystals, but had no effect on the final location of those crystals. Conversely, while still inhibiting precipitation at higher concentrations, the lower MW samples also effectively kept the

crystals dispersed in the solution. Although, this dispersive effect seems to come at the expense of overall inhibition as evidenced by the local maxima of the dosage-performance curves residing at the onset of complete particle dispersion.

As noted above, Loy *et al.* proposed the idea that an optimal MW exists for Na-PAA as an inhibitor of $CaCO_3$ precipitation and that the local maxima present in the performance curves is a result of the polydispersity of the samples,[44] but no insight onto the mechanism responsible for the difference was included. Here, an optimal MW range of ~7,000 would explain the differences seen in the performance curves as all samples exhibiting local maxima have a substantial mass fraction of 10,000 MW species or lower, as can be seen in the MWDs of Figure 3.6. Combining the results, it is concluded that although the lower MW polymer samples at low concentrations expressed a similar mechanism for inhibition, albeit more effective, as their higher molecular weight counterparts at all concentrations, the lower MW samples eventually lost their effectiveness once their concentrations surpassed 8 mg/L where overall crystal growth inhibition was sacrificed for dispersive traits.

In order to probe the differences between the mechanisms responsible for inhibition of the higher and lower MW polymer samples, images of the resulting $CaCO_3$ crystals at select formal concentrations of Ca^{2+} were taken via SEM. A set of crystallization experiments were again employed but instead of adding different MW samples to inhibit $CaCO_3$ precipitation, two samples, namely the 5k-PAA and 90k-PAA polymers, were mixed to various degrees and used at a constant total concentration of 10 mg/L. The mixtures allowed for a more controlled M_w and the imposed gradient from the lower MW to the higher MW sample allowed for comparison and investigation of the different mechanisms involved in inhibition for the two different MW regimes. The polymer mixtures ranged in quarterly mass fraction intervals from pure 5k-PAA (100:0 5k:90k PAA) to pure 90k-PAA (0:100 5k:90k PAA). The molecular weight distributions of the two pure samples (solid lines) are shown in Figure 3.14 along with the predicted MWDs of the 3 mixtures (dashed lines) and the M_w values (○) for each. The resulting FBRM chord length distributions were analyzed in the same fashion as the results above and the

critical calcium levels required to induce FBRM determined nucleation are shown in Figure 3.14 with respect to the secondary axis using weight average molecular weights of the mixtures as the abscissas. A similar trend to those reported in Figure 3.10 arose in terms of an optimal molecular weight range where critical calcium levels were the highest. Although, for these samples, the optimal M_w range was shifted towards higher MW samples and surrounded the 75:25 5k:90k PAA mixture (with an M_w of 41,900). This shift in the optimal molecular weight range most likely originated from the polydispersity of the mixed samples which were calculated to have PDIs of above 50 for the 50:50 mixture and around 40 for the 25:75 and 75:25 5k:90k mixtures. Samples of the crystals in the solution phase were collected on the half hour and imaged via SEM with 1, 2, and 2½ hour samples shown here. Figure 3.15 shows the typical crystals observed in solution, at a formal Ca^{2+} concentration of 1.68 mM, before the FBRM recorded nucleation. Even at calcium levels below the point at which particle nucleation and growth rapidly occurred, there were small $CaCO_3$ crystals present with distinct differences between those occurring in the presence of lower M_w PAA and those in the presence of higher M_w PAA.

Images A, B, and C of Figure 3.15 which represent the typical particles grown in the presence of the lower M_w PAA mixtures composed of 100%, 75%, and 50% 5k-PAA respectively, all express the characteristic peanut shape.[13] In stark contrast, images D and E represent the typical particles grown in the presence of the higher M_w PAA mixtures composed of 25% and 0% 5k-PAA respectively. These particles lacked a definitive overall shape but did exhibit many isolated planes of what appear to be the characteristic {100} cleavage planes of the rhombohedral calcite structure in any given particle. Although, the crystallographic directions of the isolated calcite faces were not aligned nor did they show any relative pattern within the particle. Upon further addition of calcium to the system, the particle morphology showed a change as rapid nucleation and growth persisted.

In Figure 3.16, the SEM images of the crystals found in the solution after 2 hours of Ca^{2+} addition (3.14 mM) are shown. Of the five variants of the 5k and 90k-PAA

mixtures, the systems employing 100%, 25%, and 0% 5k-PAA mixtures had reached their critical calcium levels at this point, implying that nucleation and growth were rapidly occurring. The particles formed in the presence of pure 5k-PAA, as shown in image A, no longer exhibited the peanut shape but rather a roughly spherical shape with many distinct {100} faces of calcite all configured with their $\langle \bar{1}\,11 \rangle$ directions intersecting the center of the crystal. This habit was not seen in the crystals formed in the presence of the 25% and 0% 5k-PAA mixtures where {100} faces remained observable but in the continued random orientation often times being offset by large areas of surface void of any resemblance to a flat cleavage plane as can be seen in images D and E. The two systems still below the critical calcium concentration at the 2 hour mark, namely the 75% and 50% 5k-PAA systems, are represented by their slowly forming crystals shown in images B and C, respectively. Here, a difference lies in the higher MW crystals with respect to the lower MW crystals. Where the crystals formed in the presence of the lower MW, 75% 5k-PAA, maintained the same general crystal habit as its 1 hour sample, the next higher MW system (50% 5k-PAA) now produced different crystals than its 1 hour sample. At 2 hours, the crystals grown in the presence of 50% 5k-PAA expressed rounded edges with multiple {100} faces being expressed. This was more analogous to the crystals produced by the 25% 5k-PAA at 1 hour than the 50% 5k-PAA precursor crystals. It should be noted here that in contrast to the relative arrangement of the expressed faces for the pure 5k-PAA case, the 50:50 case seemed to express larger {100} faces now loosely aligned as to remain parallel to the overall surface of the particle.

Since the 2-hour samples did not show the crystal habits of the solution particles after the FBRM recorded nucleation of the 75% and 50% 5k-PAA systems, Figure 3.17 shows the crystal habits of the $CaCO_3$ at 2½ hours (3.81 mM Ca^{2+}) for those polymer mixtures. For 25% 5k-PAA mixture, where inhibition of $CaCO_3$ precipitation was the strongest, the only change in crystal structure appeared to be the additional formation of larger, relatively spherical shaped particles as shown in image A. The size and shape of the already present peanut shaped particles remained the same as shown in image B. For the 50% 5k-PAA mixture system, the particles present at 2 hours seemed to grow slightly

with the addition of a few, much smaller, peanut shaped particles as shown in image C. Image D is a magnification of one of these smaller particles and suggest a limited growth since the ends of the peanut are not fully matured and the center stalk of the shape is still visible.

Summarizing the conclusions based on the SEM images, it is important to point out that the difference in the crystal habits of $CaCO_3$ formed in the presence of the lower MW PAA and those formed in the presence of the higher MW PAA can be summed up in a single aspect. The orientation of the expressed cleavage faces of calcite was observed to differ depending upon the M_w of the PAA inhibitor used. Keeping in mind that the 3-fold symmetry axis of rotation for the CO_3^{2-} anions of the calcite structure corresponds directly to the [111] direction of its unit cell, it is apparent that the different PAA MW regimes affect the orientation of not only the expressed faces, but consequently the orientation of the CO_3^{2-} ions as well. The effect of the lower MW PAA on the orientation of the calcite structure is to keep the 3-fold axis of the CO_3^{2-} anions normal to the center of the particle and therefore tangential to the overall (averaged) outside surface of the particle. This is expressed in the various peanut shapes and even more pronounced in the roughly spherical shape of the crystal shown in image A of Figure 3.16. As for the higher MW PAA, the orientation of the CO_3^{2-} anions of the calcite structure seemed to remain much less organized if at all. Thus, the observation here is that while lower MW PAA samples enforce a more organized crystal modification and the higher MW PAA samples prevent the expression of more calcite faces in general, the presence of both mechanisms (or a compromise between the two) results in the most efficient PAA inhibitor.

Conclusions

The molecular weight dependence of poly(acrylic acid) and its conjugate salt upon the inhibition of $CaCO_3$ was shown using more moderate experimental conditions than the kraft and Parr reactions of Chapter 2. A distinct difference in the inhibitory efficacy of polymers with substantial mass fractions of 10,000 MW or less ($M_w \leq 20{,}000$) and those of higher MW was shown in both the shape of their performance curves and the location

of the precipitated $CaCO_3$ once nucleation occurred. All of the lower MW polymers were shown to have local maxima in their performance curves around 8 mg/L while higher MW samples expressed a more linear relationship between critical Ca^{2+} concentration and polymer concentration with decreasing efficacy as MW increased. The efficacy of the lower MW samples at concentrations higher than the 8 mg/L local maxima was shown to be directly related to the location of $CaCO_3$ precipitation as all CLDs at critical Ca^{2+} levels expressed particles which remained dispersed in the solution phase.

It is clear that the molecular weights of the species involved in the inhibition of $CaCO_3$ are important, although a clear distinction between the various molecular weights is difficult to resolve as all polymer samples have high polydispersity indices and therefore are already composed of a broad range of MWs. In addition to this, the mechanisms which distinguish the performance of high MW samples from their lower molecular weight counterparts remain ill-defined as the FBRM method monitors only the $CaCO_3$ present as particles. In the work described in the upcoming chapters, monodispersed poly(acrylic acid) samples are prepared and implemented in order to overcome the ambiguity inherent in the highly dispersed polymer samples used thus far. These samples are also coupled with additional investigative techniques designed to monitor the behavior of the polymers alongside that of the calcium in the system in order to give a more comprehensive picture of how the molecular weight (and distribution) influence the performance of these polymeric antiscalants.

Tables

Table 3.1 The number and weight average molecular weights along with the polydispersity indices (PDIs) of the PAA and Na-PAA samples as measured via SEC.

Sample	**M_n (g/mol)**	**M_w (g/mol)**	**PDI**
2k-Na-PAA	600	1,680	2.80
5k-PAA	1,870	4,590	2.45
50k-PAA	15,600	107,500	6.89
90k-PAA	26,850	243,500	9.07
6k-Na-PAA	640	1,910	2.98
10k-Na-PAA	6,420	20,200	3.15
20k-Na-PAA	7,850	24,400	3.11
60k-Na-PAA	19,855	66,900	3.37
225k-Na-PAA	48,100	280,000	5.82

Figures

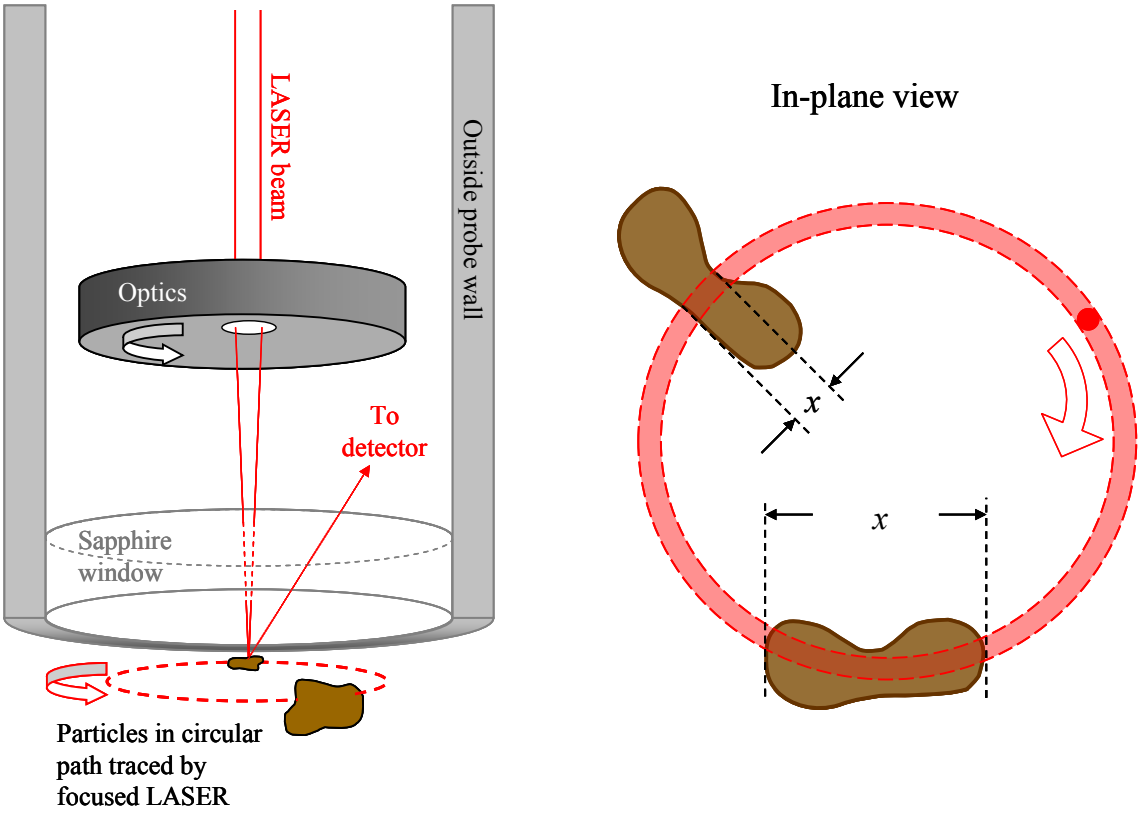

Figure 3.1 Schematic representation of FBRM probe (left) showing the spinning optics and path of the LASER beam used to measure the number and size of chord lengths of particles in solution. The in-plane view (right) shows the path of the focused LASER beam as it intersects the exact same sized particle at different points to measure different chord lengths, *x*. Not to scale.

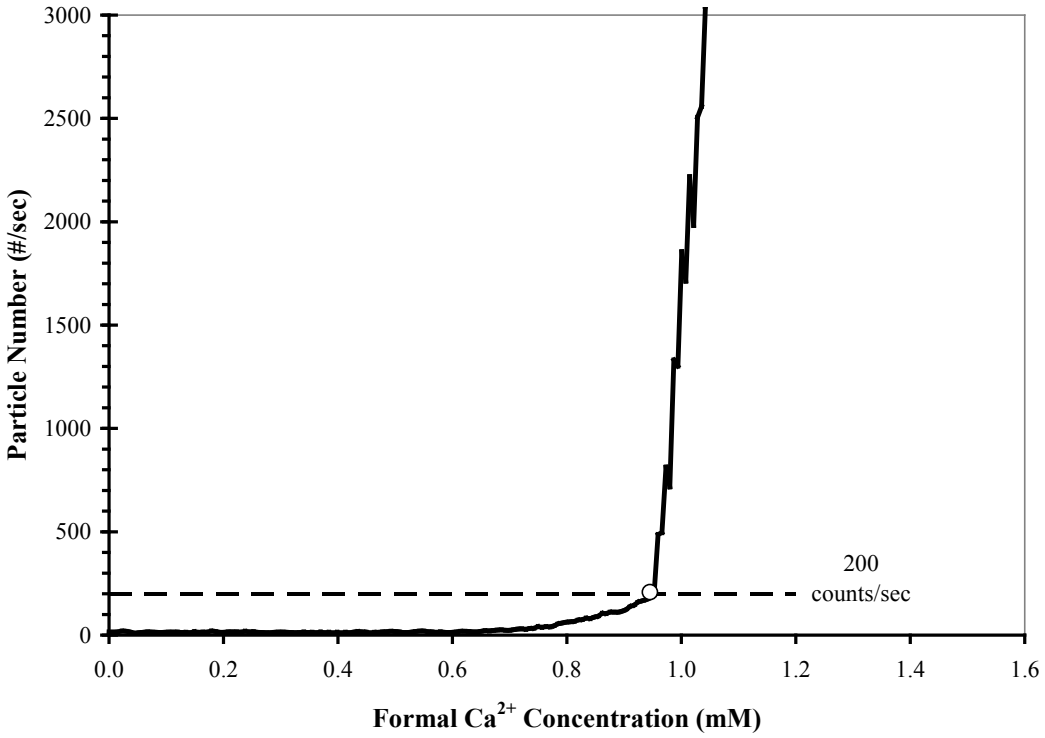

Figure 3.2 A typical plot of $CaCO_3$ particle count as monitored by FBRM with respect to the formal calcium concentration of the solution. 1000 mg/L Ca^{2+} solution was pumped at a rate of 0.6 mL/min into 500 mL of a 1 g/L Na_2CO_3 solution at pH 12 and 25 °C. The open circle (○) denotes the point at which the particle count reached 200 counts per second and hence where the critical calcium level was determined to be (dashed line).

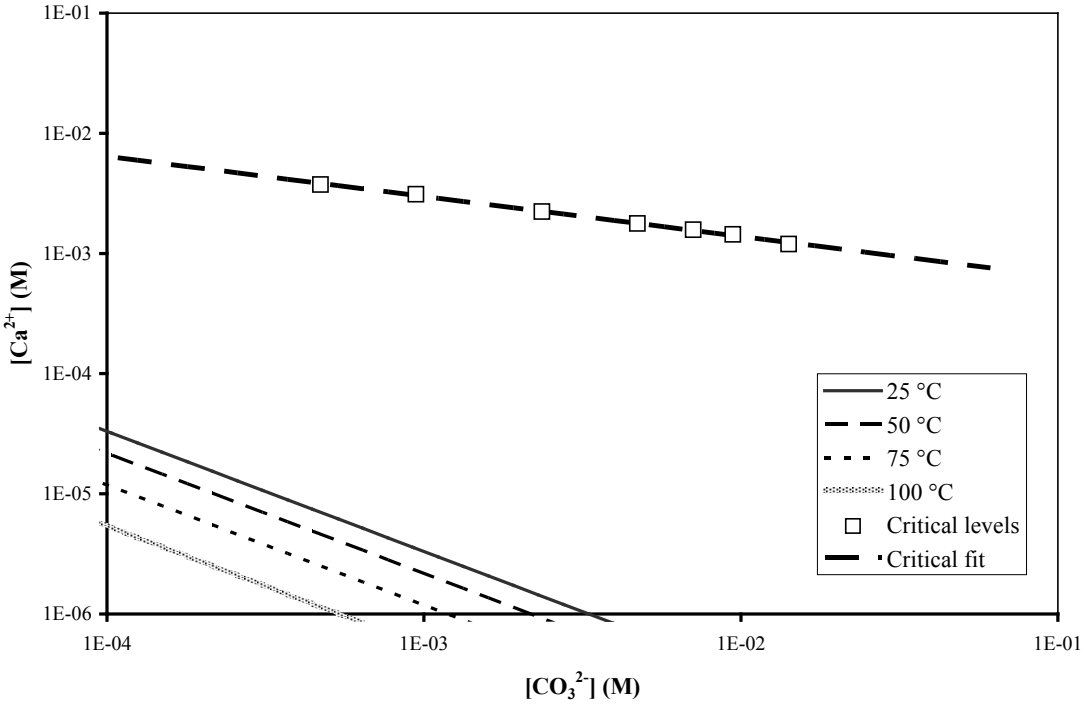

Figure 3.3 The solubility of $CaCO_3$ (calcite phase) at various temperatures along with the critical points where $CaCO_3$ precipitation occurs at 25 °C and pH of 12. The metastable region between the lines suggests the concentrations where a supersaturated solution is kinetically stabilized from precipitation.

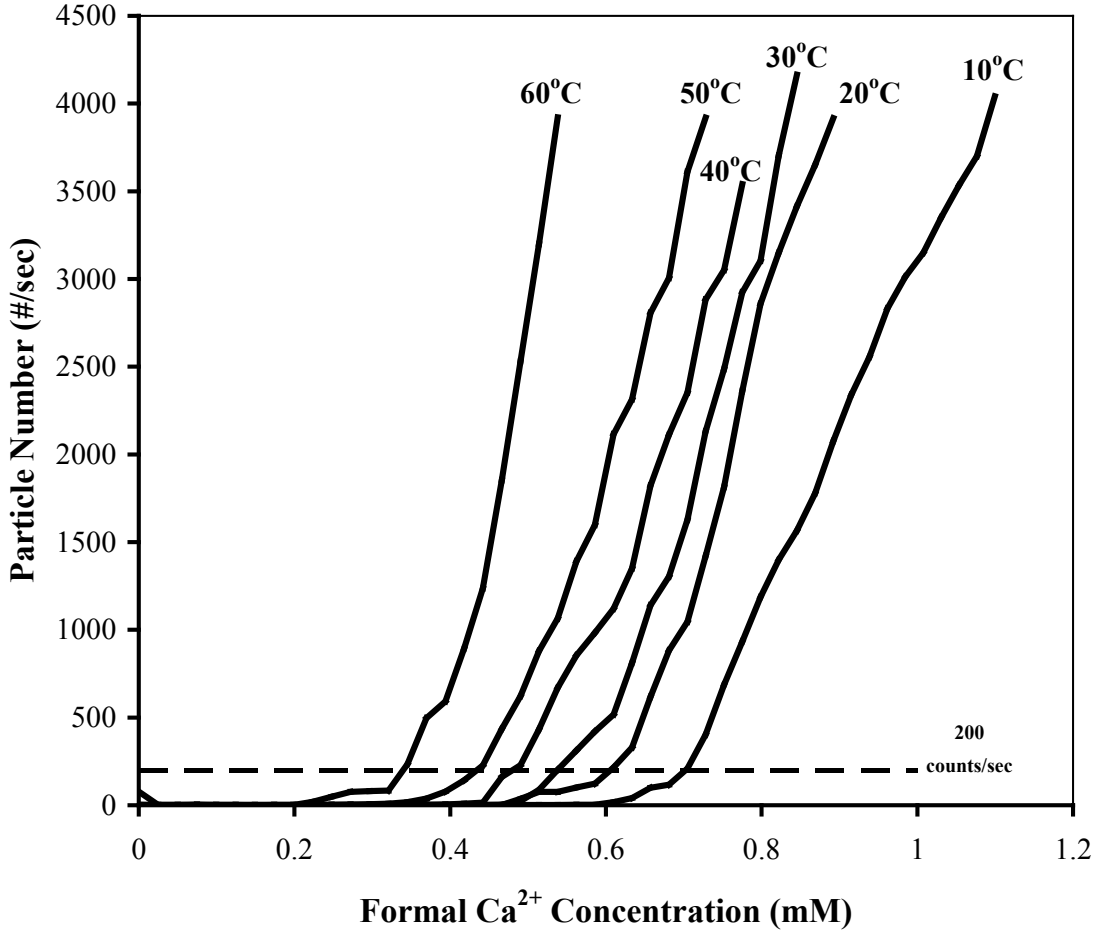

Figure 3.4 Total chord length counts via FBRM for $CaCO_3$ crystals at various temperatures as 25 mM Ca^{2+} solution was added to 500 mL of a 1 g/L (9.4 mM) $NaCO_3$, 1 g/L (25 mM) NaOH (pH ~12) solution at 0.6 mL/min. Nucleation concentrations (c_{nucl}) were taken once total chord lengths surpassed 200 per second.

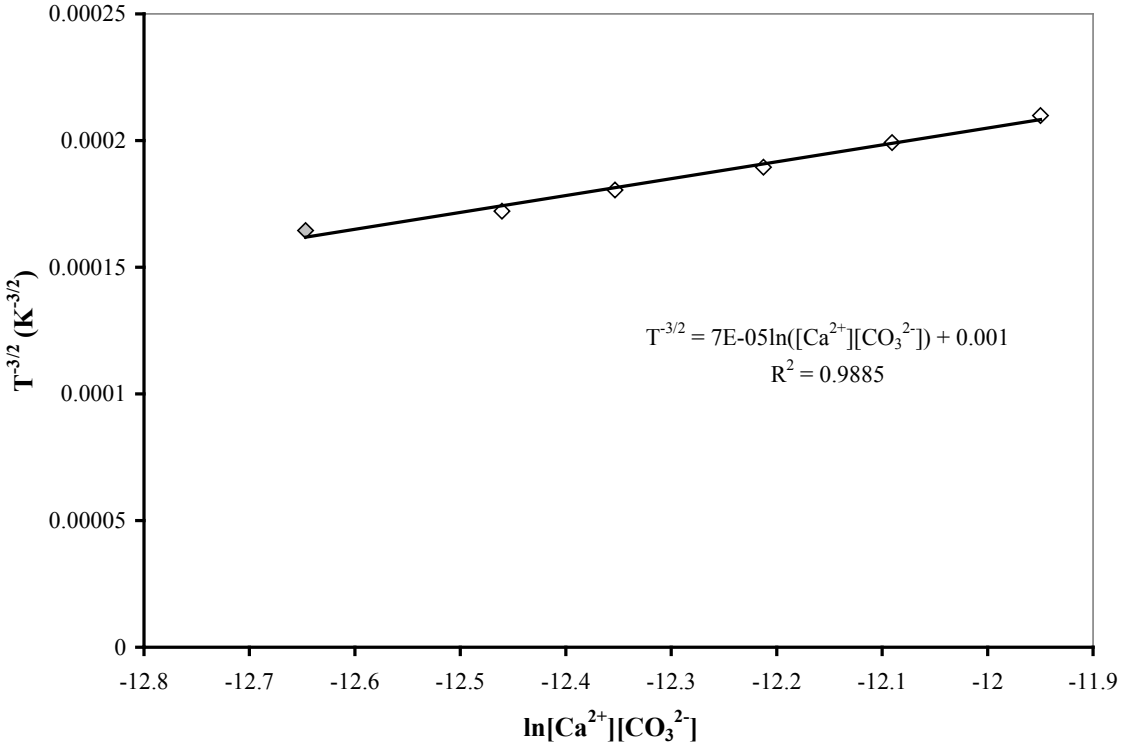

Figure 3.5 The linear dependence of $T^{-3/2}$ upon the natural logarithm of $[Ca^{2+}][CO_3^{2-}]$. Where T is the temperature at which $CaCO_3$ nucleation was monitored while $[Ca^{2+}]$ and $[CO_3^{2-}]$ are the calculated concentrations of calcium and carbonate at the point where 200 counts/sec were recorded via the FBRM (deemed the point of nucleation).

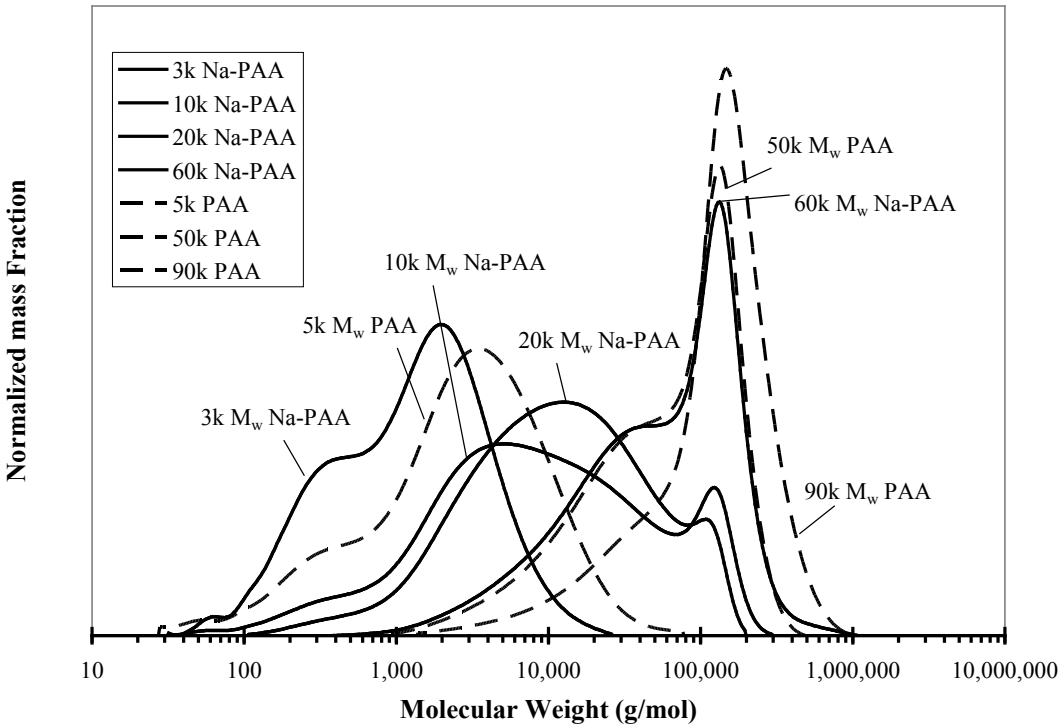

Figure 3.6 Molecular weight distributions as determined via SEC of commercially available poly(acrylic acid) (shown as dashed lines) and sodium polyacrylate (shown as solid lines) samples.

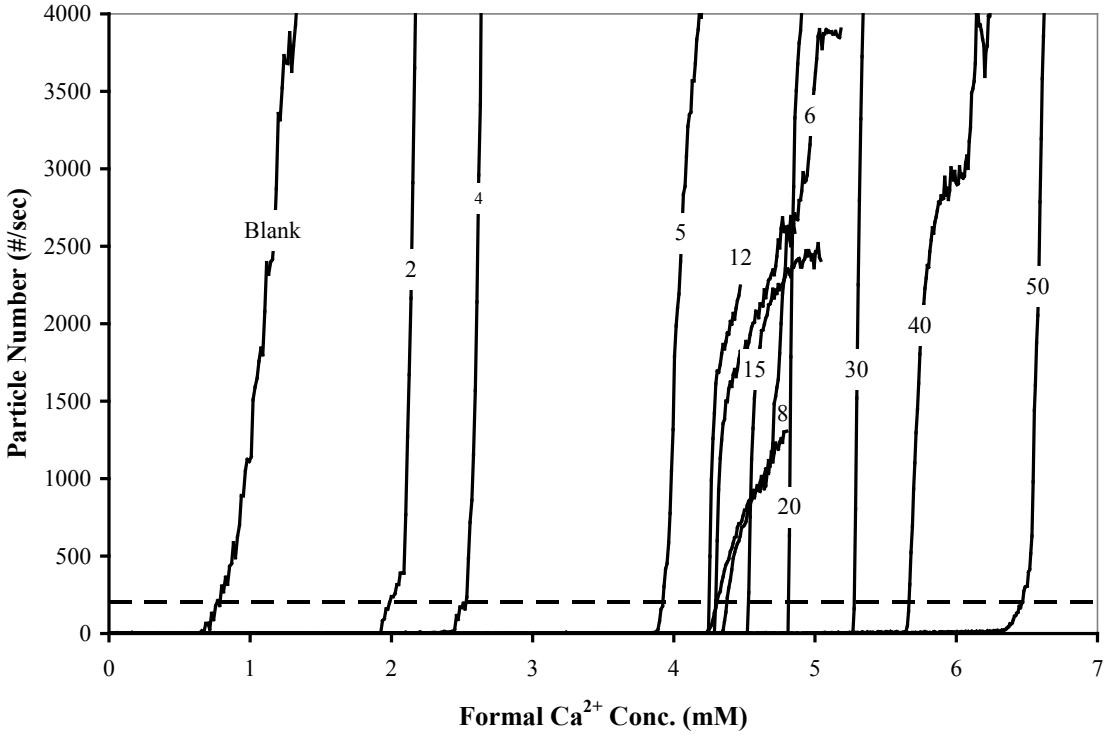

Figure 3.7 showing the curves produced by summing all chord length counts from FBRM for varying concentrations of 10k-Na-PAA. Note: Plots are labeled with their corresponding PAA concentration (in mg/L) and the dashed line represents the cutoff point (200 counts/sec) where nucleation data was taken.

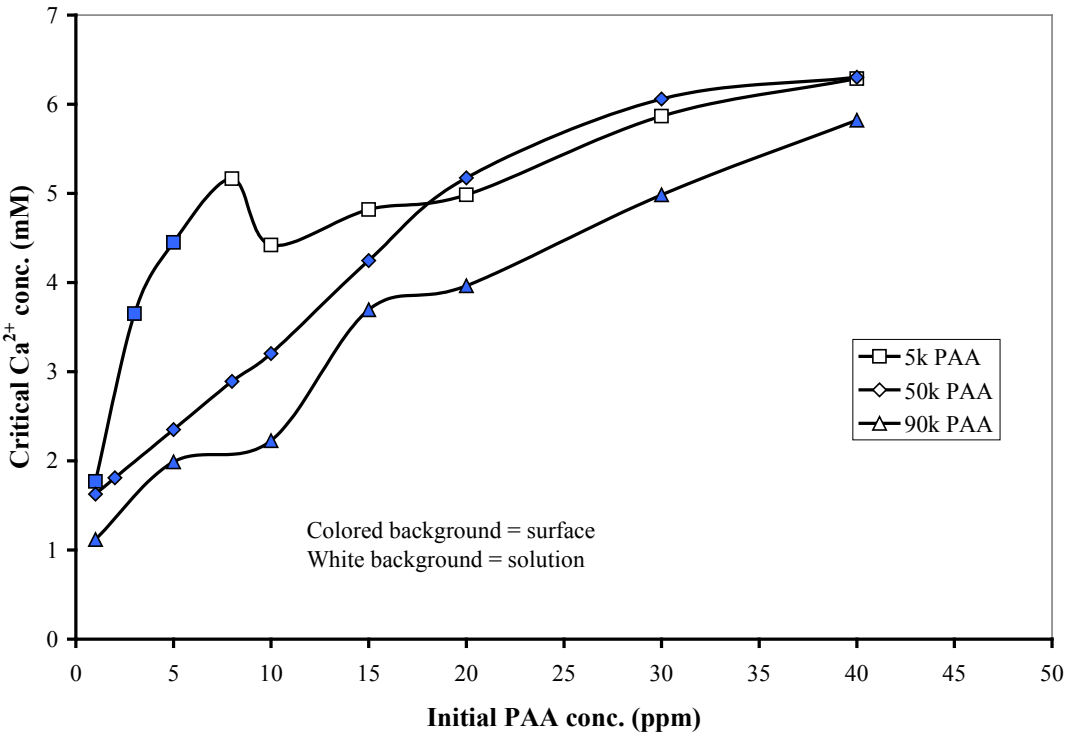

Figure 3.8 The critical calcium concentrations for various MW PAA samples with respect to their initial dosages as determined via FBRM total chord length counts. Open symbols (i.e. □ –white background) denote only particles within the solution were responsible for the particle counts surpassing 200 per second.

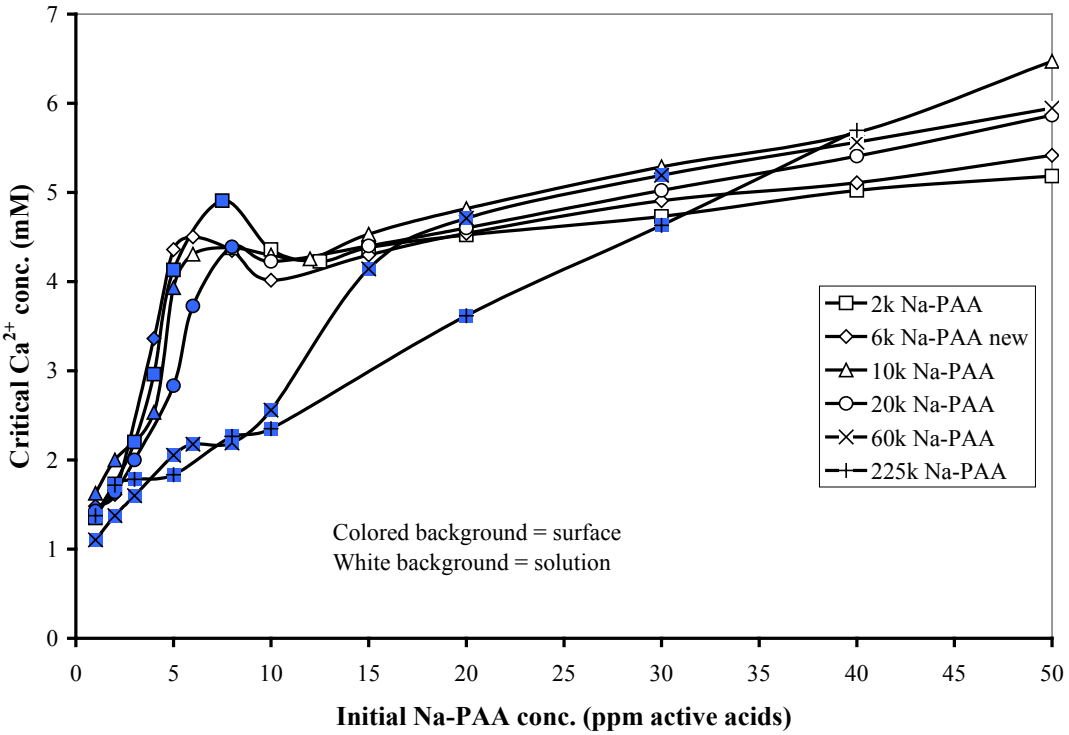

Figure 3.9 The critical calcium concentrations for various MW Na-PAA samples with respect to their initial dosages as determined via FBRM total chord length counts. Open symbols (i.e. □ –white background) denote only particles within the solution were responsible for the particle counts surpassing 200 per second.

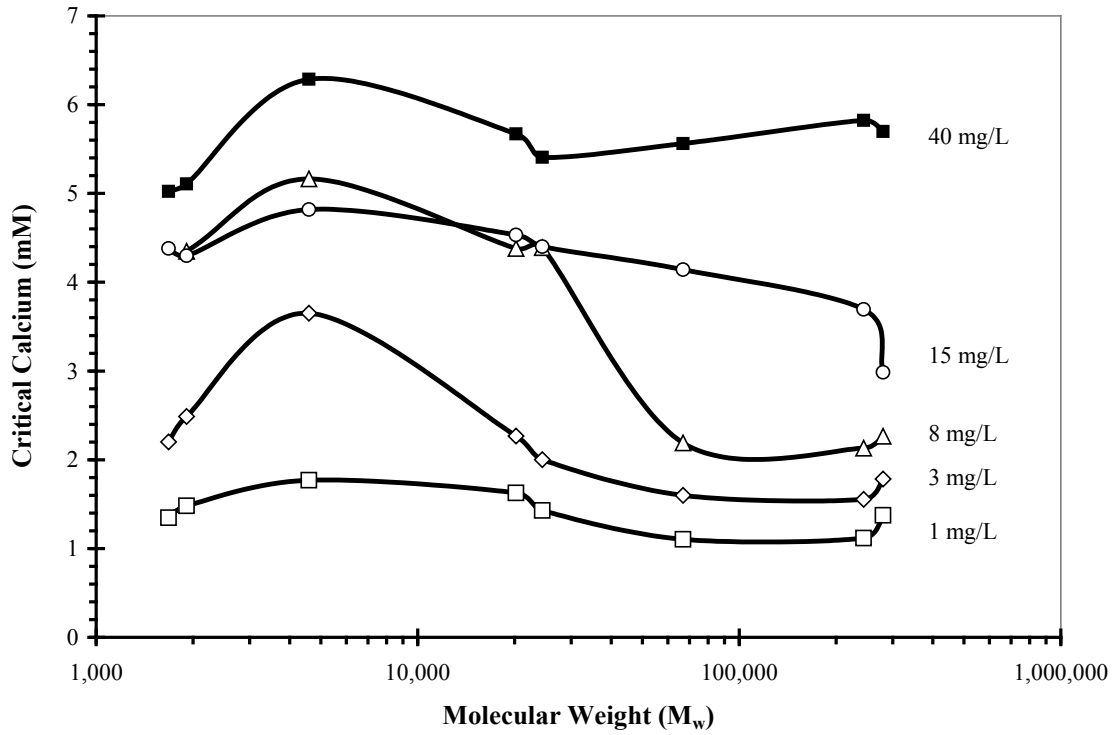

Figure 3.10 The molecular weight dependence of PAA and Na-PAA samples upon the critical calcium concentration for a system with initial Na_2CO_3 concentrations of 1 g/L and varying polymer concentrations from 1 to 40 mg/L as labeled on plot.

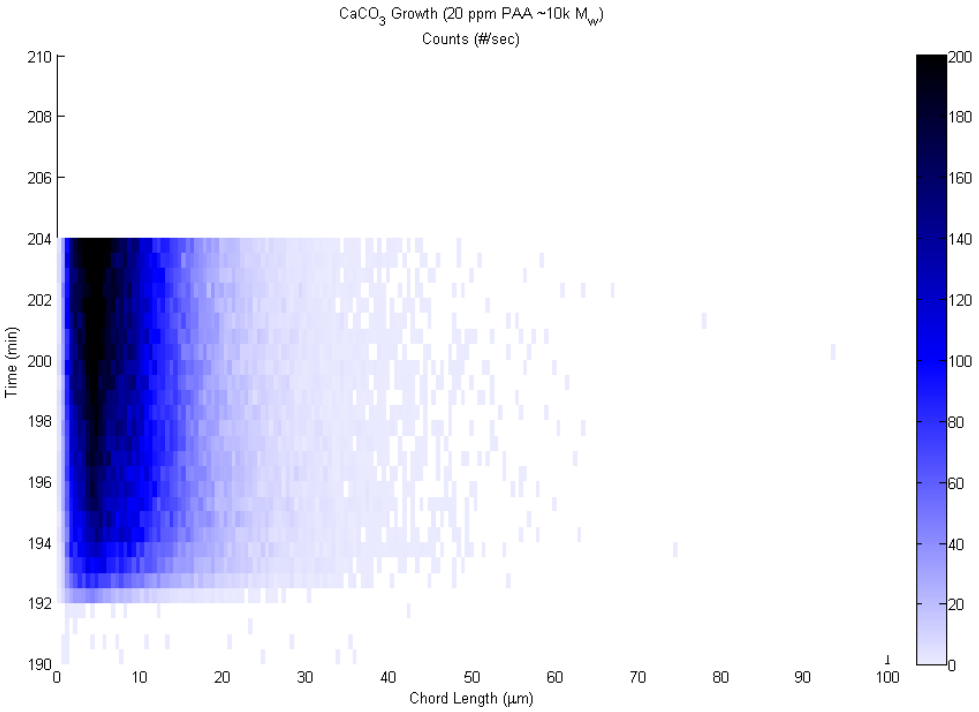

Figure 3.11 Crystal growth experiment employing 20 mg/L of 10k-Na-PAA showing FBRM chord length histograms as a 25 mM Ca^{2+} solution is added over time (0.6 mL/min). Darker pixels indicate higher chord length counts as expressed on the scale bar (right side). Note the smooth distribution produced by only particles within the solution (no growth on probe surface).

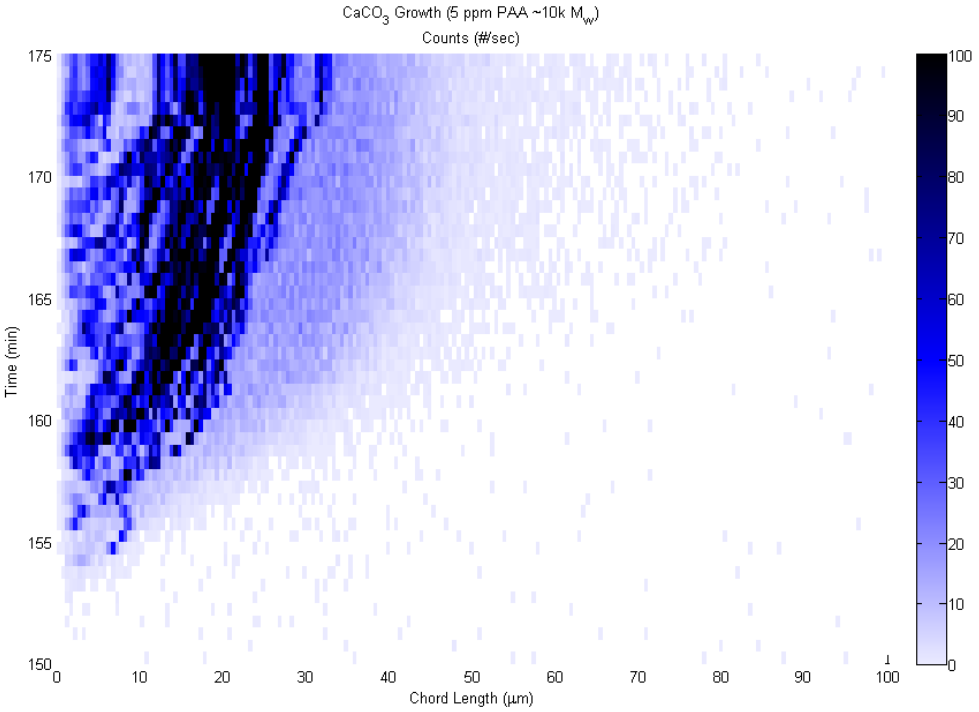

Figure 3.12 Crystal growth experiment employing 5 mg/L of 10k-Na-PAA showing chord length histograms over time. Note the surface nucleation on the window of the FBRM probe (visible as "vertical streaks") yielding counts correlating to its 75 Hz rotation speed.

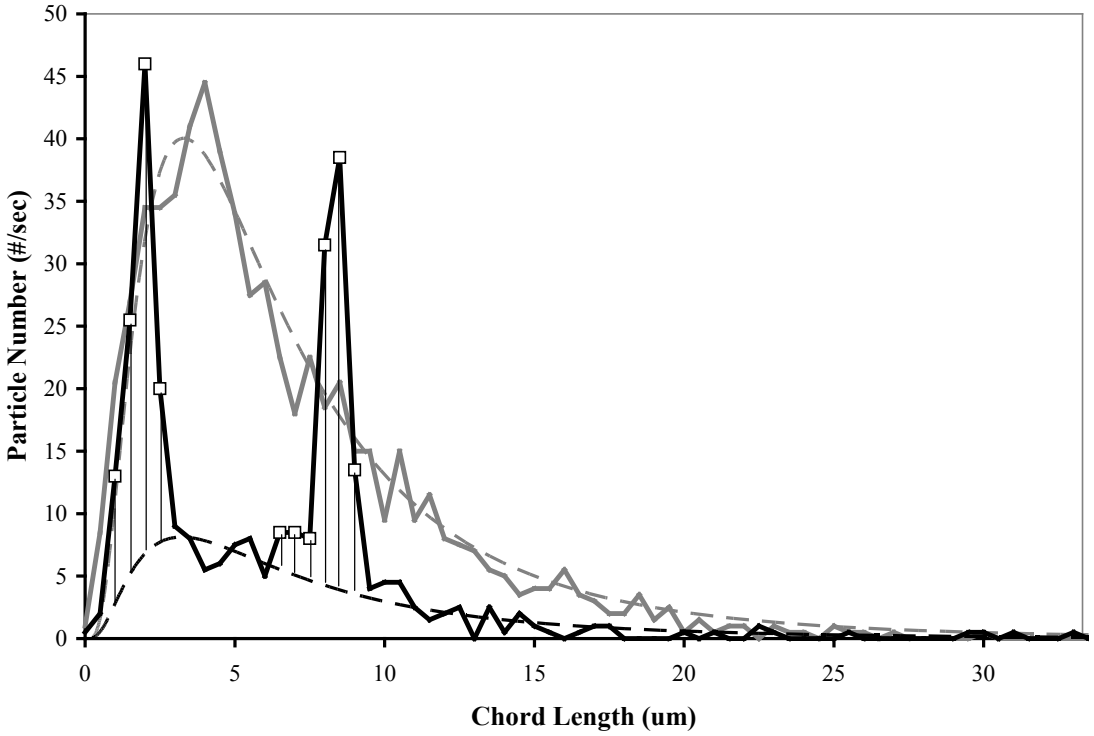

Figure 3.13 Chord length distributions at the critical points for initial 10k-Na-PAA concentrations of 5 mg/L (solid black line) and 20 mg/L (solid gray line). Log-normal Gaussian distribution fits for the underlying solution phase particles are shown as dotted lines. Chord length channels recording crystals on the surface of the probe window are shown as squares (□) with vertical line lengths representative of the additional chord length counts originating from surface particles.

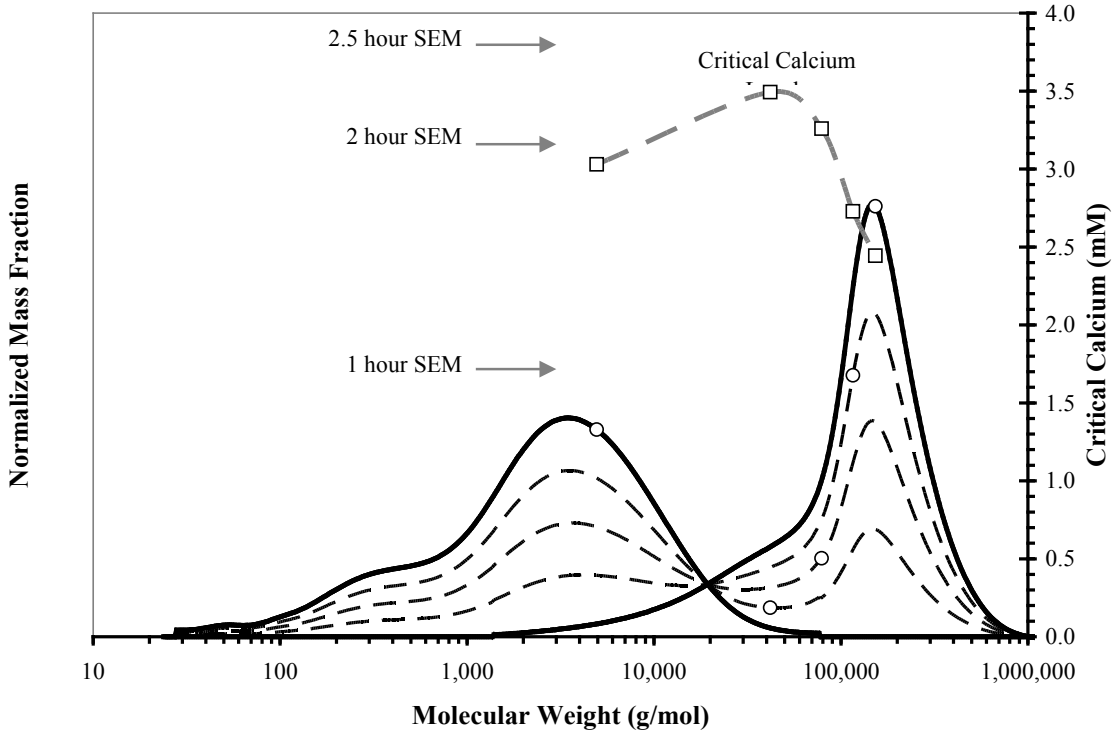

Figure 3.14 The MWDs of 5k-PAA and 90k-PAA samples (solid lines) and the calculated MWDs of their various mixtures at quarter mass fraction intervals (dashed lines) with weight average molecular weights shown as open circles (○). On the secondary ordinate, the critical calcium levels when implementing the various mixtures at a total initial concentration of 10 mg/L are plotted as open squares with dashed gray lines (– □ –) with respect to the weight average molecular weight of the mixtures. Arrows indicate the formal concentration of Ca^{2+} in the system at selected times representing SEM imaged samples.

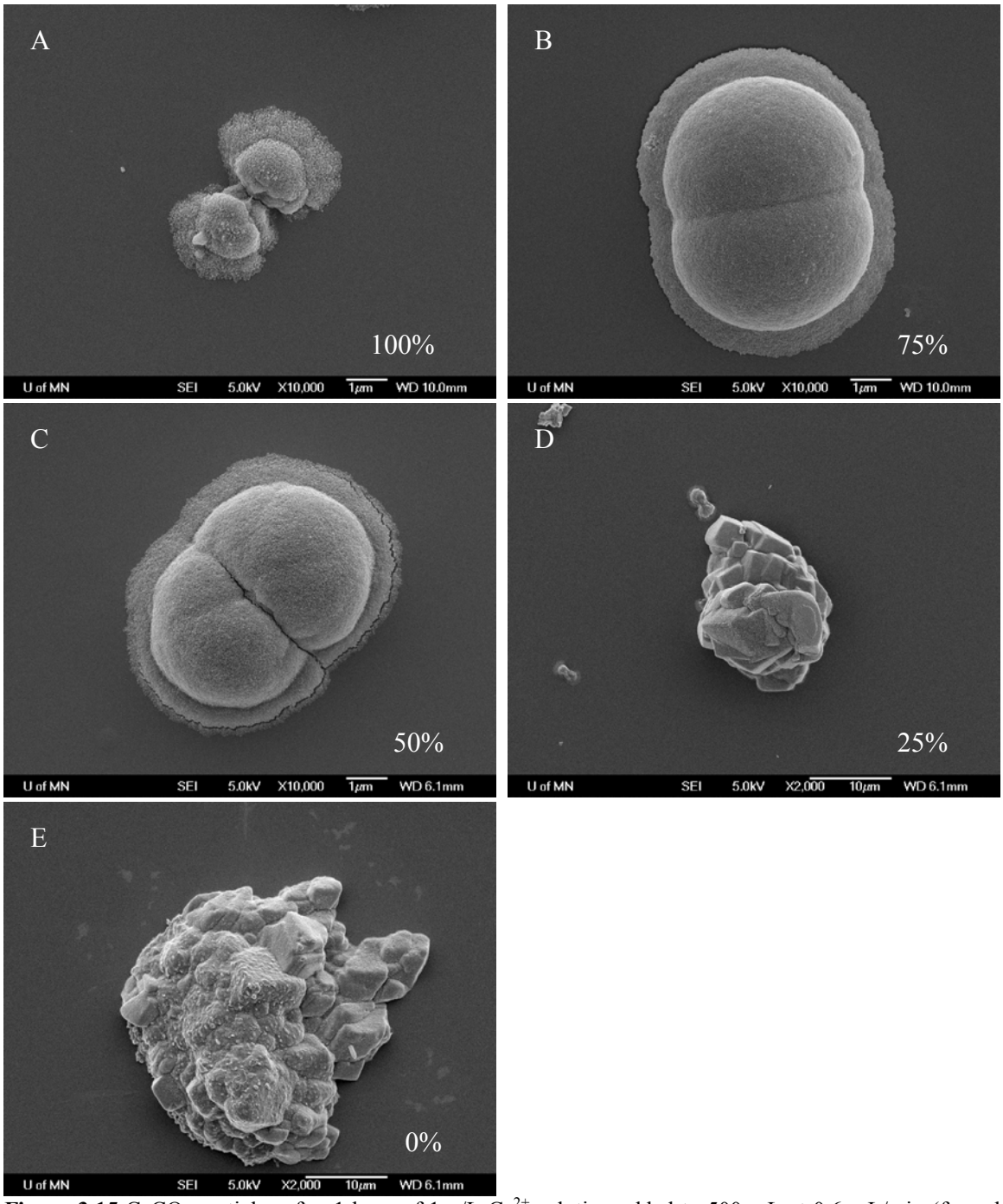

Figure 3.15 $CaCO_3$ particles after 1 hour of 1 g/L Ca^{2+} solution added to 500 mL at 0.6 mL/min (formal concentration of 1.68 mM Ca^{2+}) when precipitated from supersaturated solutions containing a range of 5k (shown as %) and 90k PAA mixtures as the inhibitor at a total initial concentration of 10 mg/L.

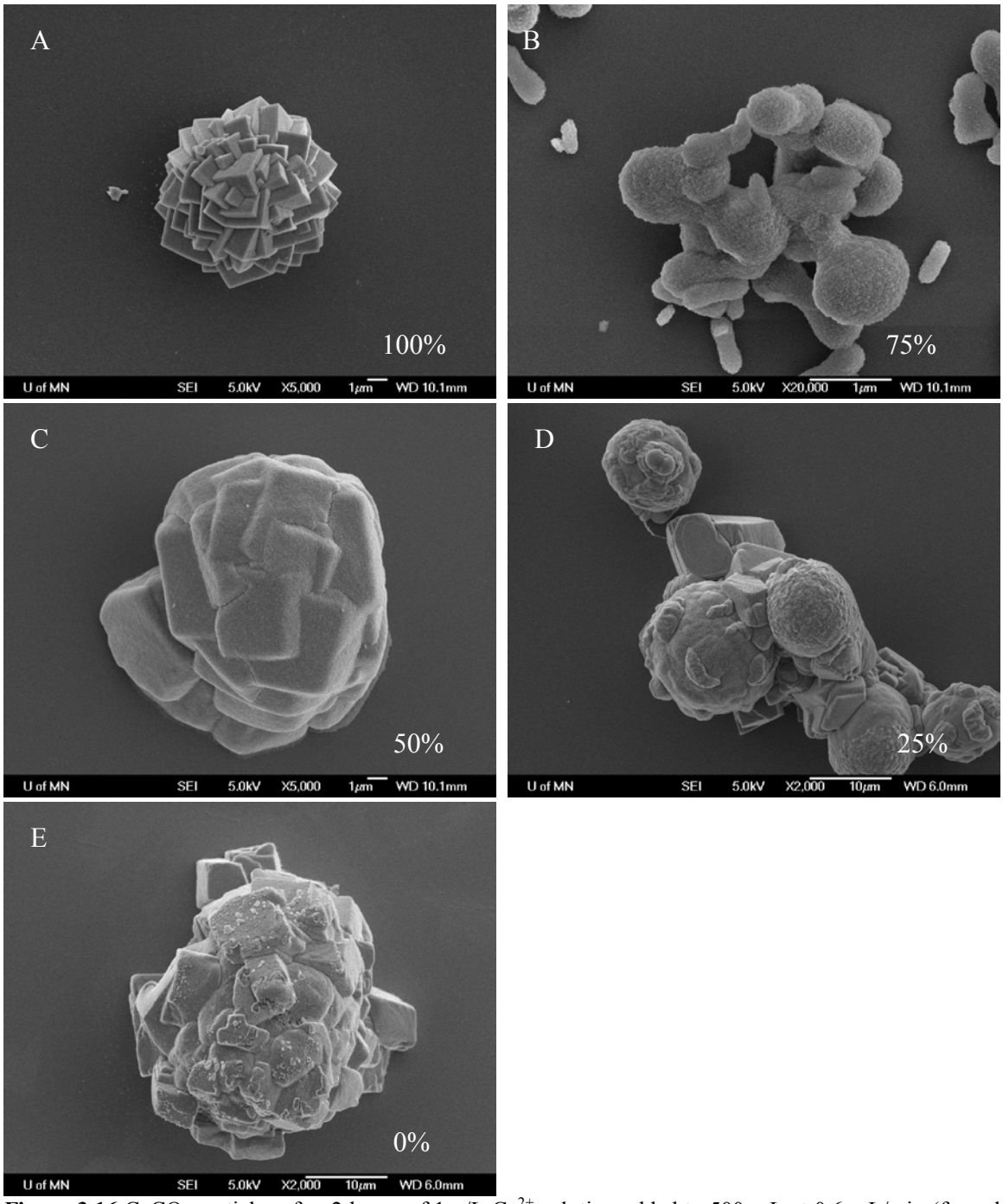

Figure 3.16 $CaCO_3$ particles after 2 hours of 1 g/L Ca^{2+} solution added to 500 mL at 0.6 mL/min (formal concentration of 3.14 mM Ca^{2+}) when precipitated from supersaturated solutions containing a range of 5k (shown as %) and 90k PAA mixtures as the inhibitor at a total initial concentration of 10 mg/L.

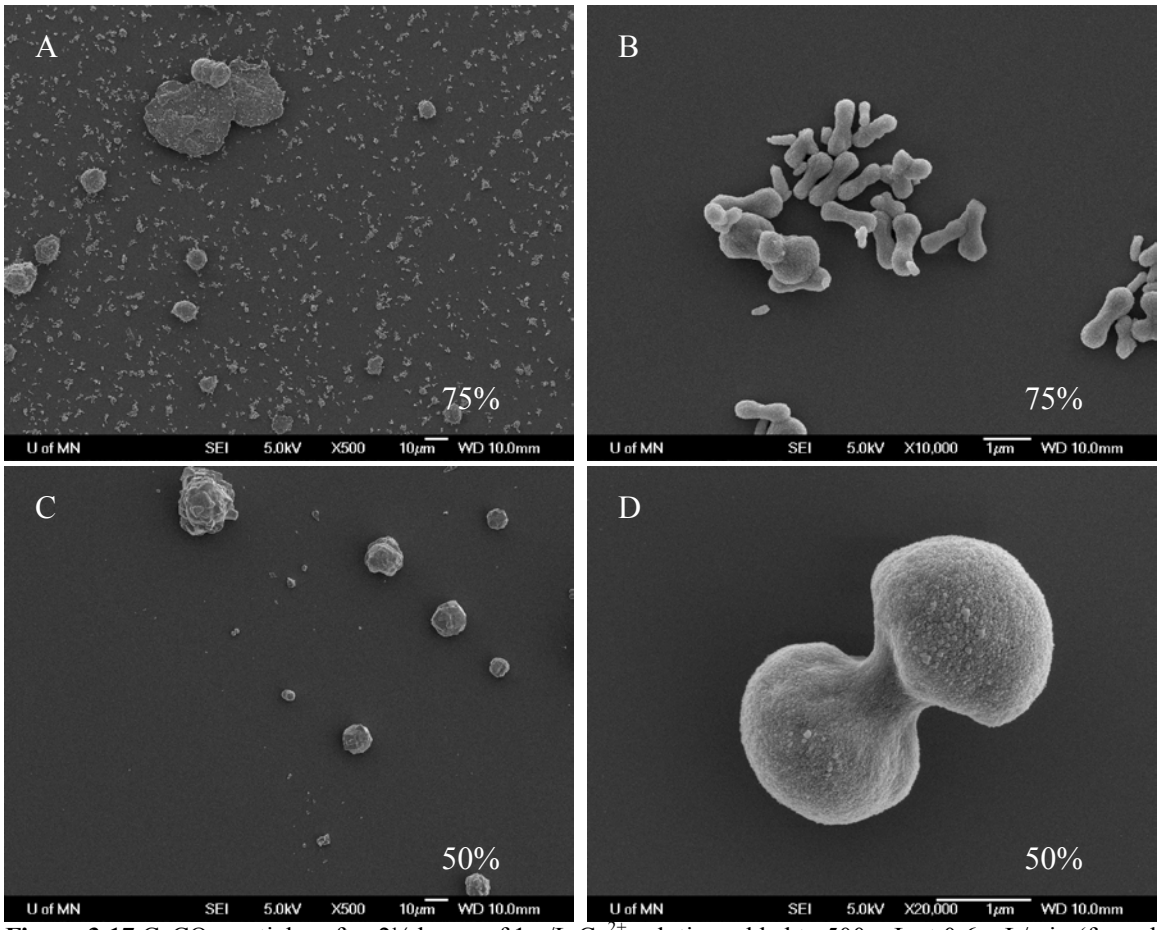

Figure 3.17 $CaCO_3$ particles after 2½ hours of 1 g/L Ca^{2+} solution added to 500 mL at 0.6 mL/min (formal concentration of 3.81 mM Ca^{2+}) when precipitated from supersaturated solutions containing a range of 75:25 (A and B) and 50:50 (C and D) 5k:90k PAA mixtures as the inhibitor at a total initial concentration of 10 mg/L.

Chapter 4 – Synthesis of Relatively Monodisperse PAA

Introduction

Commercial samples of poly(acrylic acid) (PAA) and its neutral salt, sodium polyacrylate (Na-PAA) are usually produced via free radical polymerization initiated by either potassium persulfate or ammonium persulfate. With a termination step by chain transfer, the ideal PDI of the resulting polymers is 2.0, any increase being a result of premature termination.[63, 64] The limited control over growth rates and sometimes even the mixing of multiple products to produce a product with a desired weight average molecular weight then produces a nominal polydispersity index (PDI) of the samples ranging from 3 to over 10. This relatively high and broad range of polydispersity was shown in Chapters 2 for a multitude of polymeric antiscalants used in the pulping industry for the inhibition of $CaCO_3$ scale and even for the commercially available PAA and Na-PAA samples in Chapter 3 intended for more generic purposes. The use of free radical polymerization as the dominating method for the synthesis of commercial polymer antiscalants is most likely due to its established efficiency and methods along with its lower cost with respect to newer polymerization methods. Although, it should be mentioned that newer "living polymerization" techniques are becoming more feasible as suggested by the use of living cationic polymerizations for the production of antiscalants intended to inhibit the formation of silica and silicate compound depositions present in the patent literature.[65, 66]

As discussed in the previous chapters, in order to effectively distinguish the effects of molecular weight on the $CaCO_3$ inhibition performance of poly(acrylic acid) a controlled set of polymer samples is necessary. Ideally, a single synthesis method allowing for the polymerization of monodispersed samples ranging over both the low (M_w < 20,000 g/mol) and high (M_w > 40,000 g/mol) molecular weight ranges found in Chapter 3 is sought after. Living polymerization techniques have been used extensively throughout the literature to produce nearly monodisperse polymer samples with PDI values sometimes below 1.05 but nominally around 1.1.[63, 67, 68] Atom transfer radical

polymerization (ATRP) was selected due to its ability to reach higher degrees and rates of polymerization than other radical polymerization techniques such as reversible addition fragmentation transfer (RAFT) while maintaining control over the polydispersity.[69, 70] In addition, ATRP is more forgiving than the ionic living polymerization techniques in terms of impurities and doesn't require the use of specialized initiators such as the RAFT polymerized PAA either. Another controlled radical polymerization technique, nitroxide-mediated polymerization, is unsuitable for PAA synthesis due to the tendency of its essential nitroxide compounds to decompose in the presence of acids such as acrylic acid.[71]

In a typical ATRP method, control over polydispersity is accomplished by controlling the rate of monomer addition and therefore reducing the number of side reactions. Initiators of similar chemical composition to the monomer residues are used with the exception of a halide substituent in the place of the next repeat unit. This halide plays the role of "capping" the reactive end of the growing polymer. Propagation occurs by "un-capping" the growing polymer end, reacting with a monomer, and "re-capping" the new end. A transition metal catalyst (i.e. Cu/ligand complex) is used to assist in the capping and un-capping of the growing polymer and ensure that the equilibrium distribution favors the capped state. This control over the distribution of capped and uncapped states gives ATRP the advantage of producing nearly monodispersed polymer samples from a robust chemical reaction method.

The single drawback of the ATRP method in this case is that although acrylic acid can be polymerized directly into PAA, the carboxylic acid groups tend to complex with the metal cations and therefore interfere with their catalytic effect. A common solution to this incorporates the use of *tert*-butyl acrylate, with its carboxylic acid group protected by the *tert*-butyl group (forming an ester group). The *tert*-butyl acrylate can then be safely polymerized into poly(*tert*-butyl acrylate) (PtBA) via ATRP as shown in Scheme 4.1 and subsequently hydrolyzed afterward to remove the *tert*-butyl protective groups as described in Scheme 4.2. This chapter outlines the synthesis of low PDI PAA samples via these two reactions.

Materials and Methods

Chemicals and Materials

Commercial sodium polyacrylate (Na-PAA) was purchased from Polysciences, Inc. (Warrington, PA) and SEC was used to confirm the broad molecular weight distribution. *Tert*-butyl acrylate (tBA), methyl 2-bromopropionate (MBP), N,N,N',N',N''-pentamethyldiethylenetriamine (PMDETA), CuBr, and $CuBr_2$, trifluoroacetic acid (TFA), along with all organic solvents (reagent grade) were purchased from Sigma Aldrich and used as received. All aqueous solutions were prepared using 18 MΩ "doubly" de-ionized water (DDI H_2O).

Equipment

A Varian (Palo Alto, CA) Unity 300 (with a Varian Inova console) was used to collect all ^1H NMR spectra as a summation of 50 scans. D_2O was used as a solvent for PAA samples, $CDCl_3$ for PtBA, and D_2O with a slight amount of sodium bicarbonate for any slightly water soluble copolymer of *tert*-butyl acrylate and acrylic acid. Size exclusion chromatography (SEC) was performed on an Agilent (Santa Clara, CA) 1200 Series HPLC with a UV-detector (λ = 215 nm) using Waters (Milford, MA) 250 & 120 Ultrahydrogel columns in series with a 0.3 M NaCl, 0.1 M NaH_2PO_4 eluent buffered solution (pH 7.0) pumped at 0.85 mL/min. A series of eight Na-PAA standards from Polymer Laboratories, Inc. (Amherst, MA) with molecular weights ranging from 1,250 to 323,000 g/mol were used to calibrate the system with all MWs being relative to these standards.

Experimental setup

Atom Transfer Radical Polymerization of PtBA

The monomer tBA, initiator MBP, ligand PMDETA, and catalysts CuBr/$CuBr_2$ were combined with proportions as outlined in Table 4.1 and stirred continuously. Cuprous bromide and cupric bromide were both measured into a clean dry round bottom flask containing a PTFE coated magnetic stir bar. The system was isolated with a septum after which the contained atmosphere was purged of O_2 by pumping N_2 through the system for

at least 15 minutes. Monomer was then added via syringe and needle which was purged with N_2 for at least another 5 minutes. The ligand was then added via syringe and needle, creating a blue solution, while N_2 was continuously bubbled through the system. The initiator was then added using the same technique as the ligand. Reaction contents were subsequently kept under a static positive nitrogen atmosphere and maintained at a fixed temperature of 60 ºC until polymerization was determined to be complete by either NMR analysis and/or viscosity (as determined visually). It should be noted that the polymerization temperature for the lower MW samples was kept at 45 ºC due to the relatively high concentration of initiator, and therefore radicals in the system. The reaction was terminated by quenching in cold water and diluting with aerated THF or acetone. Catalysts were removed from the polymerization reactants by passing through a short silica gel column using THF as the solvent. The diluted PtBA was then concentrated using rotary evaporation. The PtBA was further purified by precipitating the polymer with a drop-wise addition of a CH_3OH:H_2O (50:50) solution, collected, and re-dissolved in a small amount of THF. This purification step was performed three times and followed by subsequent evaporation of all remaining solvents by rotary evaporation and finally dried under vacuum (-110 mmHg relative to atmosphere) overnight leaving a transparent yellow solid. NMR samples were taken and used to confirm synthesis product and non-aqueous SEC was used solely to confirm low PDI values (~1.2).

Hydrolysis of PtBA to PAA

The PtBA was dissolved in dichloromethane (DCM) and hydrolyzed for at least 2 hours using trifluoroacetic acid (TFA) in a nominally 3:1 molar ratio of TFA:mer to produce PAA homopolymers with low polydispersities. Significant difficulties were encountered when the hydrolysis of PtBA via TFA was attempted due to the change in lyophibicity of the polymer chains as segments were hydrolyzed from *tert*-butyl acrylate to acrylic acid. Eventually, it was found that at least 3 separate hydrolysis reactions were required to fully complete the reaction. After each hydrolysis, the typically solid polymer contents were allowed to separate from the reaction solution phase, which was subsequently either decanted and/or removed via a glass transfer pipette. The polymer

was then washed thrice with diethyl ether and separated again. Upon the completion of the third ether washing, the sample was dried using rotary evaporation before drying under vacuum (-110 mmHg relative to atmosphere) over night to remove any remaining volatiles. Once the polymer sample was completely dry and before the next hydrolysis, it was crushed using a mortar and pestle until solid particles were nominally 0.5 mm in size or smaller. NMR samples were taken at this point to determine the relative completion of the hydrolysis before progressing to the next hydrolysis with both NMR and SEC samples being taken after the final hydrolysis. As final products to be used later; all polymer samples, with the exception of the highest molecular weight (105,000 M_w sample) were stored in their small solid particle form. The 105,000 M_w sample was dissolved in DDI H_2O and stored as an 8% (wt/wt) aqueous solution for further use.

Results & Discussion

The technique of preparing low PDI PAA samples via the hydrolyzation of ATRP PtBA outlined here has been documented in numerous publications as a method for selectively converting the PtBA segments of copolymers into PAA segments without disturbing other segments.[72-77] However, an extensive literature search resulted in no cases where PAA linear homopolymers were produced via this method.

Synthesis of low PDI ATRP Poly(*tert*-butyl acrylate)

A recipe for the ATRP of poly(*tert*-butyl acrylate) including a molar relationship of *x*:1:1:0.05:1.05 (tBA:MBP:CuBr:$CuBr_2$:PMDETA) where *x* was the desired degree of polymerization (modified from the literature)[78] was found to produce satisfactory results. The list of monomer to initiator ratios used is included in Table 4.1. SEC of the resulting PtBA yielded PDI values less than 1.2 (data not shown) which suggested the use of unpurified tBA monomer was sufficient and that the system was well controlled and lacking inhibitory impurities. NMR confirmed polymerization with the existence of a relatively large single peak at δ = 1.43 ppm representing the *tert*-butyl groups. Since this peak could be originating from either the tBA monomer or PtBA, comparison to the relatively low intensity of the characteristic quadruplet surrounded by two sets of doublet peaks of the tBA double bond at δ = 6.0 ppm was strong evidence that monomer

concentrations were minimal. Thus, leaving the only explanation for high concentrations of *tert*-butyl groups in the sample was from the successful production of PtBA. In terms of a complete analysis in $CDCl_3$ PtBA peaks were observed at δ = 1.15 (d, C**H**$_3$CH– initiation end group),1.27–1.69 (br, meso and racemo –C**H**$_2$– of the polymer backbone), 1.39–1.50 (br, (C**H**$_3$)$_3$C– *t*-butyl end group), 1.74–1.96 (br, meso –C**H**$_2$– of the polymer backbone), 2.08–2.51 (br, –C**H**– of the polymer backbone), 3.63 (s, C**H**$_3$O– initiation end group), 4.03–4.26 (m, –C**H**Br termination end) ppm.

Synthesis of low PDI PAA via the hydrolysis of PtBA

Since direct polymerization of acrylic acid via ATRP produces a polymer with many carboxylic acid functional groups capable of complexing the copper ions used during the propagation steps,[69, 79] the direct route was modified to incorporate a "capped" version of acrylic acid, namely tert-butyl acrylate, which does not interfere with the copper ions. In order to remove the *tert*-butyl "caps" and produce the desired PAA, the hydrolysis of the ester groups via TFA was employed.

Upon the first hydrolysis reaction of all PtBA samples, the polymer precipitated and for some of the higher molecular weight samples even managed to solidify enough to completely encapsulate the Teflon stir bar and stop its rotation. Since the NMR spectra still expressed a substantial amount of *tert*-butyl groups present in the sample, a number of alternative hydrolysis methods were explored. Due to the precipitation of the polymer the resulting reaction rate of the hydrolysis decreased as the TFA was required to diffuse through the solid polymer in order to react. The drastic difference in the lyophilicity of the PtBA reactant mers and the product PAA mers presented a challenge in terms of finding a solvent capable of dissolving the polymer chains both before and after hydrolysis. Both alkaline and acidic hydrolysis methods were explored using a wide range of solvents and aqueous solution gradients but the outcome remained the same; either the reactant PtBA did not dissolve or the product PAA precipitated. Even the alkaline hydrolysis method Kawabe and Yanagita used for the hydrolysis of poly(methyl acrylate) using a static acetone/H_2O mixture as the solvent[80] remained unsuccessful even as it was adopted and modified by the slow addition of H_2O in an attempt to match the

hydrophobicity of the solvent to that of the reacting PtBA-*co*-PAA copolymer in all its stages from PtBA to PAA. Eventually, for the sake of simplicity, the hydrolysis method using TFA in DCM was used for the preparation of PAA. It should be noted that most of the literature employing the hydrolysis of PtBA copolymers via TFA/DCM, as noted above, allow for a single hydrolysis reaction due to the solubility of the non-tBA segments of the reactant polymer in the DCM solvent. For the rare case where the non-tBA segments was hydrophilic, precipitation of the product PAA copolymer in the DCM/TFA solution ensued, but the hydrolysis reaction was still found to be satisfactorily complete for this lower MW via NMR.[81] Since the incomplete hydrolysis of all *tert*-butyl groups of the PtBA (even 0.5% unhydrolyzed) has been raised as an issue previously,[69] a number of steps were taken to ensure complete hydrolysis.

Firstly, successive hydrations using fresh TFA/DCM with at least three ether washes in between the separate hydration reactions was employed. Since the TFA hydrolysis is an acidic hydrolysis reaction of the ester group, it is technically reversible and the removal of products along with the maintenance of high levels of reactants was essential to continue the progress of the hydrolysis towards the reactants side of the mechanism as shown in Scheme 4.2. The compliment of this, namely the insurance of high concentrations of the reactants, was also directed via the use of a high molar ratio between the TFA and polymer mers present. Nominally, a ratio of 3:1 TFA:mer was employed and even a ratio of up to 5:1 was used for some of the higher MW samples during their last hydrolysis reactions.

Shown in Figure 4.1 are the NMR spectra of a high molecular weight sample (~500 DP) throughout the second hydrolysis after an initial "preparation" hydrolysis of only 60 minutes allowing for all subsequent NMR samples to be soluble in D_2O (with the aid of some sodium bicarbonate). The sample was not washed with ether between hydrolysis reactions to accentuate the accumulation of products not removed by simple separation of the solids from the liquid phase. Samples were taken every 15 minutes and solids were quickly separated from the reaction liquid and dried under vacuum to remove any remaining TFA and DCM before NMR and SEC samples were made. As can be seen in

the substantial decrease in the *tert*-butyl peak at δ = 1.42 ppm, relative to the broad backbone peak ranging from δ = 1.2–1.75 ppm as hydrolysis time increased, the reaction continued despite the accumulation of products and the solid nature of the reactant polymer although it should be mentioned that after 1 hour the *tert*-butyl peak remained constant (spectra not shown). Oddly enough the *tert*-butanol peak at δ = 1.18 ppm remained relatively constant throughout the reaction suggesting that the additional hydrolysis of the *tert*-butyl trifluoroacetate product via H_2O, as shown in the dashed circle of Scheme 4.2, was not stoichiometrically linked to the polymer hydrolysis reaction but rather a by product of the existence of a static amount of moisture in the reaction vessel and therefore not useful in determining the polymer reaction progress. Two alternative methods were used to quantify the progress of the hydrolysis with the results shown in Figure 4.2. The first method, plotted on the primary ordinate in closed diamonds (♦), was derived from the NMR data shown in Figure 4.1. Noting the number of protons associated with **C**, **D**, **E**, and **H** from the chemical structure above the spectra in Figure 4.1, the conversions of PtBA to PAA for each sampled hydrolysis time were calculated using the areas under their respective peaks using:

$$\text{Conversion } \% = 1 - \frac{(C+H) - 2(D+E)}{9(D+E)} \times 100\% \qquad (1)$$

Due to the *tert*-butanol peaks, the integration over the **C**+**H** range is most likely an underestimate as the peaks from the **C** protons at the lower δ shifts are still present under the *tert*-butanol peaks. With the integration end point being forced to stop at the valley around δ = 1.23 ppm, the underestimation of **C**+**H** results in calculated conversion percentages being slightly higher than their presumed reality.

In addition, the M_n values of the MWDs as determined via SEC are plotted against the secondary ordinate axis of Figure 4.2 in open squares (□). Here, the SEC measurement of conversion is suspected to deviate from the real values in the opposite direction due to the fact that SEC does not directly measure molecular weights but rather the hydrodynamic volume of the random coils in the buffered eluent. Thus, the M_n values

become more accurate as the polymer samples near complete conversion to PAA. Although the true molecular weight of the polymer chains is decreasing with the removal of *tert*-butyl groups, the polymer is also becoming more soluble in aqueous solution and would be expected to swell to a relatively larger extent than the less hydrolyzed polymers having more of the hydrophobic *tert*-butyl groups. With all these things considered, it was determined that complete hydrolysis could be reached with subsequent hydrolysis reactions using fresh TFA solutions and previous products (*tert*-butyl trifluoroacetate and *tert*-butanol) being removed between steps as an essential prerequisite.

The final step taken to ensure complete hydrolysis of the *tert*-butyl acrylate mers was the grinding of the polymer sample into small particles with diameters nominally lower than 0.5 mm in between hydrolysis reactions. This decrease in solid polymer particle size helped decrease the burden of diffusion responsible for bringing the TFA and *tert*-butyl acrylate monomer residues together.

Shown in Figure 4.3 are the NMR spectra following the progress of ~500 DP PtBA as it was converted into PAA with undetectable amounts of residual *tert*-butyl groups remaining un-hydrolyzed after the third hydrolysis. After the final hydrolysis and ether washing, the PAA product expressed an NMR spectrum exhibiting only the characteristic peaks from the PAA backbone at δ = 1.5–2.0 ppm (br, meso and racemo –C**H**$_2$–) and 2.3–2.5 ppm (br, meso –C**H**$_2$–) and with barely detectable peaks from the initiator end group at δ = 1.1 ppm (d, C**H**$_3$CH–) and 3.63 (s, C**H**$_3$O–) in D_2O. One interesting feature is the significant shift in the broad polymer backbone peaks with increasing hydrolysis of the PtBA-co-PAA to PAA homopolymer. This was slightly noticeable in the spectra from the timed hydrolysis experiment shown in Figure 4.1 and is most likely due to the increasing solubility that accompanied the conversion of *tert*-butyl acrylate esters to carboxylic acid functional groups. As the polymer increased in solubility (of the NMR solvent D_2O) the increased interaction between its carboxylate groups and the water decreased the electron shielding of the backbone protons.

The number average degree of polymerization of all the PAA samples produced, with a sampling of NMR spectra shown in Figure 4.4, were calculated by integrating over all

the backbone peaks and initiator methyl acrylate peaks of the NMR spectra and taking the ratio of their areas. This degree of polymerization was then converted into the NMR determined M_n by simply multiplying by the molar mass of the acrylic acid mer, 72 g/mol. As expected, in the high molecular weight cases (above 200 degrees of polymerization), the signal to noise ratio as the number of polymer end group protons paled in the light of the number or backbone protons significantly decreased the accuracy of the relative area under the initiator end group peaks leaving their subsequent M_n values subject to increasing error. No discernable initiator end group peaks above the noise of the NMR spectrum baseline could even be found for the highest molecular weight sample. The SEC determined MWDs of the final PAA products are shown in Figure 4.5 with their calculated M_n, M_w, and PDIs tabulated in Table 4.2 along with their NMR determined M_n values. The molecular weight distributions were symmetrical for all but the highest of molecular weights with no tails or shoulders which would represent premature termination or significant impurities during the polymerization. The congruence between the M_n values as determined between the 2 different measurement techniques was representative of a well controlled ATRP synthesis of the PtBA followed by complete hydrolysis into PAA.

Conclusions

As outlined in Chapters 2 and 3, a need for a monodispse sample set of PAA existed. Here, the living polymerization technique, ATRP, was used to synthesize poly(*tert*-butyl acrylate) which was hydrolyzed with sequential hydrolysis reactions using TFA and DCM to produce PAA homopolymers. The hydrolysis was shown to be complete via NMR and the poly dispersity indices of the PAA chain within each polymer sample were shown to be less than or equal to 1.3 for the majority of MW samples and relatively low (1.6 and 2.7) for the two highest MW samples. Thus a sample set composed of relatively monodispersed poly(acrylic acid) was synthesized covering a range of M_w values from less than 3,000 to more than 100,000 g/mol. These samples will be used in the upcoming chapters to further elucidate the effects of molecular weight of the PAA antiscalants upon

$CaCO_3$ nucleation and growth rates at high pH conditions conducive to kraft pulping conditions.

Tables

Table 4.1 List of ingredients for the various degrees of polymerization (DP) of PtBA samples synthesized via ATRP. Molar ratios were calculated using *x*:1:1:0.05:1.05 (tBA:MBP:CuBr:$CuBr_2$:PMDETA) with *x* representing the degree of polymerization (DP).

DP	tBA (g)	MBP (mL)	CuBr (g)	$CuBr_2$ (mg)	PMDETA (mL)
30	100	2.6	3.36	130	5.0
50	100	1.6	2.01	78	3.0
75	100	1.0	1.34	52	2.0
100	100	0.78	1.01	39	1.5
125	100	0.63	0.806	31	1.2
200	100	0.39	0.504	20	0.75
500	100	0.16	0.201	7.8	0.30
1000	100	0.08	0.101	3.9	0.15

Table 4.2 Synthesized PAA samples via the hydrolysis of ATRP PtBA with TFA/DCM with molecular weight averages characterized via NMR and SEC.

Label	M_n (NMR)	M_n (SEC)	M_w (SEC)	PDI (SEC)
30 DP	3,113	2,090	2,711	1.3
50 DP	3,691	2,564	3,353	1.3
75 DP	5,385	4,937	5,772	1.2
100 DP	8,402	8,663	10,020	1.2
125 DP	9,792	13,636	16,902	1.2
200 DP	18,965	27,733	35,142	1.3
500 DP	46,203	47,176	74,924	1.6
1000 DP	NA	38,250	104,875	2.7

Schemes

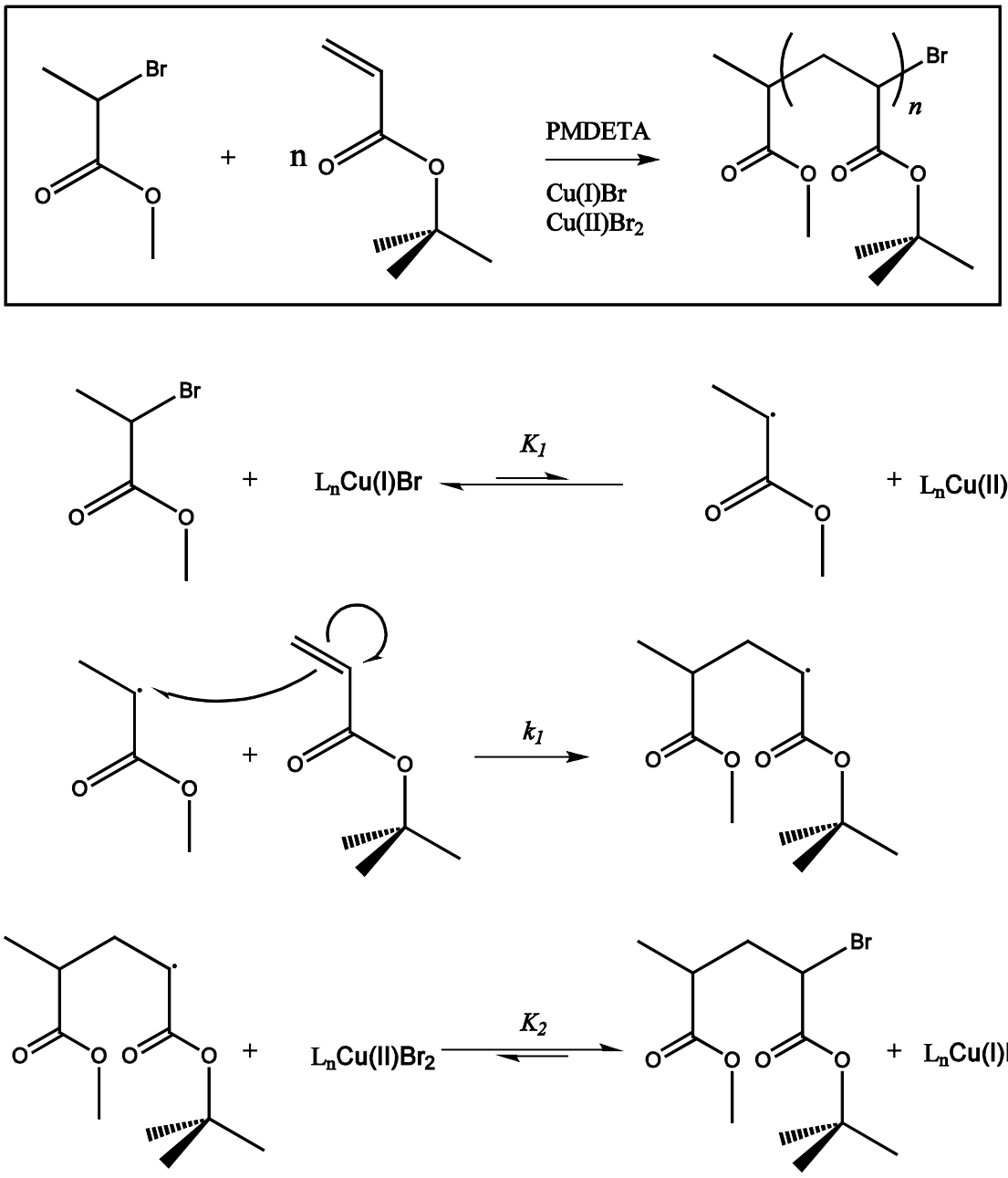

Scheme 4.1 The Atom Transfer Radical Polymerization (ATRP) of poly(*tert*-butyl acrylate). The overall scheme is shown in the upper box while the detailed mechanism follows below.

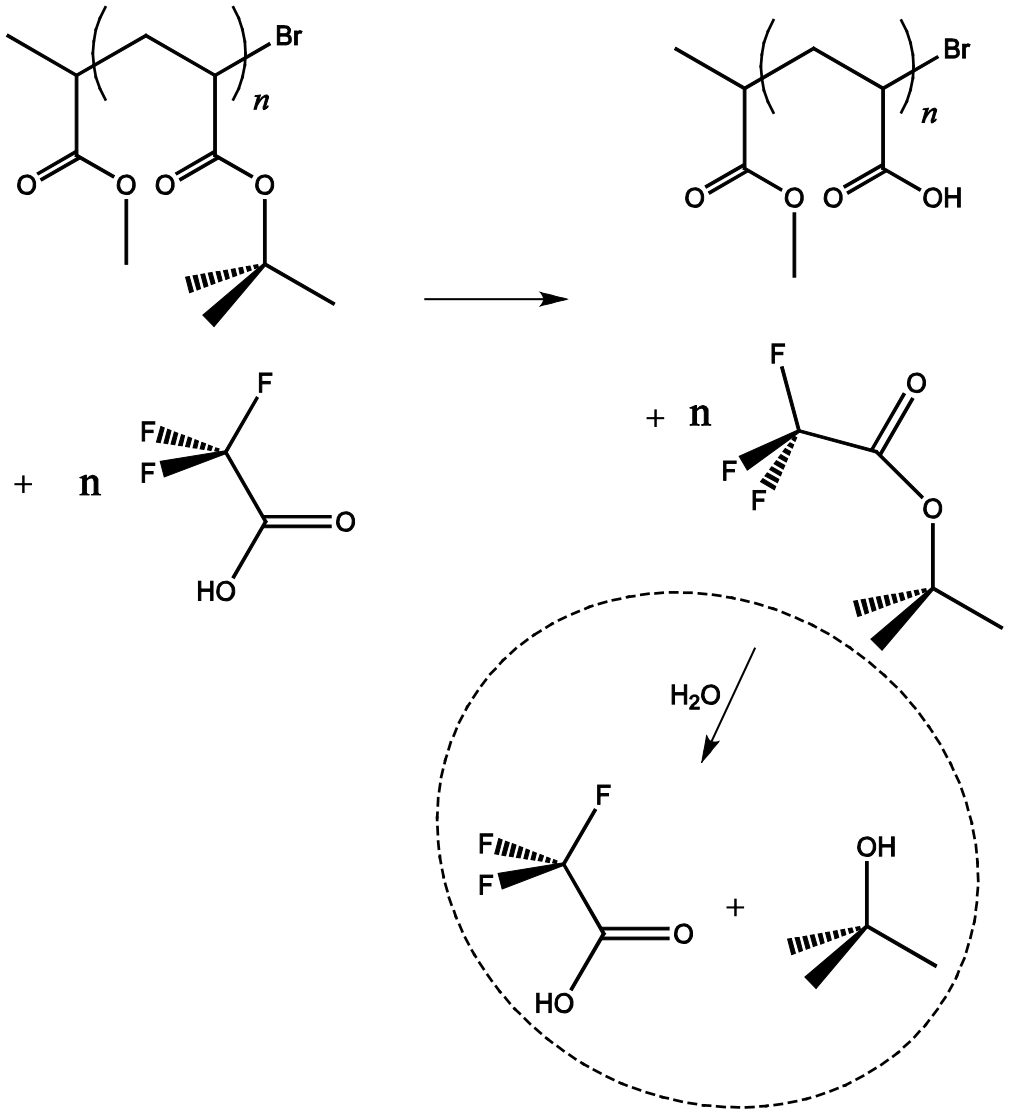

Scheme 4.2 Hydrolysis scheme for the conversion of PtBA to PAA. Possible effect of moisture creating *t*-butanol is shown within the dashed circle.

Figures

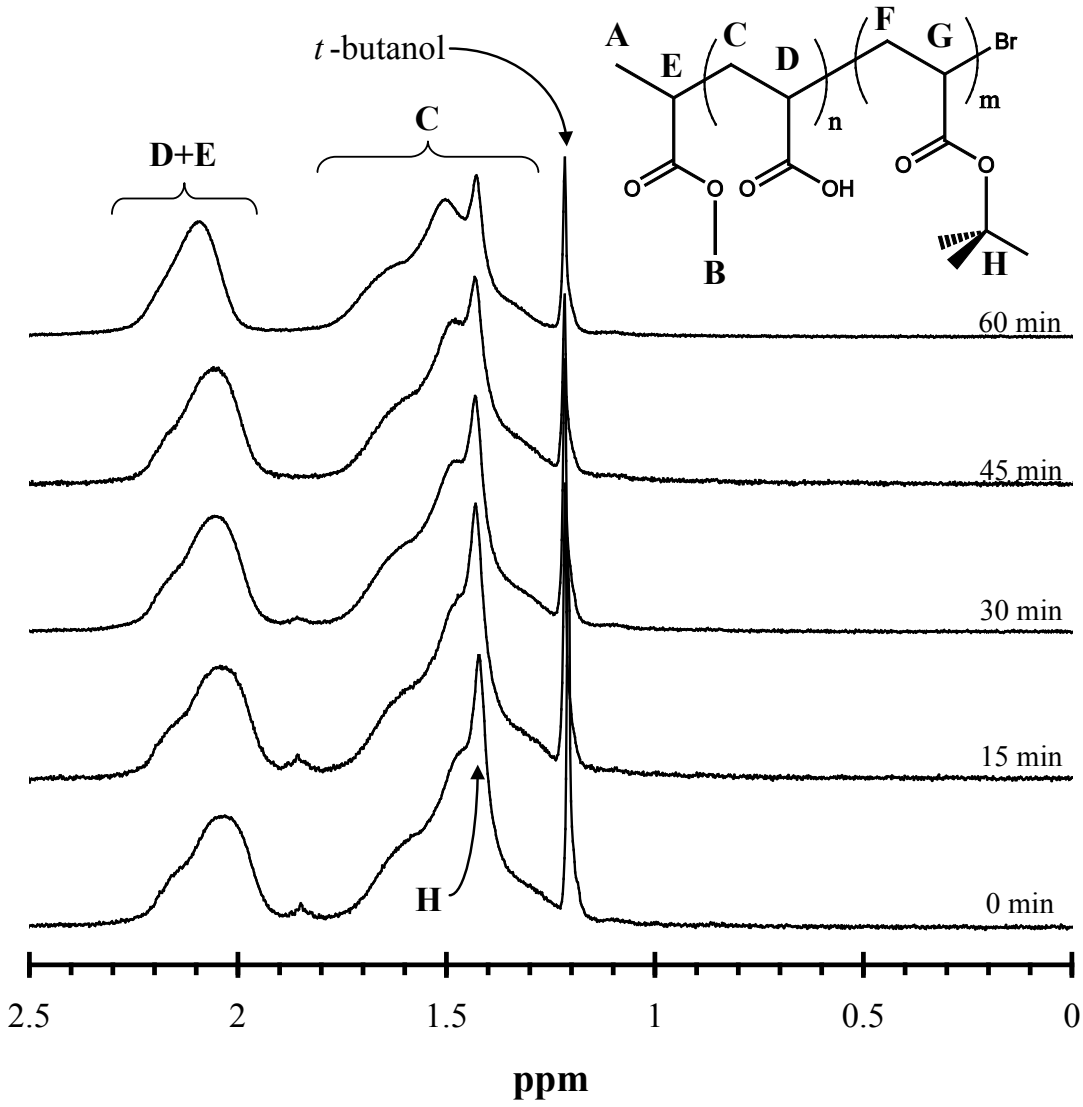

Figure 4.1 ^{1}H NMR spectra showing the progress of a second hydrolysis of the 500 DP ATRP PtBA sample with TFA as followed via NMR. Spectra are labeled according to the length of hydrolysis time. All samples are in D_2O. Peak values are assigned as labeled in the chemical structure at the top.

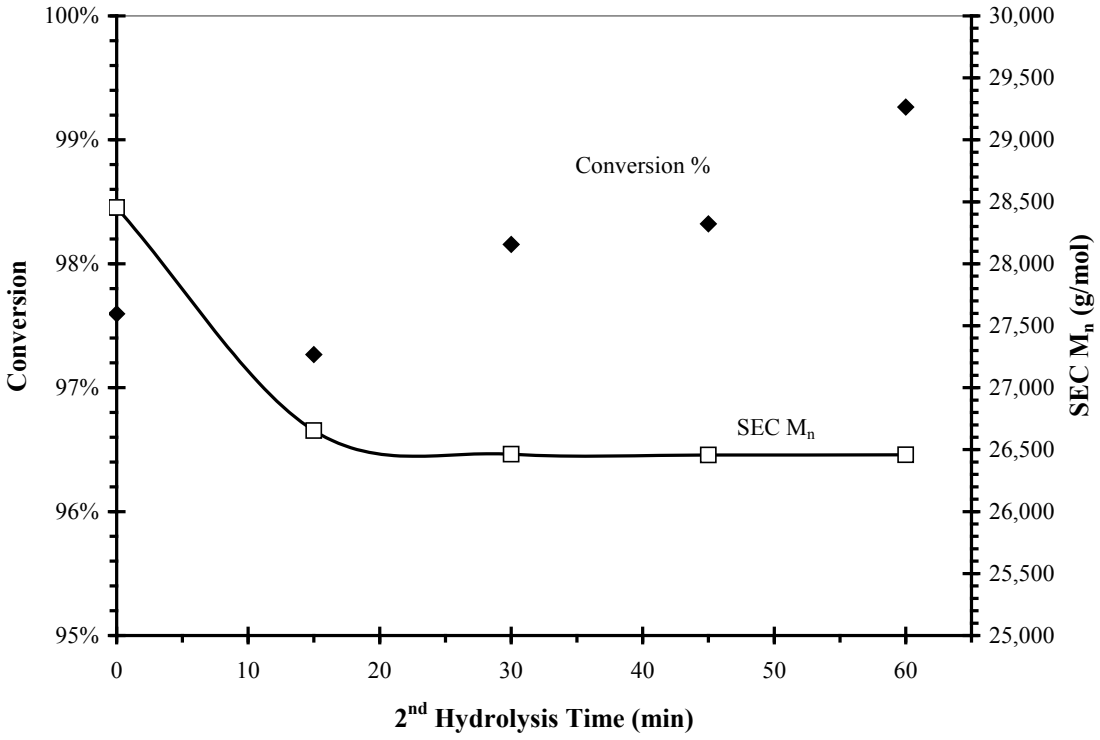

Figure 4.2 The calculated % conversion of *t*-butyl acrylate mers to acrylic acid mers during the 2nd hydrolysis of a ~500 DP ATRP P**t**BA sample. Conversion percentages were calculated from the NMR spectra shown in Figure 4.1. The number average molecular weights of the samples (as determined via SEC) are shown plotted against the secondary ordinate axis as open squares (□).

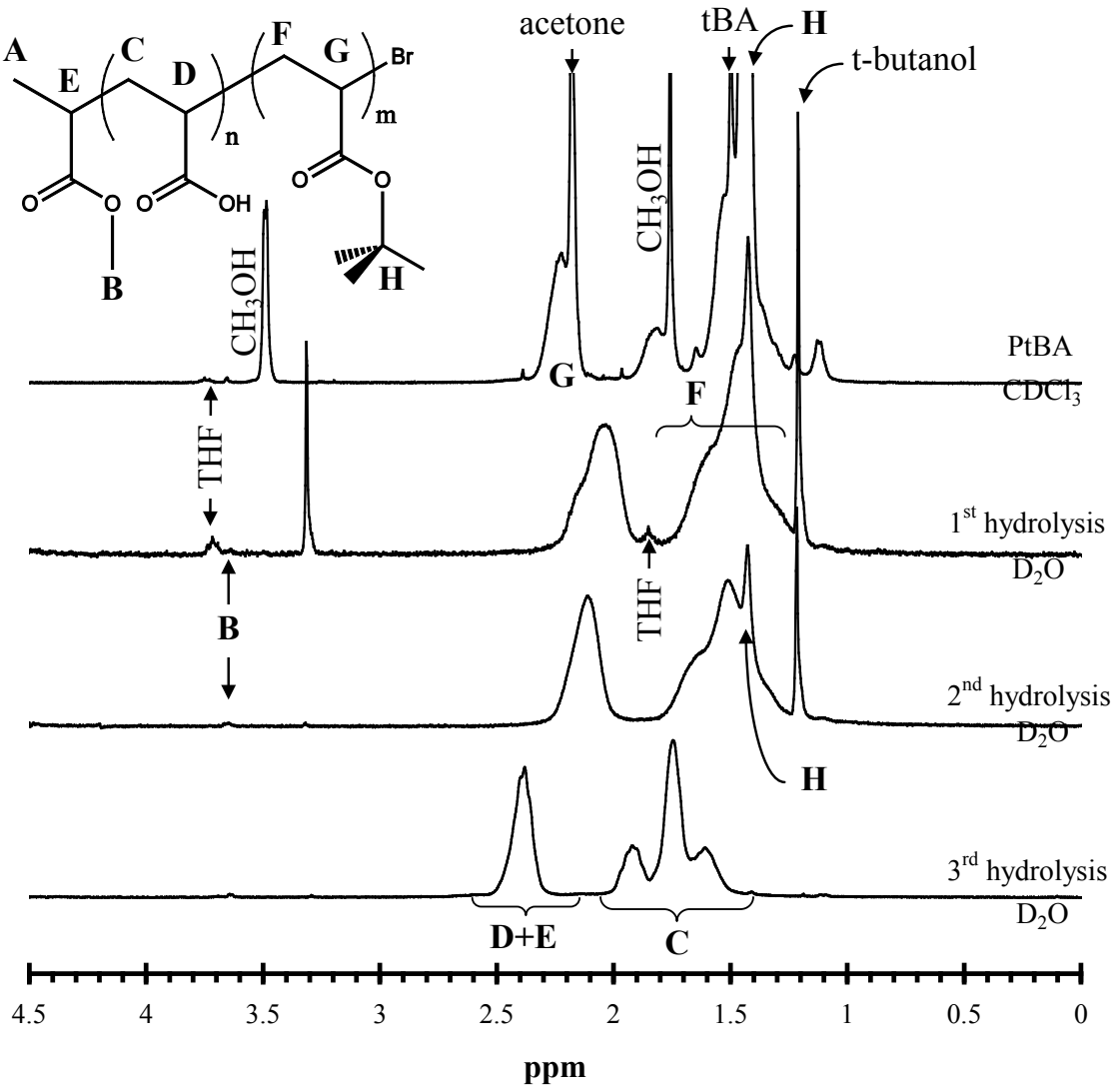

Figure 4.3 NMR spectra showing the progressive conversion of 500 DP ATRP PtBA to PAA via the hydrolysis of the t-butyl acrylate groups. Spectra are labeled according to the number of hydrolysis reactions the sample was subjected to along with the deuterated solvent used during NMR sample preparation. Solvent peaks and PtBA/PAA proton peaks labeled according to notation on chemical structure at top.

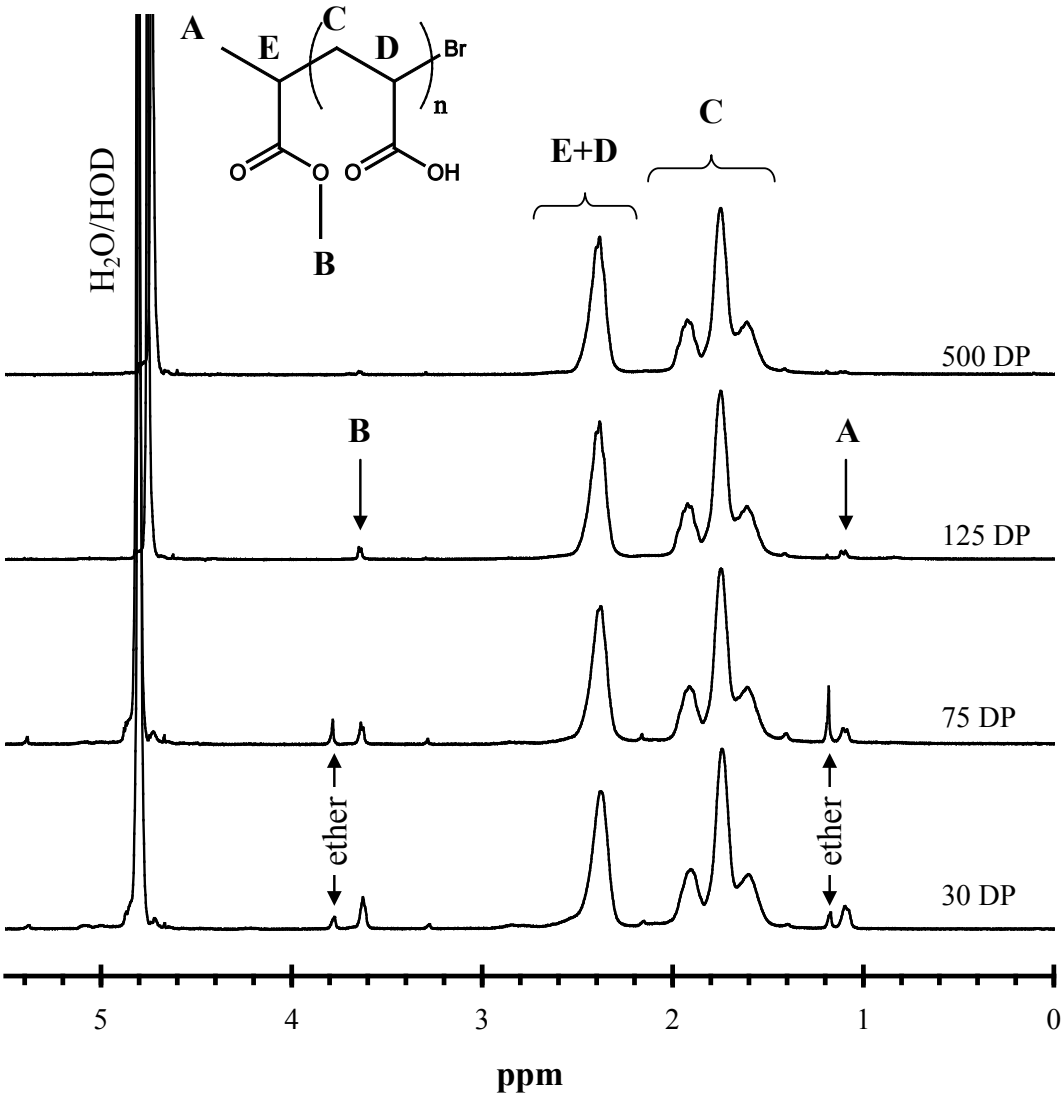

Figure 4.4 NMR spectra for some of the PAA samples hydrolyzed from ATRP synthesized PtBA samples. Spectra are labeled via their goal degrees of polymerization (DP) with solvent peaks and PAA proton peaks labeled according to notation on chemical structure at top.

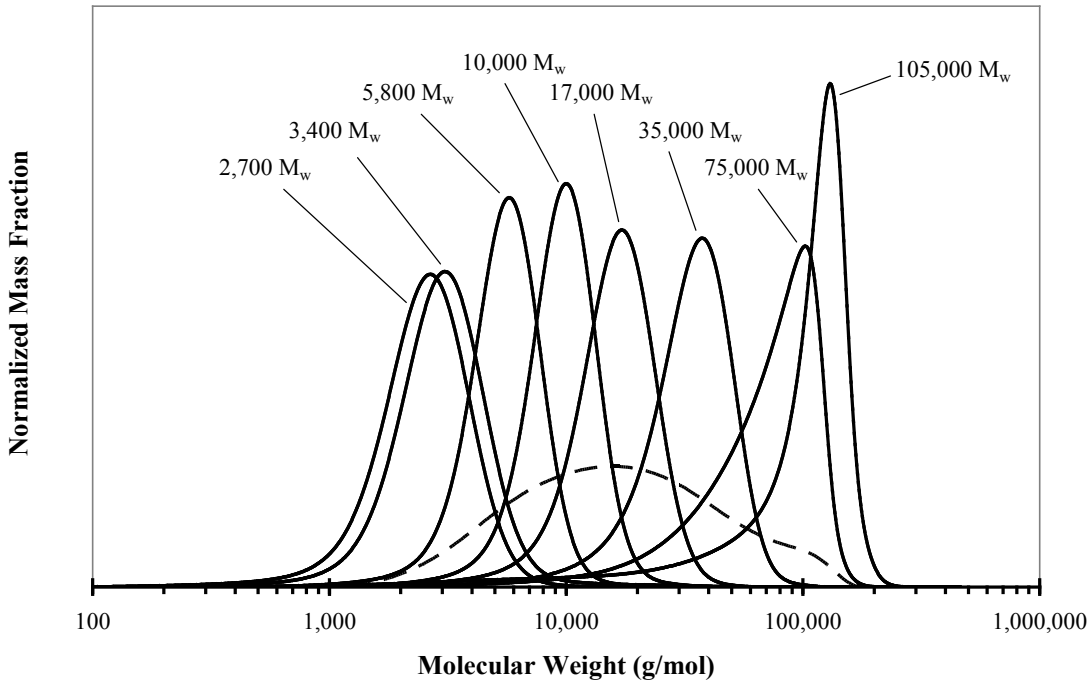

Figure 4.5 Molecular weight distributions of poly(acrylic acid) samples prepared via the hydrolysis of ATRP synthesized poly(*tert*-butyl acrylate) are shown in solid lines. Weight average molecular weights are given to be used to distinguish between samples. The commercially prepared 20k-Na-PAA sample is shown as dashed line. All mass fractions have been normalized with respect to mass (area under their curves).

Chapter 5 – Adsorption of PAA onto Calcite

Introduction

PAA and its conjugate salt, Na-PAA are used extensively in industry as dispersants and antiscalants often times with respect to $CaCO_3$. The adsorption mechanism of PAA onto the solid phase $CaCO_3$ is of utmost importance with regards to its performance since inhibition of the solid scale is most efficient when the antiscalant mechanism works on the surface of growing nuclei rather than in the solution phase prior to nucleation (such as chelation). Guo and Severtson, using an application of classical nucleation theory, have shown previously that carboxylic acid containing polyelectrolytes, PAA and poly(maleic acid), inhibit the formation of $CaCO_3$ scale via mainly surface interactions.[14, 39] As discussed in the previous chapters, the investigation of the mechanisms responsible for PAA inhibition (with particular interest in MW effects) of $CaCO_3$ deposits requires a low PDI sample set and information about how the various MWs interact with the growing $CaCO_3$ particle surfaces.

Fundamental literature for the mechanisms responsible for these surface interactions, and adsorption behavior of PAA onto calcite in particular, is rare and far between, but a few cases do report some adsorption values and trends despite their use of polydisperse samples. In the midst of investigating Na-PAA's dispersant properties, Järnström has reported an equilibrium plateau adsorption of 0.95 mg of 2600 MW Na-PAA per square meter of ground $CaCO_3$ (limestone) in 0.2 M NaCl at pH 9.2.[82] Mäkinen et.al. used commercial $CaCO_3$ (dispersed with a known amount of PAA) and Coatex 70/30 (with a proprietary conc. of PAA) to yield a 6 hour equilibrium plateau adsorption of 1.27 mg of Coatex 70/30 per square meter of $CaCO_3$ in pH 8.5.[83] In the most comprehensive investigation into the mechanisms involved with PAA adsorption onto calcite, Geffroy, *et. al.* outlined the decreasing adsorption as the pH was increased with a final plateau value of just under 0.1 mg/m^2 at pH 10. In addition, they also found that precipitation was a major contributor to the isotherm values once the solution concentration exceeded 1 g/L Na-PAA.[84] We felt it was necessary to expand these findings into the higher

regions of pH where kraft process liquors reside while remaining at low dosage concentrations (which is common practice) where precipitation is not an issue. Just outside of the PAA interaction with $CaCO_3$ realm, PAA adsorption onto other sparingly soluble salts has been documented. Vreugd *et. al.* investigated the adsorption of both PAA and its higher charge density counterpart poly(maleic acid) (PMA) onto CaF_2. They reported some similar trends as shown here such as a lack of MW dependence upon adsorption at high pH ranges with a plateau concentration of 0.3 mg/m^2 at pH 10.[85]

In this chapter, adsorption studies are focused on determining the interactions between PAA and calcite surfaces. As outlined in the previous chapters, the molecular weight dependence of the antiscalants is taken into consideration specifically with the use of the low PDI PAA samples from Chapter 4 being particularly useful in isolating MW effects which can then be expanded to incorporate the more common commercial (high PDI) PAA antiscalants.

Materials and Methods

Chemicals and Materials

Powdered calcium carbonate was purchased from Sigma Aldrich (St. Louis, MO) as precipitated $CaCO_3$ and was used without purification or further grinding. Brunauer-Emmett-Teller (BET) surface area analysis was carried out using a Micromeritics (Norcross, GA) ASAP 2000 gas sorptometer. Average measured surface area of the $CaCO_3$ crystals was 8.2437 m^2/g. X-ray diffraction (XRD) analysis carried out using a Bruker-AXS (Siemens, Karlsruhe, Germany) D5005 X-ray diffractometer XRD confirmed the sole phase to be calcite. Na_2CO_3 and $CaCl_2$ were from Fisher Scientific (Pittsburgh, PA). Doubly de-ionized water used for all solution preparations had a resistivity of equal to or greater than 18 MΩ. Commercial poly(acrylic acid) and sodium polyacrylate (PAA & Na-PAA, respectively) were purchased from Polysciences, Inc. (Warrington, PA) and SEC was used to confirm the broad molecular weight distribution. RAFT Na-PAA samples were provided by Kemira Chemicals (Marietta, GA). Poly(acrylic acid) samples with narrow molecular weight distributions were synthesized

as described in Chapter 4. All of the molecular weight distributions of the polymer samples used are shown in Figure 5.1.

Experimental

Adsorption isotherms were collected for the high PDI PAA & Na-PAA samples as well as for the low PDI PAA samples onto calcite crystals at high pH. Adsorption isotherm studies were modeled after the suggestions presented by Fleer and his colleagues.[86] The aqueous phases were made by diluting selected polymer samples (in aqueous form) with a saturated $CaCO_3$ solution of DDI H_2O to produce a concentrated stock solution used for the entire isotherm. This stock solution was diluted further with saturated $CaCO_3$ solution to various concentrations and adjusted to pH 12 with NaOH. Initial samples were taken of this solution. Solid $CaCO_3$ was then added at an approximate weight percentage of 5%. Each slurry was isolated by wrapping the containing beaker with Parafilm® and stirred vigorously through equilibrium sample collection. The equilibrium sample of the slurry was collected after 24 hours of mixing and pushed through a 0.45 μm PTFE syringe filter. This process was repeated using 8 different polymer concentrations (typically 50 to 600 mg/L) of initial aqueous phases to produce 8 points per isotherm. Kinetics isotherms varied only in the respect that multiple samples were taken at various time intervals.

Equipment

Size exclusion chromatography (SEC) was performed on an Agilent (Santa Clara, CA) 1200 Series HPLC with a UV-detector (λ = 215 nm) using Waters (Milford, MA) 250 & 120 Ultrahydrogel columns in series with a 0.3 M NaCl, 0.1 M NaH_2PO_4 eluent buffered solution (pH 7.0) pumped at 0.85 mL/min. A series of eight Na-PAA standards from Polymer Laboratories, Inc. (Amherst, MA) with molecular weights ranging from 1,250 to 323,000 g/mol were used to calibrate the system with all MWs being relative to these standards. Samples were prepared by mixing filtered isotherm solution with an equal volume of doubly concentrated eluent (0.6 M NaCl, 0.2 M NaH_2PO_4) buffered to pH 4.5 in order to prevent any precipitation of $CaCO_3$ in the columns.

SEC was utilized to analyze both the initial and equilibrium samples of the aqueous phase for both concentration and molecular weight distribution (MWD) changes. Initial samples, taken before solid $CaCO_3$ was added, were used to correlate the UV absorbance (λ = 215 nm) of the SEC detector to the known polymer concentration. This calibration method had a nominal correlation of $R^2 > 0.99$ although it should be noted that concentrations below 2 ppm were difficult to resolve. MWDs were determined via calibration of the SEC system with Na-PAA standards from Polymer Laboratories®.

Nitrogen adsorption/desorption measurements were performed on a Micromeritics (Norcross, GA) ASAP 2000 gas sorptometer. The $CaCO_3$ samples were outgassed at 0.003 mmHg for 24 hours at 200 °C prior to measurement. The $CaCO_3$ adsorption substrate displayed a Brunauer-Emmett-Teller (BET)[87] surface area of 8.2437 m^2/g.

Results & Discussion

It has been claimed numerous times that the kinetics of polyelectrolyte adsorption has not been studied as intensely as that for adsorption of nonionic polymers.[86, 88] In conjunction with this, the replacement kinetics of differing sized non-ionic polymers is also lacking of systematic studies[89] with polyelectrolyte replacement being completely ignored. As for adsorption kinetics of uncharged homopolymers, Dijt and his colleagues make a strong case for mass-transfer being the limiting step in highly controlled systematic studies.[90, 91] A result of this mass-transfer limitation leads to their hypothesis that the adsorbed polymer layer is in a constant equilibrium with the immediately adjacent layer of solution phase polymer, which leads to their work in exchange kinetics of different sized polymers.[89] There they describe the difference in adsorption rates for high and low MW polystyrene. Although, this comes in stark contrast for polyelectrolytes at high pH (as described above) where there isn't a dependence upon MW for adsorption plateau concentrations, suggesting that the rates will also be similar.

Another difference between adsorption behavior of non-ionic polymers and polyelectrolytes is with regards to their conformation at the surface. Non-ionic polymers are known to adsorb to surfaces with many loops and tails left hanging in solution. In contrast, polyelectrolytes tend to adsorb with more of a flat conformation. When this

information is coupled with the re-conformation results of PAA onto alumina[90], one can hypothesize that although the electrostatic interactions are much more influential in determining adsorption, eventually the entropic gain resulting from larger MW species residing on the surface will win out.

As with any adsorption isotherm method, a precise measurement technique is required to measure either the concentration of adsorbate on the surface or in solution. Since the molecular weight dependence of the adsorbing PAA was of primary concern for this study, SEC coupled with UV absorbance was chosen as the measurement method. An advantage of using SEC is that the concentration of the PAA in solution could be determined precisely while at the same time, the determination of the MWD could also be performed. With the supernatant concentrations being considered, the amount of adsorbed PAA per area of calcite, Γ, was determined indirectly using

$$\Gamma = \left(c_p - c_0\right)\frac{V}{A_s} = \Delta c_p t_s \qquad (1)$$

with Δc_p representing the difference in the solution phase polymer concentrations before and after adsorption (c_o and c_p, respectively) and t_s representing the average thickness of solution adjacent to the surface calculated as the quotient of the total volume of solution, V, and the total surface area of the calcite phase, A_s. The total surface area was calculated as the product of the known mass of calcite added and its N_2 adsorption (BET) value as reported in the Experimental section.

In Figure 5.2, the SEC MWDs of a typical sample are shown both before and after adsorption. In this case the initial polymer concentration was ~450 mg/L 20k-Na-PAA (active acids). As can be seen, the area under the MWD curve changes significantly after the polymer adsorbed to the calcite surfaces. The change in solution concentration, Δc_p was quantified by taking advantage of the linear relationship between absorption and concentration (Beer's Law) and summing up all of the recorded UV detector responses during the polymer elution time range (area under the curve). Shown in Figure 5.3 is a typical calibration curve expressing the proportionality between the calculated area under

the curve and the known PAA concentration at $\lambda = 215$ nm. It should be mentioned that although hydroxide ions have been documented to absorb UV radiation around this wavelength ($\lambda \leq 220$ nm),[92] careful control over the SEC eluent pH allowed for a consistent baseline UV absorbance. It was found that batch preparations of SEC eluent, along with individual calibration curves for each isotherm analyzed, were required to produce reliable linear correlations between the SEC areas and polymer concentrations with the example R^2 value shown in Figure 5.3. It was found through the numerous calibration files created that correlations remained reliable as PAA concentrations decreased until the area under the SEC curve dwindled to the point where the signal-to-noise ratio became significant (~2 mg/L PAA even at the highest sample injection volume, 100 μL).

Shown in Figure 5.4 are the collected isotherms for some of the various PAA samples after allowing 24 hours for adsorption. Included samples spanning a range of MWs from 3,000 to 75,000 and PDIs of 1.3 to 4.2 and encompassing ATRP, RAFT, and commercial (free-radical) polymerization methods are shown. The mass of polymer adsorbed to the surface, Γ, is plotted versus the mass of polymer in the solution phase, $c_p t_s$, where c_p is the volumetric concentration in solution and t_s is the volume of the solution phase per surface area of the calcite phase. Where the typical isotherm relating the adsorbed amount to the solution concentration suffices for small molecules and monodispersed polymers, plotting Γ vs. c_p for polydispersed samples can give rise to different looking isotherms depending upon the ratio of solution volume to solid surface area.[93, 94] It is common practice to therefore normalize the adsorption isotherm curves of polydispersed polymer samples by plotting the mass of polymer on the surface, Γ, as a function of the mass in solution, $c_p t_s$, (with both masses being reported per unit area of available surface). A typical high affinity monolayer adsorption behavior was exhibited for all samples tested with a rapid change from complete adsorption to a plateau level after concentrations exceeded the saturation concentration. Saturation of the calcite surfaces appeared to be constant over all tested MWs and polydispersities. All isotherms were fitted using the Langmuir adsorption model:

$$\frac{\Gamma}{\Gamma_{sat}} = \frac{\alpha c_p t_s}{1 + \alpha c_p t_s} \quad (2)$$

where Γ_{sat} represents the plateau value of the adsorption curve (surface saturation concentration) and α is representative of the adsorbate's affinity for the surface.

Fitting the individual isotherm curves with Equation 2 yielded a consistent surface saturation concentration, Γ_{sat}, of 0.43 mg/m^2 within experimental error which is on the order of magnitude found for other highly charged polyelectrolyte adsorption values at low salt concentrations.[86, 95]

The constant saturation concentration over all MWs from Figure 5.4 suggests that the conformation of the adsorbed polymers was flat with little to no loops or tails since a non-flat conformation would suggest that higher MWs would adsorb larger amounts as their loops and tails not in direct contact with the calcite surface would increase the amount of polymer mass attached to the solid phase. This conclusion is not unreasonable since the constant Γ_{sat} implies nominal surface area coverage per PAA repeat unit of 27.8 Å^2. Also, due to the relatively high pH, the PAA would be close to if not completely ionized and the adsorption conformation would be expected to lack loops and tails.[95] Even at a pH value as low as 8.25, the conformation of adsorbed PAA on alumina (isoelectric point ≈ pH 8.5) has been shown to be initially flat.[96] At pH 10, it has been shown that PAA will adsorb to alumina despite the obvious electrostatic repulsion, but will not presume a flat conformation until the pH is lowered enough to switch the charge on the surface.[97] Here, the flat adsorption conformation (at a pH greater than calcite's isoelectric point of 10.4 ± 0.3)[98] suggests that the interaction between the ionized carboxylic acid functional groups and the calcite lattice is stronger than with alumina. This strong interaction was also shown by Mann and his colleagues where he noted that carboxylic acid groups interact specifically with the calcite structure,[15, 17] essentially becoming a substitute (of lesser charge) for the trigonal planar CO_3^{-2} cation within the lattice structure.

In contrast to the reliability of the Γ_{sat} values, the affinity values, α, were not as reliable due to the high affinity nature of the isotherm curves. The typical method of using linear regression to determine the slope and intercept of the data when plotted as the inverses of Γ and $c_p t_s$ such as

$$\Gamma^{-1} = (\alpha \Gamma_{sat})^{-1} (c_p t_s)^{-1} + \Gamma_{sat}^{-1} \quad (3)$$

yields Γ_{sat} as the inverse of the intercept and α as the quotient of the intercept and slope. This form, along with the non-linear form of Equation 2, requires a significant fraction of data points between the completely adsorbed range (where $c_p t_s \approx 0$) and the completely saturated state where $\Gamma \approx \Gamma_{sat}$. Do to the extremely high-affinity nature of all the PAA isotherms tested, the range between $c_p t_s \approx 0$ and $\Gamma \approx \Gamma_{sat}$ was quite small. Therefore, the determined affinity values, α, for the various samples could not be determined precisely, but were typically on the order of 10^5 suggesting a high propensity for any polymer in solution to adsorb to available calcite surfaces.

As noted above, the advantage of using SEC (with a UV absorbance detector) was to not only get concentration values, but also a clear picture of the MWD changes upon adsorption. As exemplified in Figure 5.2, all MWDs shifted towards higher MWs upon adsorption. This trend suggested that lower MW species were preferentially adsorbed over the 24 hours allotted for each experiment. Since it is fairly well known that higher molecular weight species adsorb preferentially at equilibrium, not due to an increase in anchoring points but rather due to the entropy decrease in mixing in the solution as MW increases,[86] the path of the isotherm MWDs toward their final equilibrium state became a point of interest. Although the specific interaction and incorporation of the ionized carboxylic acid functional groups as mentioned above would suggest a tendency for the adsorbed polymer to remain attached, in reality the rate at which ions of the lattice desorb and are replaced by similar ions from solution would have more effect on replacement rates.

Upon noticing that all solution phase MWDs shifted towards higher MWs upon the removal of adsorbed polymer as exemplified in Figure 5.2, the rates of adsorption of the different MW species were investigated.

In Figure 5.5, the adsorption rate for select PAA samples is shown plotted as the Langmuir-fitted Γ_{sat} values vs. adsorption time in order to elucidate the effects of MW on the rate of adsorption. It was assumed that the smaller low molecular weight (LMW) species were adsorbing faster and therefore creating the observed preference for lower molecular weights on the surface. Isotherm plots were collected and again fitted with the Langmuir model for adsorption. The Γ_{sat} values were then determined at various times and plotted against the log of time allowed for adsorption as shown in Figure 5.5. However, there appeared to be no noticeable trend with respect to the MW and PDI of the sample and the rate at which Γ_{sat} increased. However, the individual SEC elugrams for the PAA in solution still showed an obvious preference for LMW species on the surface when polydisperse samples were tested. In order to ensure that the ATRP synthesis method of the low PDI samples was not responsible for the lack of distinction between adsorption rates, a mixture of various low PDI samples having a similar M_w and polydispersity as the tested commercial sample was prepared and tested. Similar results to the commercial sample were obtained.

The individual adsorption isotherms for the mixture of low PDI ATRP PAA samples at various adsorption times are plotted in Figure 5.6, with initial polymer solution phase concentrations of 175 mg/L and 300 mg/L shown as open squares (□) and diamonds (◊) respectively. The individual SEC elugrams from concentrations below and above the 24 hour adsorption saturation level are shown in Figures 5.7 and 5.8, respectively. As can be imagined, the area under the SEC curves dwindled to zero as nearly all of available polymer molecules adsorbed to the surface in Figure 5.7. Figure 5.8 shows the eventual partial displacement of the LMW species which originally adsorbed to the calcite surfaces with the HMW species from the solution, but not until≥24 hours, for adsorption within the plateau region of the isotherms. This supported the idea that LMW species

were preferentially adsorbing not due to a thermodynamic standpoint, but rather a kinetically faster standpoint.

Figure 5.9 exemplifies the differences between adsorption and displacement after 24 hours. The SEC detector response for select MW fractions (near the four maxima) in solution is plotted vs. the time allowed for adsorption (in log scale) for the mixture of ATRP PAA sample. A linear fit of the data points below 24 hours was extrapolated for the selected MWs and plotted as dashed lines. Thus the difference between the experimentally detected amounts and the extrapolated amounts at longer adsorption times could be considered the amount of polymer active in the exchange process. For the lowest MW shown, 3,000 g/mol PAA mass fraction was obviously at higher concentrations in the solution phase after 24 hours than would be expected purely from the lower adsorption times. In contrast, the HMW fractions were at lower concentrations than expected if no displacement occurred. This outlines in detail what can be seen in Figure 5.8. As LMW polymers are displaced from the surface, extra HMW polymers are adsorbing than would've been expected from analyzing the samples prior to the 24 hour sample.

The rates as determined via the kinetics studies of the low PDI samples at different MWs did not show a clear difference in their rate of adsorption, but the preference for LMW species on the calcite surfaces was still present, as can be seen from Figures 5.7 thru 5.9. Apparently, the preference for LMW during the initial adsorption originates not from a simple rate comparison but rather from a competitive aspect between different MW species.

To address the conformation of the adsorbed PAA molecules on calcite, a slight detail of the Γ_{sat} vs. adsorption time plots in Figure 5.5 suggests a change in the amounts of loops and tails occurring at approximately the same time that HMW species are replacing the LMW species already adsorbed. Up until ~24 hours, the amount of polymer adsorbed follows a logarithmic trend as the surface becomes saturated with PAA. After ~24 hours, the total mass of the adsorbed polydisperse samples begins to increase beyond the logarithmic trend as HMW species replace the LMW species on the surface. This

suggests that the mass of polymer species exchanged between the surface and the solution is not conserved. Rather, the number of polymers adsorbed can be shown to remain relatively constant over the exchange period monitored.

Plotted in Figure 5.10 are the MWDs as mole fractions for the experimentally determined and hypothetically extrapolated distributions of PAA in solution after 4 days (96 hours) of adsorption for the solution starting with a concentration of 300 mg/L. Extrapolations for all SEC MW fractions were carried out by fitting every equivalent fraction at adsorption times less than 24 hours with the empirical exponential decay formula,

$$h_i = a_i e^{b_i t} + c_i \tag{4}$$

where h_i denotes the detector response of the i^{th} mass fraction at adsorption time, t. The fitting constant, b_i, suggests the rate of adsorption for MW species characterized by the i^{th} fraction and c_i would be its hypothetical mass concentration at infinite time if no displacement occurred. Obviously, $a_i + c_i$ would then be the initial concentration of the i^{th} mass fraction before adsorption. Fitting the data in this manner allowed for a much more accurate and comprehensive comparison between the desorption of LMW species as they were being replaced with HMW species. These fitting constants were then used to calculate hypothetical MWDs void of displacement effects. Figure 5.10 shows the mole fractions of the experimental and the hypothetical MWDs. The molecules active in the exchange process, the difference between these two MWDs, is also plotted in Figure 5.10 to show the clear conservation of the total LMW molecules desorbed (positive area) and the total HMW molecules displacing them (negative area).

Upon comparison of all SEC fractions (not just the selected fractions shown in Figure 5.9) the total polymer species desorbed from the surface and that which was adsorbed (in excess of the extrapolated amount) as shown in Figure 5.10, it was found that 65% extra mass was adsorbed during the exchange process. In contrast, when SEC data was converted into mole fractions, it was found that less than 1% extra molecules were

adsorbed during the exchange process. This demonstrates a clear 1-to-1 stoichiometric exchange process.

Figure 5.11 outlines a simple explanation for this 1-to-1 molecular exchange which follows from the assumptions that there are a finite number of adsorption sites on the calcite and that the PAA initially adsorbs flat on the surface (although *not* necessarily linearly). As a LMW molecule desorbs (area 3), it frees up adsorption sites on the calcite where a HMW molecule displaces it. Since the surface is already saturated with adsorbed PAA and the HMW molecule is larger than the LMW molecule it is displacing, there will be an excess of mass from the HMW molecule which will not be in contact with the surface but still considered to be adsorbed as loops and tails (area 4). Those loops and tails are now responsible for the increase in mass adsorbed to the surface. It is presumed that eventually all LMW molecules will be replaced by the larger MW species but that the loops and tails of the exchanged HMW molecules will be responsible for adsorbing onto the locations left by the final desorbing LMW molecules (area 5). Thus, the actual equilibrium state, where the calcite surface will be completely saturated with only HMW species, will eventually occur (area 6). The actual amount of time required for complete saturation by only HMW species is still unknown as the length of the experiment becomes impractical and easily prone to increasing error.

Conclusions

It has been shown here, and schematically represented in Figure 5.11, that the adsorption of poly(acrylic acid) onto calcite goes through a number of distinct MWDs and conformation stages on its way to equilibrium. The initial adsorption MWD is driven by competitive kinetics between the PAA species followed by replacement and eventually re-conformation. The metastable period immediately after the initial saturation of the calcite surface with PAA (~ 24 hours) yields a constant adsorption concentration of 0.43 mg/m^2 independent of the molecular weight of the adsorbate. This suggests a relatively flat adsorbed polymer conformation. The MWD of the adsorbed PAA shows a strong preference for lower molecular weights even though the adsorption rates of the individual species do not show any strong trend with respect to their MW.

An in-depth look at the MWD of the adsorbed PAA after the initial saturation period exposed a 1-to-1 replacement of LMW molecules with HMW molecules from the solution phase. This overloading of the mass of PAA with respect to the available surface area caused an increase in the adsorbed mass while conserving the number of molecules adsorbed. It is expected that this conservation of molecular concentration at the surface will be interrupted as additional equilibrium time allows for the displacement of all LMW species with the loops and tails of the HMW species already adsorbed.

The processes shown in this chapter remain possible at longer time frames than the use of PAA as an antiscalant requires. A typical use of PAA within a kraft pulping mill will only require the inhibition of $CaCO_3$ scale from depositing over a range of a few hours. Although, it should be pointed out that where the isotherms shown here involved the adsorption of PAA onto *existing* calcite surfaces the PAA used at the mill inhibits the *growth* of these $CaCO_3$ surfaces. Especially in terms of the exchange kinetics, it is very likely that growth of the $CaCO_3$ precipitates may speed up the effects of this process. The next chapter will discuss some techniques and methods used to investigate the more complex process (and system) of the adsorption and eventual inhibition of $CaCO_3$ at high pH with PAA.

Figures

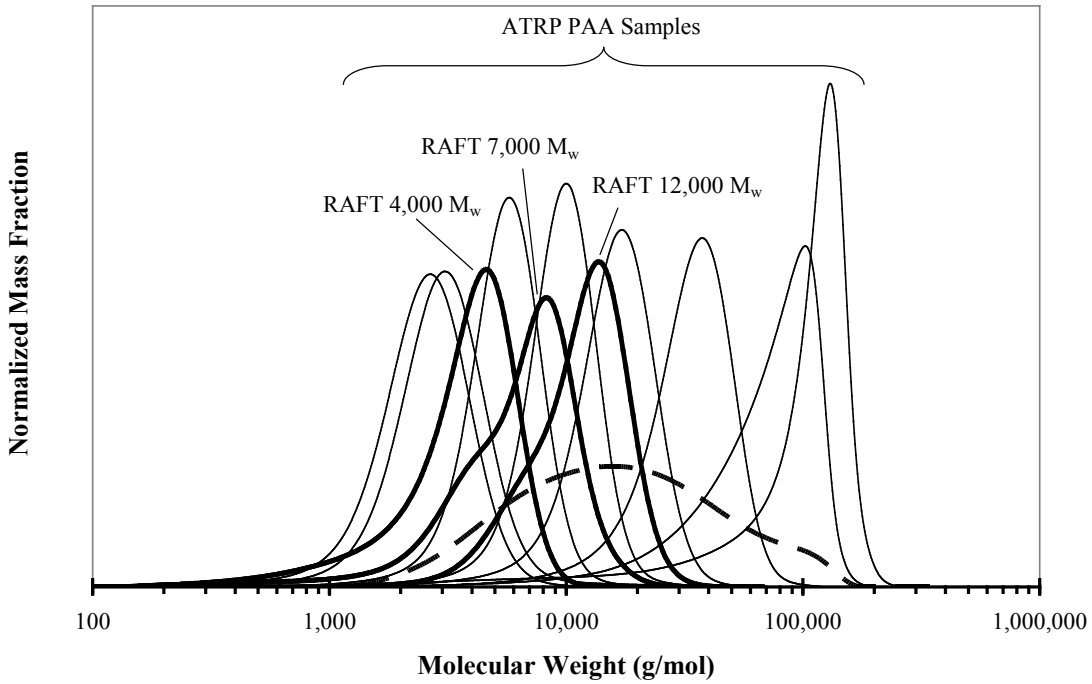

Figure 5.1 Molecular weight distributions of PAA and Na-PAA samples synthesized using various techniques. The eight different ATRP PAA samples prepared as described in Chapter 4 are shown as thin lines. Na-PAA samples synthesized using RAFT polymerizations are shown in thick lines denoted with their SEC determined M_w values. The 20k-Na-PAA commercial sample used in Chapters 2 and 3 is shown as a dashed line for reference. All MWD intensities shown have been normalized in order to maintain equal areas under their respective curves.

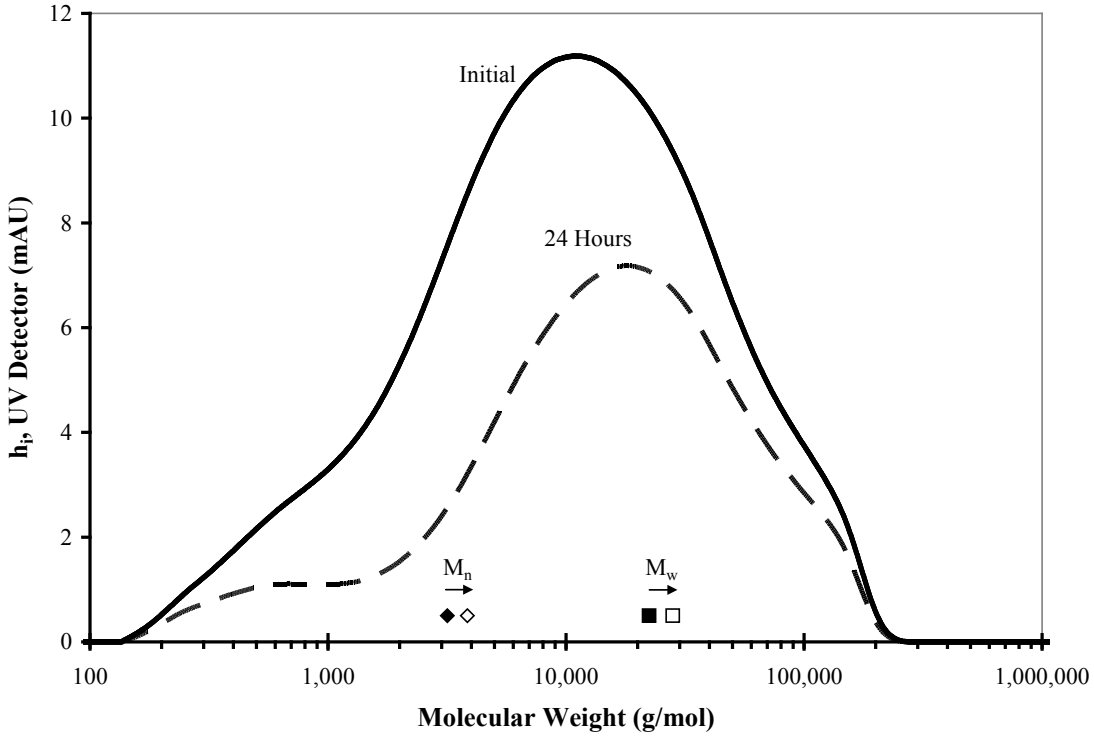

Figure 5.2 UV detector response (λ = 215 nm) showing the amount and MWD of 20k-Na-PAA sample before and after adsorption to calcite at pH 12. The number and weight average molecular weights are shown as closed symbols for the initial MWD (♦ and ■ respectively) and open symbols for the MWD after 24 hours(◊ and □ respectively). The areas under the MWD curves were converted to concentrations via the use of the calibration curve in Figure 5.3.

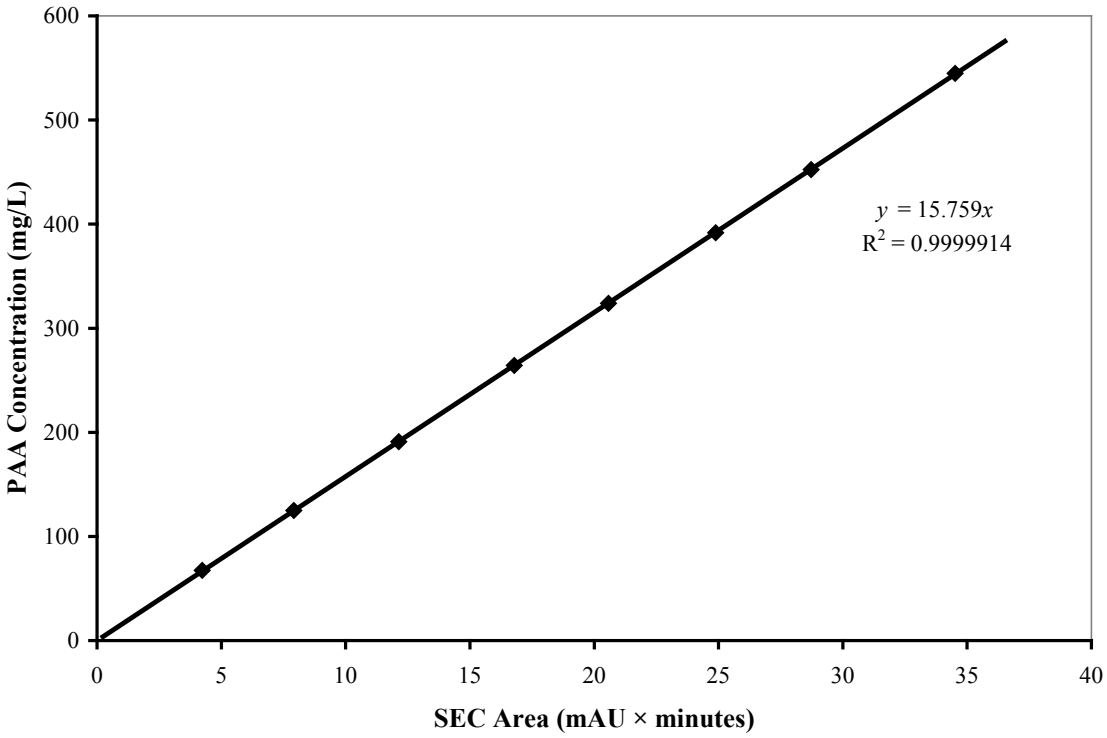

Figure 5.3 Calibration line using the UV absorbance (λ = 215 nm) of 20k-Na-PAA (plotted as the active acid equivalent of PAA) concentration with respect to area under the SEC elution curve. The data was fit with a linear line encompassing the ordinate.

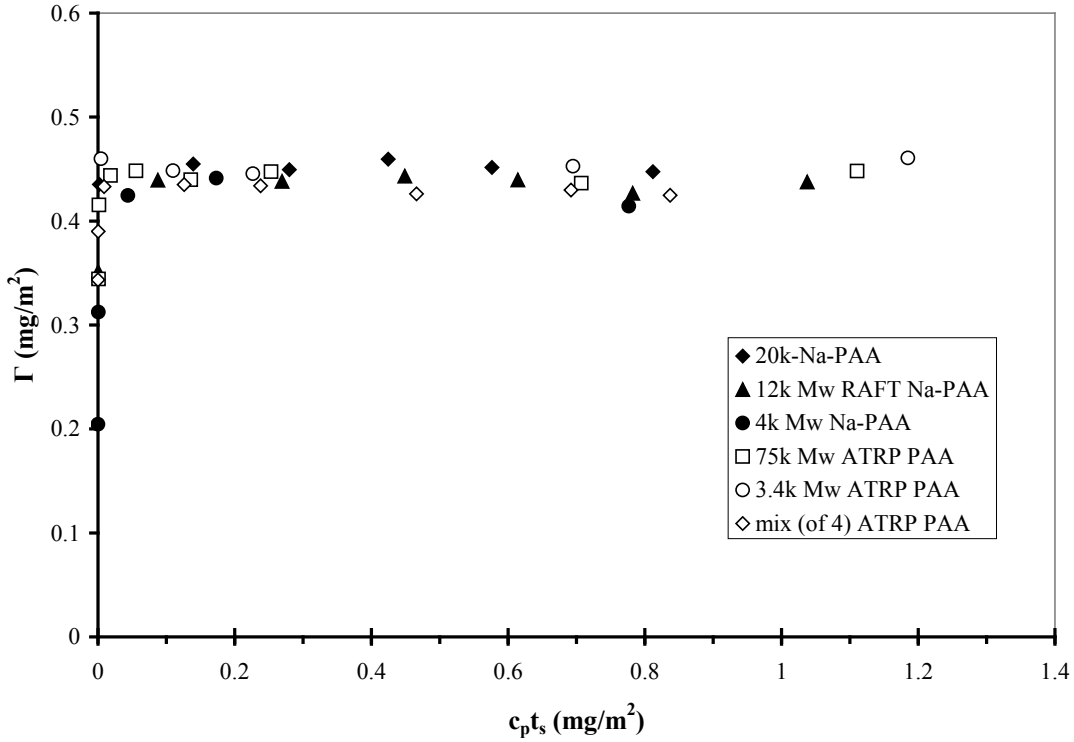

Figure 5.4 Single day adsorption isotherms of Na-PAA and PAA from various sources onto calcite at pH 12. Commercial Na-PAA (~20,000 MW) along with two of the RAFT polymerized Na-PAA samples are shown as closed symbols. The two low PDI PAA samples synthesized via ATRP and hydrolysis of PtBA are shown in open circles. A mixture of four ATRP PAA samples intended to mimic the MWD of the 20k-Na-PAA is shown in open diamonds (◊).

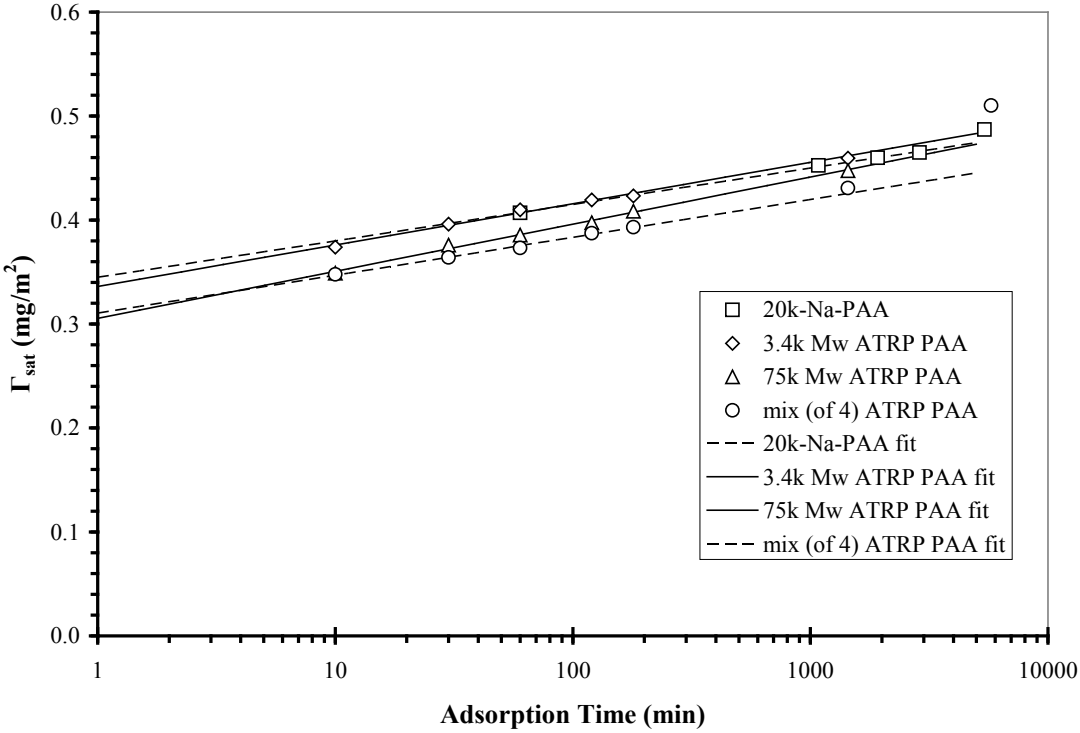

Figure 5.5 Adsorption rates of various PAA samples. 3,400 M_w (◊) and 75,000 M_w (Δ) ATRP PAA samples are shown with logarithmic fits (solid lines). Polydisperse samples, 20k-Na-PAA (□) and the mixture of 4 ATRP PAA samples (○), are shown with dashed lines as logarithmic fits for samples below 30 hours (1800 minutes).

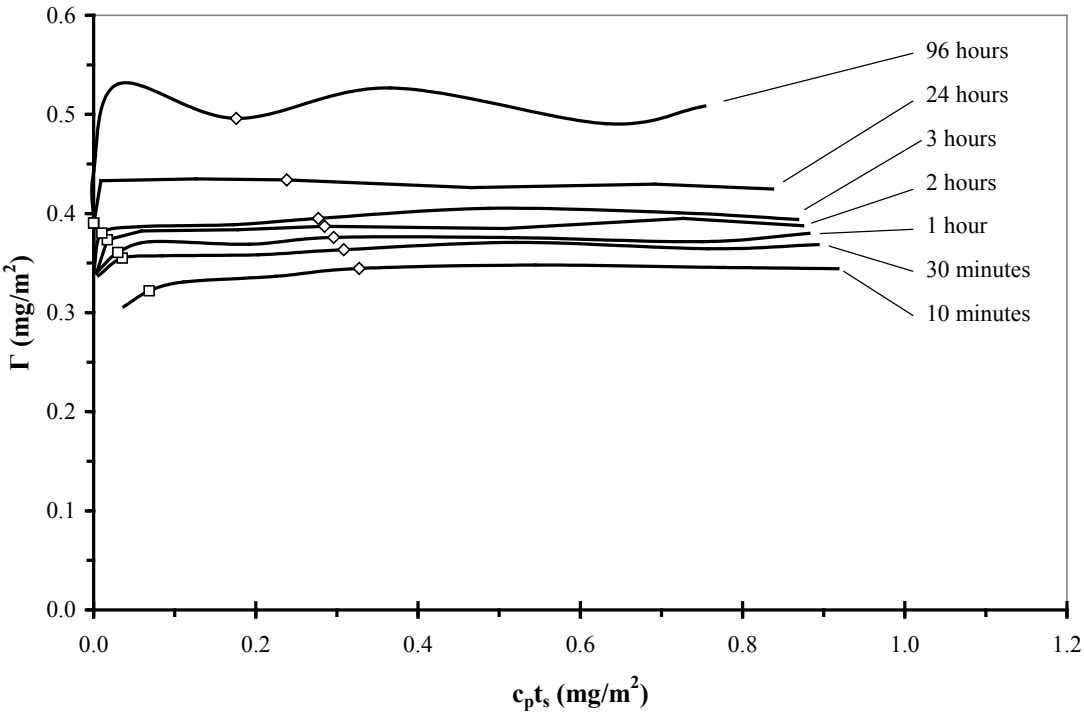

Figure 5.6 Individual isotherms at various sample times for the polydisperse mixture of ATRP PAA samples. Solution phase MWDs are shown in Figures 5.7 and 5.8 for the samples initially at 175 and 300 mg/L PAA (□ and ◊ respectively).

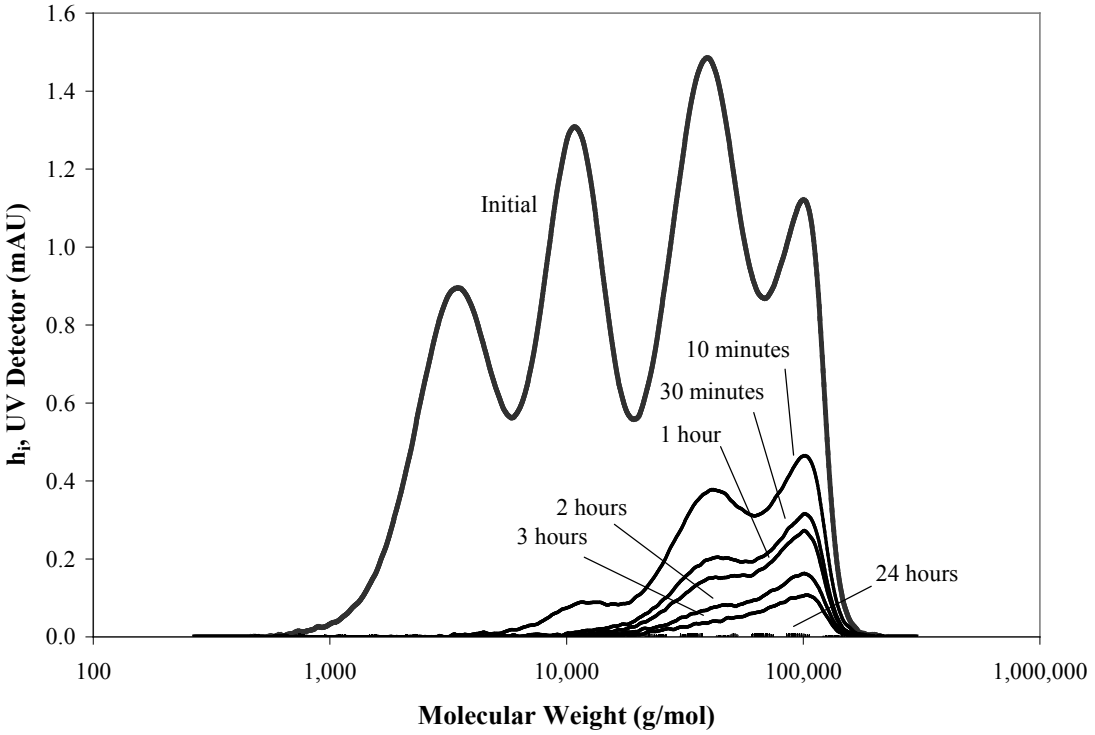

Figure 5.7 SEC spectra (UV detector) of solution phase PAA (mixture of four ATRP PAA samples) for the isotherm slurry with initial concentration at ~175 mg/L (shown as ◊ in Figure 5.6) as adsorption time increases. Area under the curves decreased steadily until reaching essentially zero at 24 hours of adsorption where nearly all PAA in the system was adsorbed.

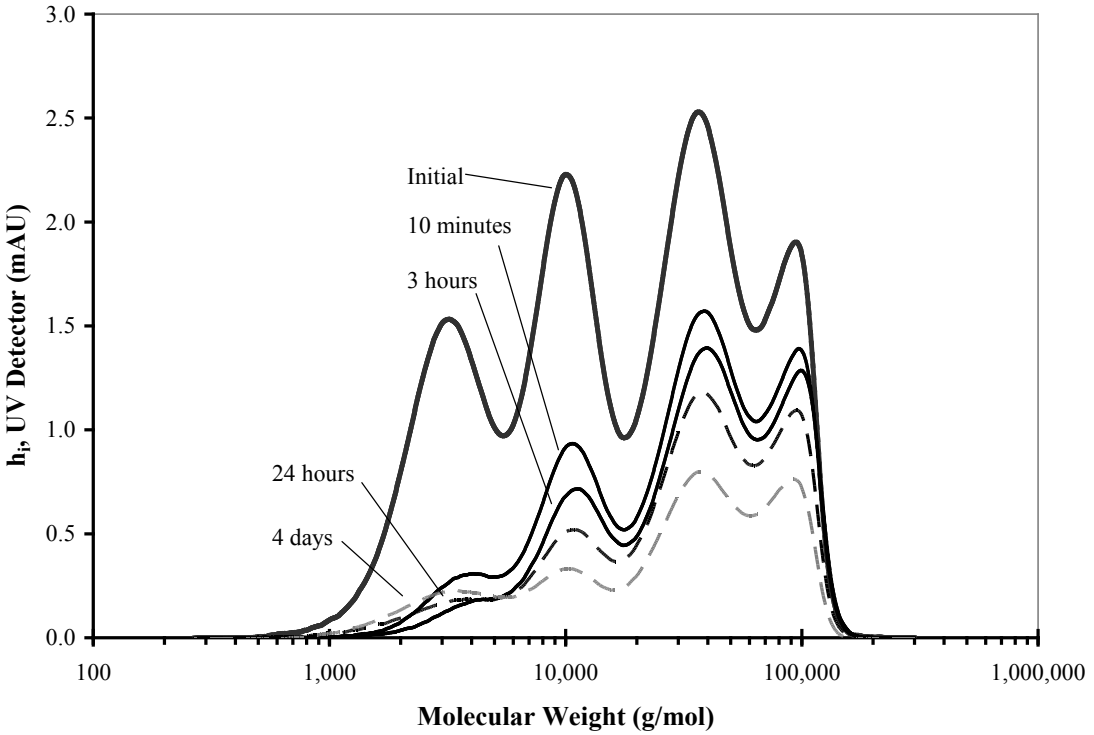

Figure 5.8 SEC spectra (UV detector) of solution phase PAA (mixture of four ATRP PAA samples) for the isotherm slurry with initial concentration at ~300 mg/L (shown as ◊ in Figure 5.6) as adsorption time increases. Spectra with adsorption times longer than 3 hours are shown as dashed lines and express an increase of low MW fractions with adsorption time.

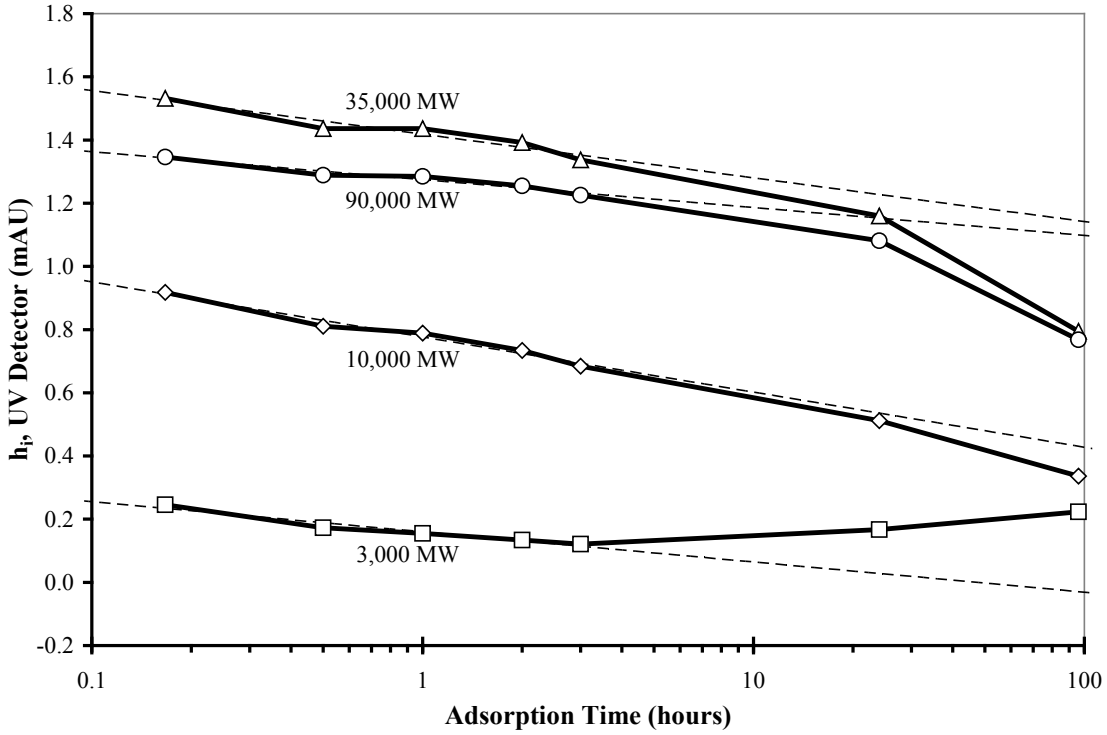

Figure 5.9 Relative solution concentrations of the four major mass fractions with respect to adsorption time. Logarithmic fits for points up to 3 hours are shown as dashed lines.

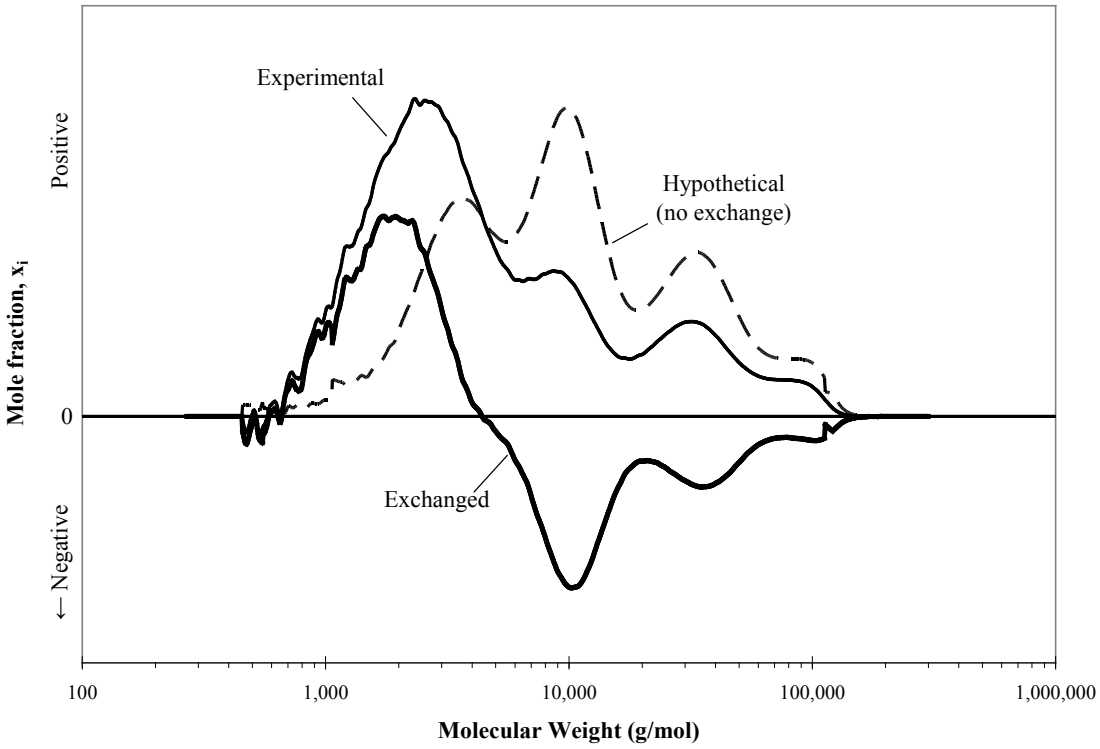

Figure 5.10 The relative PAA molecules in solution after 4 days (96 hours) of adsorption according to experimental data (thin line) and theoretical extrapolation (dashed line) based on initial 3 hours. The number of molecules active in the exchange process is then shown as the difference between the two (thick solid line). The positive and negative areas between the exchanged amounts and the x-axis are nearly equal.

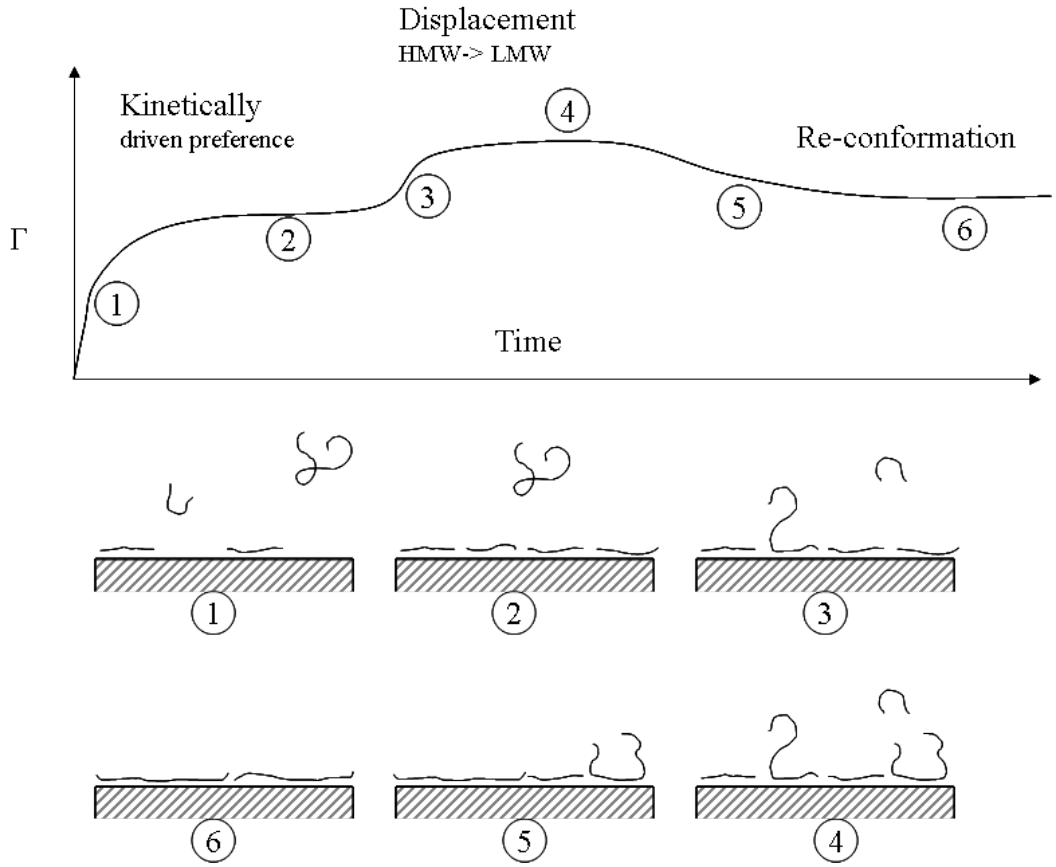

Figure 5.11 Schematic representation of PAA adsorption and conformation at the pH 12 calcite surface.

Chapter 6 - Inhibition of $CaCO_3$ Formation by Monodisperse PAA

Introduction

The previous chapters have led to a number of conclusions involving the molecular weight effects of PAA upon $CaCO_3$ inhibition. In Chapter 2, a myriad of commercial polymeric antiscalants already in use by kraft mills were analyzed and tested for their dose-performance efficiencies with regard to inhibiting $CaCO_3$ deposit formation and growth in kraft digester conditions. It was clear that the molecular weight of the polymers played a role in inhibition among other factors. In Chapter 3, inhibition experiments in a slightly less caustic environment and at more moderate temperatures were employed to investigate the mechanistic differences between PAA samples with MWs above and below M_w of ~20,000 g/mol. Although differences in inhibition efficacy were observed, the polydisperse nature of the commercial PAA/Na-PAA samples maintained some ambiguity of distinct inhibition mechanisms between the different MW ranges due to the presence of such a broad distribution of MW species in the individual polymer samples. This ambiguity fueled the need for a more monodispersed sample set than is commercially available and led to the successful synthesis of low PDI PAA samples via the hydrolysis of ATRP PtBA in Chapter 4. These low PDI samples were used alongside low molecular weight (LMW) low PDI RAFT polymerized Na-PAA and the polydisperse PAA/Na-PAA samples to investigate the isolated mechanism of PAA adsorption onto static calcite surfaces in pH 12 solution in the previous chapter (Ch. 5). Although neither adsorption quantities nor rates were found to conclusively differ with changes in the MW of the adsorbing species, a clear preference for LMW species and a flat conformation was exhibited with initial adsorption. Additionally, the dynamic nature of the PAA adsorbed layer was expressed as the adsorbed LMW species were replaced with HMW PAA molecules.

In an effort to understand how the dynamic nature of the adsorbed PAA influences the inhibitory effects of various MW PAA samples, the experimental method used in Chapter 3 was upgraded in a number of ways. First, the low PDI samples described in Chapters 4

and 5 were implemented in order to decrease the ambiguity of inhibitory efficacies between the low and high molecular weight PAA species. Second, the FBRM results monitoring the chord length distributions (CLDs) of particles both in solution and at the surfaces were compared to an additional analysis tool responsible for monitoring the $CaCO_3$ deposits present only at the system's surfaces, namely a quartz crystal microbalance (QCM) submerged in the solution alongside the FBRM probe. Third, the solution phase composition responsible for the nucleation and growth of the precipitated $CaCO_3$ was monitored to determine both the free Ca^{2+} cations in solution (via an ion selective electrode) and PAA MW concentrations and distributions (via SEC). In addition, the growth and morphology of precipitated crystals were also investigated using SEM for analysis of differing crystal habits during growth.

The interactions between polyelectrolytes and insoluble mineral crystal deposits have long been of interest to investigators across many scientific fields including biology, chemistry, and material scientists. In nature, all invertebrate organisms rely on the interplay between polyelectrolytes and hydroxyl apatite simply for strong bone structure while material scientists try to mimic the composite structure of some mollusks' nacre (proteins and aragonite $CaCO_3$ in a "brick and mortar" configuration) in order to also duplicate its tremendous strength to weight ratio.

As mentioned in the Introduction (Ch. 1), there lies a synergistic tie between antiscalant and biomineralization research. This relationship becomes more evident in this chapter as the mechanisms of scale inhibition are investigated in more depth. Of particular importance to biomineralization (of $CaCO_3$) is the transient precursor stage where the crystals lack order. The importance of the amorphous calcium carbonate (ACC) phase upon structured and controlled deposits of the other, more stable, polymorphs of $CaCO_3$ such as calcite and aragonite has been documented numerous times in particular with its relationship to biomineralization.[28, 99, 100] The ACC is slightly more soluble in water than the more stable polymorphs of $CaCO_3$ but is not as energetically stable, thus it requires a stabilizing agent in order to remain in existence and not transform into calcite or vaterite. In biomineralization processes, the ACC phase

typically remains as small (on the order of 500 nm) stabilized colloidal particles and acts as a precursor to the growth of specific crystals with a specific morphology and even crystal habit.[28, 29] A wide variety of polyelectrolytes (often in the form of proteins or polysaccharides) are used by various organisms in order to both stabilize the ACC phase and aid in its transformation into any of the three most stable $CaCO_3$ polymorphs. The effects of polyelectrolytes on stabilizing the ACC phase has been documented heavily[101-103] with PAA particularly in a few isolated cases[13, 99, 100] although the mechanisms involved are still unclear.[104] The use of numerous methods to monitor the different components of the crystallization systems in this chapter will be useful for not only elucidating the mechanisms of scale inhibition but also in adding to the knowledge upon which biomineralization can draw.

Materials and Methods

Chemicals and Materials

Inorganic materials including anhydrous Na_2CO (CAS #497-19-8), NaOH (50% $^{w}/_{w}$ CAS #1310-73-2), anhydrous $CaCl_2$ (CAS #10043-52-4), and HCl (CAS #7647-01-0) were purchased from Sigma-Aldrich (St. Louis, MO) as reagent grade chemicals. Poly(acrylic acid) and its neutralized salt form, sodium polyacrylate, were purchased from Polysciences Incorporated (Warrington, PA) as solutions with concentrations ranging from 20 to 63% $^{w}/_{w}$. Low PDI PAA samples were synthesized as outlined in Chapter 4.

Solutions

The initial solutions were prepared as 1 g/L Na_2CO_3 (9.4 mM CO_3^{2-}), 1 g/L NaOH (25 mM, pH 12), and varying concentrations of polymer additives from 1 to 50 mg/L (ppm active acids). The calcium solution used was prepared from $CaCl_2$ to produce a concentration of 1 g/L Ca^{2+} (2.77 g/L $CaCl_2$, 25 mM Ca^{2+}). All solutions were prepared using 18 MΩ "doubly" de-ionized water (DDI H_2O).

Experimental setup

500 mL of the initial solution was added to an 800 mL beaker and the various probes were submerged while stirring was commenced at 400 rpm via an overhead stirrer. The calcium solution was dripped into the stirred solution at 0.6 mL/min via a 7550-90 Masterflex (Cole-Parmer Instrument Company, Vernon Hills, IL) peristaltic pump. Chord length distributions of $CaCO_3$ particles were gathered using focused beam reflectance measurement (FBRM). A Lasentec D600L (Mettler-Toledo Inc., Columbus, OH) FBRM probe and hardware were used to collect all chord length distribution data (0–100 μm in 200 linear channels) until the total sum of chord length counts was at least 2000. A quartz crystal microbalance (as described below) was used to monitor in-situ crystal growth on surfaces. Calcium ions in solution were monitored using a Thermo Orion (Cummings, MA) IonPlus Calcium Ion Selective Electrode. PAA solution concentrations and MWDs were collected using Agilent (Santa Clara, CA) 1200 Series HPLC with a UV-detector (λ = 215 nm) employing two Waters (Milford, MA) 250 & 120 Ultrahydrogel columns in series with a 0.3 M NaCl, 0.1 M NaH_2PO_4 eluent buffered solution (pH 7.0) pumped at 0.85 mL/min. A series of eight Na-PAA standards from Polymer Laboratories, Inc. (Amherst, MA) with molecular weights ranging from 1,250 to 323,000 g/mol were used to calibrate the system with all MWs being relative to these standards. Samples were prepared by mixing filtered colloid suspension with thrice its volume of 4× concentrated eluent (1.2 M NaCl, 0.4 M NaH_2PO_4) buffered to pH 4.5 in order to prevent any precipitation of $CaCO_3$ in the columns. Scanning electron microscope (SEM) images were collected (using a nominal accelerating voltage of 5 kV and an initial working distance of 8 mm) on a JEOL (Tokyo, Japan) 6500 Field Emission Gun – Scanning Electron Microscope. Crystal samples for SEM were collected during the crystallization experiments by removing and preparing the filter membrane of the 0.45 μm PTFE syringe filter used to separate the suspension into an SEM sample.

Since commercial QCM instruments are rarely dynamic in terms of their modularity and are typically designed to meet the needs of the coating and etching industries, a modular QCM instrument was built. Shown in Figure 6.1 is the general schematic used for the modular QCM system. The center component of the system was the oscillator

circuit which was responsible for finding the resonant frequency and maintaining the oscillation of the crystal. Either an oscillator based on the analog NTE (Bloomfield, NJ) NTE927 differential video amplifier (rather than a digital IC amplifier used in most commercial QCM systems) or a Maxtek PLO-10i phase lock oscillator from Inficon (Syracuse, NY) was used. An Agilent (Santa Clara, CA) 53131A dual channel frequency counter which had the capability to monitor two oscillator circuits simultaneously was used for the frequency counter component. The interface between the computer and the counter allowing for data acquisition relied on the IEEE-488 standard (also commonly known as General Purpose Interface Bus or GPIB) with an Agilent 82357A USB/GPIB interface used for connecting to Agilent I/O Control computer software. This setup allowed for the addition of other possible components which could enhance the amounts of data recorded. For instance, an Agilent 34401A digital multimeter was commonly added for monitoring (and recording) the crystal resistance using the phase lock oscillator. Other options, although not employed here, could be such measurement tools as an impedance analyzer. These "optional" components are shown with dashed connections in Figure 6.1 to express the robustness and versatility of the modular-based setup.

Results & Discussion

Critical Ca^{2+} Determination & Analysis

The quartz crystal microbalance (QCM) is a robust and powerful measurement tool for monitoring the "in-situ" properties of thin films and coatings. Typical industrial uses include monitoring of thickness and rates of coatings via numerous methods in both the optics and semiconductor industries.[105, 106]

The two electrodes on an AT-cut quartz crystal induce transverse shear strain waves within the quartz via the converse piezoelectric effect as shown in Figure 6.2. A change in the characteristic resonance frequency of the crystal with the addition of a thin film can result in the determination of the thickness of the film, l_f, via the Sauerbrey equation[107] as shown in Equation 1.

$$l_f = -\frac{N_q \rho_q}{\rho_f} \frac{\Delta \nu}{\nu_q^{\,2}} \tag{1}$$

This "Sauerbrey thickness" uses the known constants of quartz: $N_q \equiv$ frequency constant for an AT cut quartz crystal (1.668×10^3 m/sec), $\rho_q \equiv$ density of quartz (8.83 g/cm^3), and $v_q \equiv$ resonant frequency of the unloaded crystal (~5 MHz) along with the known density of the added layer, ρ_f and the change in the resonant frequency of the crystal with the addition of the added thin film layer, Δv. Of course, the thickness value does not directly rely on the resonant frequency of the transverse shear wave, but rather its wavelength. Substituting inverse periods for the frequencies in Equation 1 then yields

$$l_f = \frac{N_q \rho_q}{\rho_f}\left(\tau - \tau_q\right) \tag{2}$$

where τ_q and τ represent the period of the resonant transverse shear wave of the crystal before and after the material composing the thin film is added. To improve accuracy, the commonly employed "Z-match" model,

$$l_f = \frac{N_q \rho_q}{\rho_f}\left(\frac{\tau}{\pi R_z}\right)\arctan\left[R_z \tan\left(\pi \frac{\tau - \tau_q}{\tau}\right)\right] \tag{3}$$

is used with R_z representing the ratio of the quartz and film material acoustic impedances. It should be noted here that although Equation 3 adds a useful complexity upon the logical addition of the acoustic property differences between the quartz and film material, Lu and Lewis point out that setting R_z equal to unity, and assuming no difference in material acoustic properties, only deviates the calculated l_f significantly from Equation 2 once the change in resonant frequency exceeds 0.5%.[108]

In order to investigate the differences between nucleation observed in solution and on surfaces, a quartz crystal microbalance (QCM) was used in addition to the FBRM as implemented in the experiments of Chapter 3. Since $CaCO_3$ growth was only allowed up

to frequency changes of at most 0.35%, Equation 2 was used to convert Δv into l_f values. This allowed for an adequately accurate surface thickness measurement without the timely (and costly) requirement of measuring the acoustic impedance of $CaCO_3$, not to mention investigating the change in transverse shear wave propagation in $CaCO_3$ with the addition of PAA to the matrix.

Figure 6.3 shows typical responses of both the QCM and FBRM probes with response to the increasing formal Ca^{2+} concentration. Similar to the critical Ca^{2+} concentration determination from the FBRM probe (as outlined in Chapter 3) the critical Ca^{2+} level was determined from the QCM response via the use of a somewhat arbitrary QCM thickness value of 5 $\mu g/cm^2$ as the threshold point. Therefore, the formal Ca^{2+} concentration where the QCM reading first reached 5 $\mu g/cm^2$ (denoted as the circle data point on the QCM curve) was used as the QCM determined critical Ca^{2+} concentration. For comparison purposes, the analogous FBRM determined critical Ca^{2+} concentration is also shown on the FBRM curve (secondary axis) of Figure 6.3.

The dose-performance curve shown in Figure 6.4 is a plot of both the FBRM and QCM determined critical Ca^{2+} concentrations using various initial concentrations of the 3,400 M_w PAA sample (synthesized in Chapter 4) as the $CaCO_3$ inhibitor. In this form, it becomes clear that the discrepancy between the FBRM and QCM determined critical Ca^{2+} concentrations, which was noticeable in Figure 6.3, does not become significant until the higher initial antiscalant concentrations were used. In addition, the efficacy of the low MW (and low PDI) PAA upon inhibition of $CaCO_3$ precipitation shows some obvious trends. First, the initial trend of critical Ca^{2+} concentration with respect to antiscalant concentration is linear. Second, at a critical polymer concentration near 10 ppm, the efficacy (slope of the dose-performance curve) changes suddenly. Third, at polymer concentrations above 10 ppm, the trend remains linear but shows different efficacies for inhibiting $CaCO_3$ when determined via the QCM compared to the FBRM measurements. These trends remained true for most of the low M_w (low PDI) polymers tested. Clearly, the PAA antiscalant inhibits nucleation and rapid growth differently depending upon its concentration in solution. Interestingly, in the higher concentration

regime, the inhibitor allows for surface nucleation (detected by QCM) much sooner than in the solution phase (as detected by FBRM). In the extreme case, such as for the low M_w PAA shown in Figure 6.4, the ability of the inhibitor to prevent surface nucleation has little to no dependence upon further addition of PAA (above the critical polymer concentration). Since the mechanism by which the FBRM detected nucleation in the low concentration regime of the dose-performance curves was by nucleation on the probe window (similarly as that outlined in Chapter 3), this suggests that the mechanism responsible for nucleation (on surfaces) and rapid growth in the lower concentration regime does not respond with increased inhibition upon the addition of PAA past the critical point. This suggests that nucleation in solution occurs (in the higher concentration regime) but only after surface nucleation has already begun (as noticed by the QCM).

Figure 6.5 shows the dose performance curves for some low M_w (low PDI) polymers side-by-side with the polydisperse ~20k M_w commercial Na-PAA sample. These samples, with M_w values below 10,000 g/mol, all showed the same trends as those outlined for Figure 6.4. In addition to having linear efficacy trends in polymer concentration regions below and above the critical point, the majority of the low concentration data points overlapped regardless of MW. Also, the range at which the critical polymer concentrations for the different MW polymers occurred was consistently 10 to 12 ppm.

Figure 6.6 shows the dose performance curves for some of the higher M_w ATRP PAA samples again with the polydisperse ~20k M_w commercial Na-PAA sample given for reference purposes. These samples, with M_w values all above 10,000 g/mol, still showed the two distinct regions with linear efficacies but with critical polymer concentrations being expressed in a lower 4 to 7.5 ppm range. In addition, all of these higher MW polymer samples yielded similar initial efficacies where an increase in 1 ppm of PAA resulted in the inhibition of an additional 0.22 mM Ca^{2+} from precipitating.

Summarizing the dose-performance curves over all the low PDI polymers examined, Figure 6.7 represents the change in the initial and secondary efficacies as determined via

FBRM (open □ and ◊ respectively) and QCM (closed ■ and ♦ respectively) with respect to the M_w of the polymer antiscalant used. It is clear that as the initial efficacies decrease with increasing MW until they plateau for the higher MWs, the secondary efficacies reach their maximum around a MW of 20,000 g/mol. Since the efficacies are plotted in terms of the stoichiometric ratio between the amount of Ca^{2+} inhibited and the number of carboxylic acid functional groups present in solution, it can be seen that the initial efficacies of the lower MW polymers surpass a molar ratio of 25 calcium cations per acid functional group of the polymer. Even in contrast to this, where the secondary efficacies at low MW polymer concentrations above the critical level yield molar ratios of ~2 Ca^{2+} per –COOH, the polymers are still maintaining calcium levels to a greater extent than a purely stoichiometric charge match resulting in an efficiency of ½ would suggest. This is clear evidence that strict chelation is not responsible for the inhibition of $CaCO_3$ with Na-PAA/PAA polymer antiscalants. It should be noted that although the trend is not shown here, the critical polymer concentration underwent a local maximum around a MW of 10,000 g/mol but stayed within the range of 4.2 to 12 ppm polymer for all MWs tested.

Post-nucleation Results & Discussion

Up until this point, the focus has been on the critical Ca^{2+} levels required to begin nucleation. Now, a look at the data after nucleation will lead to some additional insights into the interplay between the characteristics of the instruments and the mechanisms of the system. As most antiscalants will not inhibit the onset of nucleation entirely, it is important to note the effects that PAA/Na-PAA has on crystal growth as well as strictly on inhibition.

To begin with, the FBRM data from the low PDI polymer samples fell into the two categories outlined in Chapter 3, where FBRM determined Ca^{2+} concentrations were determined to either be a result of monitored $CaCO_3$ crystals dispersed in solution or upon the probe window. In addition to this, sudden changes in the overall crystal count and CLDs were expressed for many of the individual crystal growth experiments after nucleation began where initial PAA concentrations around the critical point were

employed. Figure 6.8 is one such plot showing numerous sudden changes in the CLD with respect to time as the stock 1 g/L calcium solution was dripped into the initially 500 mL carbonate and 10 ppm 75,000 M_w ATRP PAA solution. Although a single crystal on the FBRM probe was observed as expressed by the vertical dark streak, the remainder of the CLDs are under examination here. As can be seen, at discrete times, the monitored CLDs show sudden shifts towards larger particles with intensities remaining fairly constant between the shifts. Figure 6.9 shows the total FBRM particle count and QCM thickness measurement with respect to time. Here, the trend of sudden increased particle sizes as shown in the CLD shifts of Figure 6.8 is accompanied with an overall sudden decrease in the FBRM total crystal count in the solution phase. In addition, the QCM response suggests sudden increases in the mass of $CaCO_3$ present on the surface with little to no mass being added in between the brief periods of crystal growth. Combining the data from the two measurement techniques leads to the conclusion that after stable $CaCO_3$ is present in the system, crystal growth (both in solution and on the surfaces) is dormant until the Ca^{2+} and CO_3^{2-} solution reaches the upper limit of its metastable region upon the continual addition of Ca^{2+} and initiates growth again. This growth most likely occurs on the existing particles dispersed in the solution and causes at least some of them to adhere to the surfaces, being measured by the QCM, suggesting a transfer of existing particles from solution to the surface. This cycle between rapid growth and dormant crystals suggests that the saturation of the solution also cycles from the upper limit of its metastable region to the lower limit (saturation) respectively. To confirm this, the solution phase needs to be monitored along with the crystal growth methods.

Since FBRM and QCM both monitor the amount of $CaCO_3$ precipitated out from the supersaturated solution stabilized with polymer, information regarding the actual solution phase concentrations of calcium cations and PAA were desired in order to confirm and expand the results. In addition to the polymer concentration in solution throughout nucleation and crystal growth, the molecular weight distribution (MWD) of the portion of the polymer active in these two processes was sought after.

Figure 6.10 shows the dose-performance curves for 2 different mixtures of ATRP PAA samples. The first mixture uses 4 different ATRP samples ranging from 3,400 M_w to 75,000 M_w selected in order to mimic the polydispersity of the reference ~20k MW commercial Na-PAA sample (shown as thick gray line). The second mixture used only the two extreme ATRP PAA samples, namely the 3,400 and 75,000 M_w samples, mixed in a 50:50 mass ratio. Whereas both mixtures expressed a local maximum at the same 8 ppm polymer concentration as the reference polymer, the 50:50 mixture showed the most similarity to the commercial polydisperse sample. In an attempt to understand the total behavior of the system at the critical polymer concentration, numerous analysis techniques were implemented for a crystal growth experiment with 8 ppm 50:50 3,400:75,000 M_w ATRP PAA mixture with results shown side-by-side with respect to the formal concentration of Ca^{2+} which was added continuously in the form of a 1 g/L solution. In both Figures 6.11 and 6.12, the QCM thickness is shown plotted against the secondary ordinate for reference purposes expressing the sudden growth rates as described previously. Shown in Figure 6.11, the ion selective electrode (ISE) used to monitor the solution phase concentration of free calcium cations maintained a constant linear slope with the initial addition of calcium (as expected) but peaked and began decreasing before nucleation was detected by either the QCM or FBRM. It should be noted that this decrease in free Ca^{2+} concentration before nucleation of detectable crystals was accompanied with an increase in visually noticeable turbidity. Once nucleation occurred, and growth ensued rapidly (followed by a dormant stage), the free Ca^{2+} concentration began to rise again due to the added calcium and repeated this process of reaching a maximum and decreasing during the rapid crystal growth correlating with the QCM data. This alone confirms that the regions of sudden crystal growth suggested by the FBRM and QCM data were not some manifestation of just exchanges in crystal position within the system (crystals moving from the solution to the surfaces) but rather due to the oscillation in metastability of the Ca^{2+}, CO_3^{2-}, and PAA solution.

The most interesting portion of the solution phase data is represented in Figure 6.12 where the SEC derived polymer concentrations and MWDs are summarized. At discrete points during the crystal growth experiment, samples of the solution/slurry were collected

and filtered to analyze only the solution phase via SEC. Using the SEC spectra from before any calcium was added to the solution, the initial area under the SEC peaks was used as the reference for calculating the subsequent polymer concentrations in solution during the experiment (similar to the method used in Chapter 5 for the isotherm concentrations). The decrease in the total PAA concentration to less than 1 ppm suggests that the majority of the polymer escaped the solution phase by the end of the experiment (at 8.8 mM formal Ca^{2+} levels). The great advantage of using SEC to determine the PAA concentration lies in its ability to also give a complete MWD for each sample. Thus, the bimodal MWDs were de-convoluted and the concentration of each of the 3,400 and 75,000 M_w PAA components were calculated and are plotted in Figure 6.12 also. When the solution phase PAA concentrations are coupled with the QCM and ISE data, a few things become apparent. First, at the point where Ca^{2+}, as monitored via the ISE, begins to separate out from solution (also accompanied by the visually noticeable increase in turbidity) but before the QCM and FBRM detect nucleation, the PAA is also leaving the freedom of the solution. In contrast to the kinetics experiments of Chapter 5, the rates of adsorption appear to be quite different for the high and low MW PAA species, with the lower 3,400 M_w species leaving the solution phase almost twice as fast as the higher 75,000 M_w species. Although it should be mentioned that the term "adsorption" may be misplaced at this point seeing as there is no clear evidence that solid crystal phases have nucleated yet. Once nucleation and rapid growth do occur (as evidenced by the QCM data) and as growth of the $CaCO_3$ crystals diminishes, during the plateau regions of the QCM data, desorption (or at least a return to the solution phase) of the polymer molecules occurred. The first plateau expresses this trend most vividly with a substantial increase in the total amount of PAA in solution. Upon subsequent growth and plateau regions, the amount of PAA oscillation decreased. Monitoring the two different MW samples, it is suggestive that not only does the lower MW species adsorb faster than their higher MW counterparts, but they also desorb much faster, with the concentration of low MW PAA in the solution phase just before the second growth region being larger than the higher MW concentration. Ideally, in-situ adsorption information would be the most useful here, but the dynamic surface area of this system makes an accurate mass per unit area

difficult if not impossible to ascertain. A clear difference can be seen between the PAA and $CaCO_3$ interaction of a growing crystal and the interactions when the calcite has a relatively static surface (as in the isotherms of Chapter 5). There are two possible reasons for this discrepancy. The first, is that the adsorption/desorption kinetics vary significantly due to the addition of new Ca^{2+} and CO_3^{2-} ions to the surface along with polymer. The second is the possibility that the solid $CaCO_3$ phase observed in these growth experiments is not entirely calcite.

In addition to the numerous methods of monitoring $CaCO_3$ particle growth and interactions with PAA shown in Figures 6.11 and 6.12, SEM images were also taken of the crystals present at various times throughout the experiment and shown in Figure 6.13. As can be seen through the succession of $CaCO_3$ particles as they grow in the presence of the two part mixture of PAA, the particle size increases with time. The morphology, however, changes slightly as the system moves through multiple growth and plateau stages. Upon the initial growth stage (as expressed by the QCM data), Figure 6.13-A shows typical ~3 μm long peanut shaped crystals. However, the surfaces of the crystals were extremely porous with individual surface edges of the protrusions suggesting a slight misalignment of their crystallographic directions similar to those expressed in the SEM images of Chapter 3. As growth ensued and plateaued, the crystals grew to ~6 μm and expressed much smoother surfaces with channels and cracks replacing the pores of image A. Flat crystallographic faces were only vaguely observable at the ends and in the center of the oblong ellipsoidal-shaped crystals. After the second growth and plateau region, the crystal structures shown in Figure 6.13-C confirm the conclusion of separate growth stages within the system as the crystals express separate growths upon the existing ellipsoidal shape. The majority of crystals showed growth only on the ends of the existing peanuts yielding a "capped" appearance. In some cases, new nucleation began (and remained) at the center of the peanut. The strong correlation between the flat faces being only present at the tips and center of the peanuts of image B and the new growth only nucleating at those same spots in image C suggests that the stabilized calcite {100} faces with maximum growth rates in the $\langle \bar{1}\,11 \rangle$ directions are the first also to

nucleate new growth. As growth continues past the second plateau, as shown in Figure 6.13-D, the crystals grow in size through agglomeration and continual growth of the "caps" shown in image C.

From the SEM images, it is clear that the precipitated $CaCO_3$ nucleates and then continues to grow via deposits on existing crystals. This process of multiple stages of rapid $CaCO_3$ deposition separated by periods of little to no precipitation is confirmed with the oscillation of free Ca^{2+} levels as monitored via the ISE probe. There is, however, an extended period before the first rapid growth stage where the free Ca^{2+} concentration in solution decreases despite the continual addition of calcium cations being pumped into solution. This period is often accompanied with a substantial increase in the visually noticeable turbidity level of the solution. Clearly, a separate phase is being generated in solution which encompasses the Ca^{2+} but does not show up as a deposit in either the QCM or FBRM data. In addition to this separate phase encompassing calcium cations, it also removes PAA mass from the solution phase. The concentration of PAA in the solution for the two MWs is also shown in Figure 6.12 and suggests that this separate phase has a preference for the lower MW (3,400 M_w) over the higher MW.

In order to present a reasonable and unified explanation for the inhibition (and controlled growth) mechanisms of PAA with respect to $CaCO_3$ deposits, it may be useful to mention a number of key components from the biomineralization and crystal growth literature. Thus, an explanation can be offered if the initial phase before nucleation and rapid growth, which was just shown to comprise of at least Ca^{2+} and PAA and to be responsible for the visual increase in turbidity, is *not* a precursor (in the strictest sense) for the calcite crystals which form the stable precipitates measured via both QCM and FBRM. At this point it would be wise to make a distinction between terms. It has been mentioned numerous times throughout the literature that amorphous calcium carbonate (ACC) is a precursor for calcite and the other more stable $CaCO_3$ polymorphs in the realms of stabilization, biomineralization, and even antiscalants, but no instruments available today can prove that a single crystal of ACC (stabilized in water) transforms

directly into one of the more structured polymorphs. With this in mind, the term "precursor" will be used here to define ACC when its phase is simply noticeable in the solution before the more stable calcite phase is noticed. When describing the more explicit case where an ACC crystal (or globule) morphs into calcite (*without* re-dissolving first) the ACC will be referred to as a "strict precursor" to calcite formation. The idea that ACC does not always directly transform into calcite (or aragonite or vaterite) has been mentioned in the literature by Addadi *et al*. who distinguishes the difference between the transient anhydrous ACC phase and a precursor ACC phase. The transient phase is described as the ACC which is directly transformed into another more stable polymorph of $CaCO_3$. In contrast, a precursor (or more explicitly, a strict precursor) is the hydrated form of ACC observed before a more stable polymorph is observed. In addition to the distinction made by Addadi *et al*., Mann points out that transformations *must* proceed by dissolution.[28, 29]

With this distinction emphasized, the explanation begins to solidify rather quickly, explaining a number of previously mentioned phenomena which appear contrary to a simple polymer adsorption mechanism being responsible for inhibition behavior. For example, the adsorption results of Chapter 5, showing adsorption onto calcite being essentially independent of the MW of the PAA with only a small competitive effect, are in direct contrast to the clear dependence of MW upon $CaCO_3$ inhibition shown here and earlier, in Chapters 2 and 3. The existence (and importance) of a PAA stabilized amorphous calcium carbonate phase (ACC/PAA) explains how the MW independent nature of PAA adsorption onto calcite can result in a MW dependent $CaCO_3$ inhibition performance of PAA.

As depicted in Figure 6.14, the first phase formed, ACC/PAA, is the least stable but also possesses the smallest energy barrier to formation. Without a stabilizer, the presence of ACC is short lived if it is even ever present at all in the slurry. With an additive such as PAA, ACC can remain in solution for prolonged periods being stabilized by the polymer.[99] In the present system, two things should be mentioned about this initial ACC/PAA phase. First, the ACC/PAA particles remain small enough that they are

neither detectable by the FBRM optics nor deposited upon the surface of the QCM crystal. However, the presence of this phase is supported by the clear removal of both Ca^{2+} and PAA from the solution phase. Secondly, the tendency for the smaller (3,400 M_w) PAA species to stabilize the ACC is over twice that of the higher (75,000 M_w) PAA species present in solution. It should be mentioned here that the increasing ratio between the calcium and PAA –COOH functional groups (Ca:COOH) in the ACC/PAA phase (measured by subtracting the amounts measured in solution from the calculated formal amounts) is supportive of Mann's recognition that ACC is accomplished during biomineralization by encapsulating it "in an impermeable organic sheath."[29] In the present system, the amount of PAA (relative to calcium) stabilizing the ACC phase decreases as particles gets larger and their surface area to volume ratio decreases.

The second phase formed, calcite, has a limited (if any) correlation to the first ACC phase but it is the phase which triggers the detection of nucleation via both FBRM and QCM methods. The ACC/PAA may be a precursor but it is not a strict precursor to the calcite. The only effect the ACC/PAA phase has on the forming calcite (and the system as a whole) is the decrease in PAA inhibitor concentration in the remaining solution phase as a result of ACC formation and stabilization. Thus, once the solution phase concentration of PAA decreases (via removal to the ACC/PAA phase) to a point where it can no longer inhibit calcite growth (especially since the more effective LMW species are missing from solution), the system is vulnerable to nucleation and growth of the calcite phase. Since this calcite phase is more stable and energetically favorable, nearly all of the calcium in the system is transported to its surfaces to be included in the growing crystals.

Once the calcite phase has nucleated and grows, it is in constant equilibrium with the Ca^{2+} in solution. Since the ACC/PAA is also in equilibrium with the solution Ca^{2+}, there is a subsequent mass transfer of Ca^{2+} from the highly soluble ACC/PAA particles to the calcite particles. This type of mass transfer resembles the growth of mollusk nacre where the aragonite crystals grow at the expense of the ACC phase[109] and supports the proposed ACC phase diagram of Faatz *et al*. where they suggest that "the amorphous material may

also serve as a reservoir from which crystalline material can evolve."[104] The relative proximity of the two different phases has not been established, but it is clear that as the calcium of the ACC/PAA is redistributed, the PAA that was originally stabilizing the ACC is re-dissolved and finds itself back in the solution phase. This is evidenced in Figure 6.12 by the increase in the solution phase PAA after the calcite phase has stopped its initial growth stage. Once the calcite phase, with adsorbed PAA, has consumed enough Ca^{2+} from the solution phase (exhausting the "reserves" from the ACC/PAA in the process), crystal growth stops. Or more likely, the amount of calcite surface coverage by the PAA increases as the rate of Ca^{2+} diminishes, leaving a saturated surface once growth stops. At this point, the calcite phase is essentially isolated from the solution phase via the adsorbed PAA and does not allow additional Ca^{2+} to be added to the surface. The solution phase is essentially the same as before ACC originally formed albeit with a lower concentration of PAA. More explicitly, the Ca^{2+} levels are just at saturation, with PAA concentrations being returned to initial conditions (as before the ACC was nucleated) minus whatever polymer has adsorbed to the calcite. This cycle of forming stabilized ACC/PAA until Ca^{2+}:PAA conditions are once again suitable for calcite growth is repeated throughout the duration of the crystal growth experiments. The overall decrease in solution phase PAA is evidenced in Figure 6.12 when sampled between ACC → calcite cycles. Also, it is apparent from the noticeable decrease in the solution phase Ca^{2+} levels immediately after the calcite growth stops (peaks of the local maxima as measured via the ISE probe continually decrease) in Figure 6.11 with continuing cycles. Such a decrease confirms that the solution phase has a decreasing effective supersaturation (metastable) limit which correlates with the knowledge that there is less PAA available in the solution phase as an inhibitor with each cycle of calcite growth.

In terms of the performance of an antiscalant, the stabilized ACC/PAA phase is relatively harmless in comparison to the calcite phase which settles quickly and is also found on the QCM and FBRM surfaces. Since the main objective of using an antiscalant in the kraft digestion and chemical recovery cycle is to keep the heat transfer surfaces free from deposited $CaCO_3$ and its insulating properties, the most advantageous property

of any antiscalant is to increase the critical supersaturation point at which this unstable calcite phase finds its way to the surfaces of the system.

Conclusions

The low PDI PAA samples synthesized in Chapter 4 were used to isolate the inhibition effects of the specific MW species. Although all of the samples expressed a sudden change in their inhibition efficacy at around 8 ppm, it was shown that MW species below 10,000 M_w performed much better at low concentrations. In contrast, the MW species above 10,000 M_w performed more poorly at concentrations below their change in efficacy with their secondary efficacies (at higher concentrations) being higher than their lower MW counterparts. The combination of these two trends explains the general trends of the polydisperse (commercial) PAA/Na-PAA dose-performance curves of Chapter 3.

Nucleation and growth experiments involving mixtures of the low PDI samples were conducted in order to elucidate the mechanisms responsible for the two different efficacies and the local maxima present in the dose-performance curves. ISE, SEC, and SEM were utilized in addition to the QCM and FBRM probes in order to track the concentrations of the PAA and Ca^{2+} along with the crystal habits. It was proposed that the precipitated calcite crystals responsible for the common definition of "scale" were preceded by a PAA stabilized ACC phase which also removed both Ca^{2+} and PAA from the solution. Once the solution conditions became low enough in PAA, calcite crystals nucleated and grew at the expense of the ACC/PAA phase. It is this ACC/PAA precursor phase that should be the focus of future polymeric antiscalant development as its stability is the key component in extending the greater initial efficacy of the dose-performance curves. In particular, the greater initial efficacy of the lower MW PAAs is of utmost importance to this concept as they also exhibit a greater tendency towards this precursor phase. Building upon this proposed explanation, the ideal antiscalant would not only stabilize a large amount of ACC but also leave species behind in solution that are tailored for inhibiting calcite nucleation and growth.

Figures

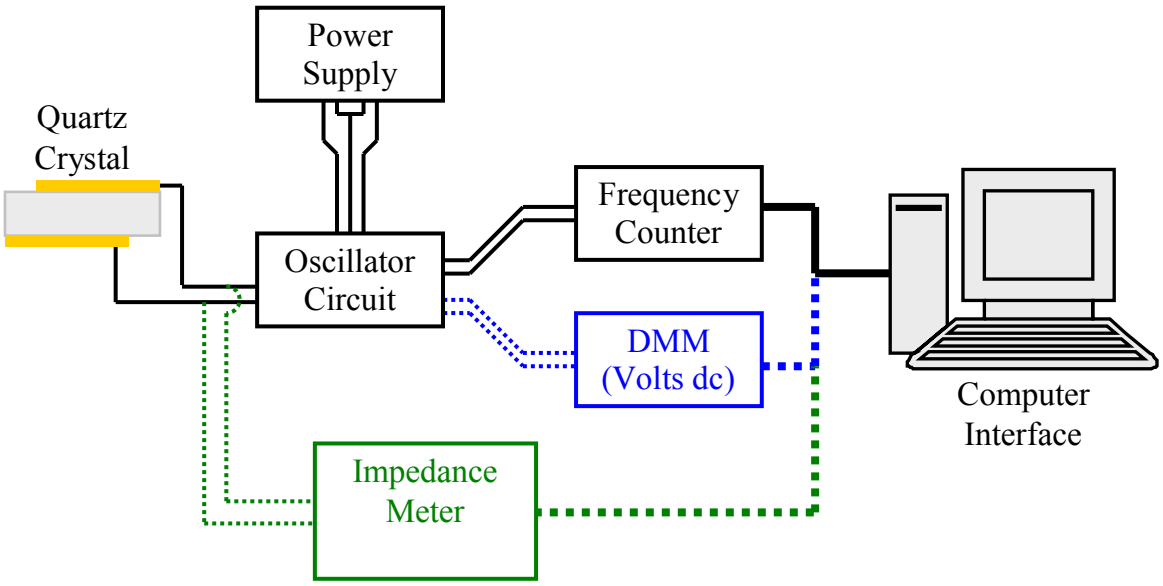

Figure 6.1 Schematic of modular quartz crystal microbalance (QCM) system built. An AT-cut quartz crystal is used as the frequency determining component for an externally powered oscillator circuit. The frequency counter, digital multimeter (DMM), and impedance meter are used to monitor oscillator circuit and output data to computer over GPIB interface (shown as thick connections). Dotted lines denote optional component connections.

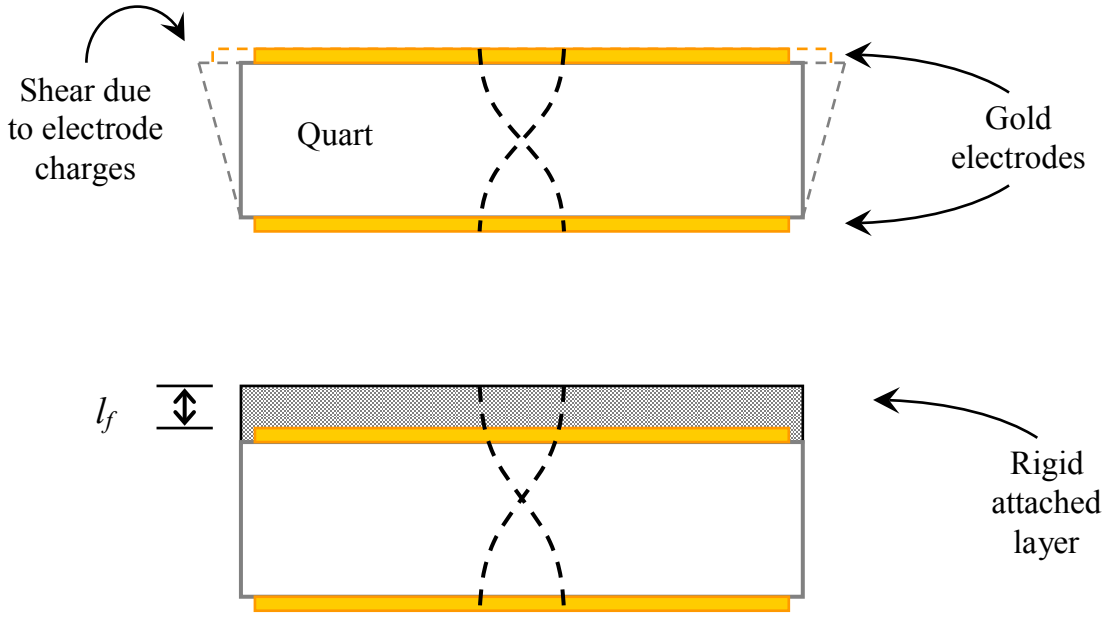

Figure 6.2 Diagram of quartz crystal microbalance (QCM) mechanism. Dashed lines through the center of the crystals express the transverse shear wave propagation due to alternating charge between gold electrodes (top). An increase in (resonance) wavelength as the thickness of the (rigid) attached layer, l_f, expands the effective boundary of the entire crystal yields a decrease in the monitored resonant frequency (bottom).

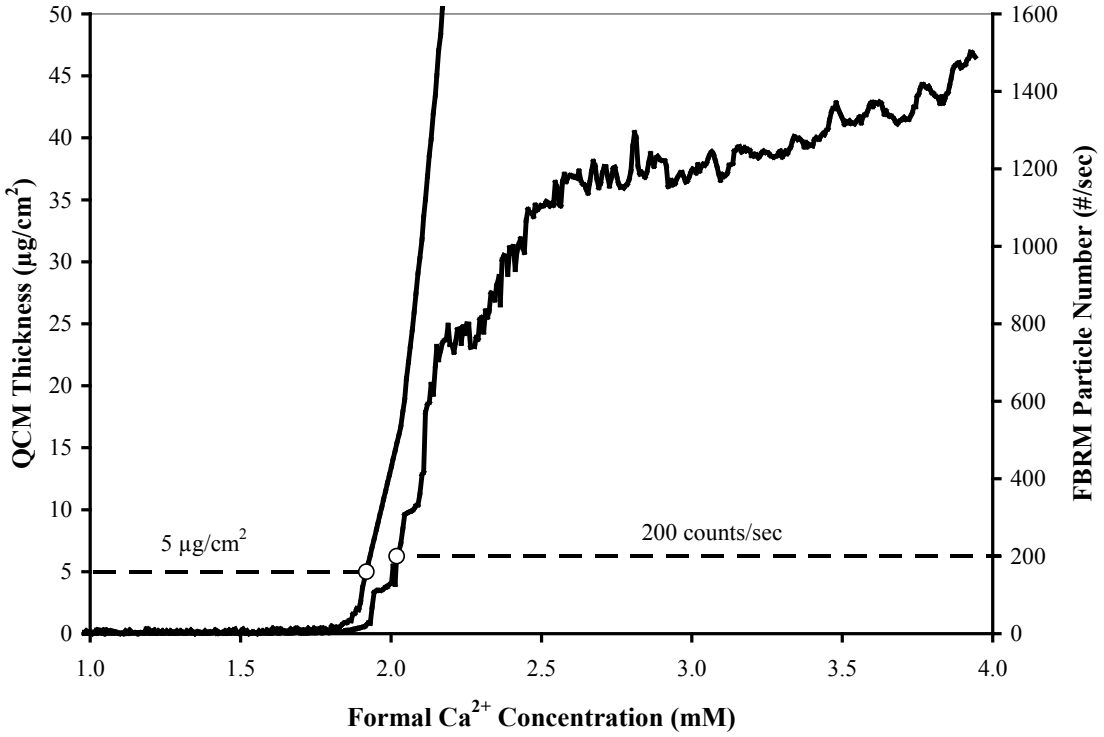

Figure 6.3 A typical plot of $CaCO_3$ growth on the Au coated QCM crystal (primary axis) and particle count as monitored by FBRM (secondary axis) with respect to the formal calcium concentration of the solution. 1000 mg/L Ca^{2+} solution was pumped at a rate of 0.6 mL/min into 500 mL of a 1 g/L Na_2CO_3 solution at pH 12 and 25 °C. The open circles (○) denote the points at which the $CaCO_3$ growth on the QCM reached 5 µm/cm^2 or the particle count reached 200 counts per second (dashed lines) and hence where the critical calcium level was determined to be via each method.

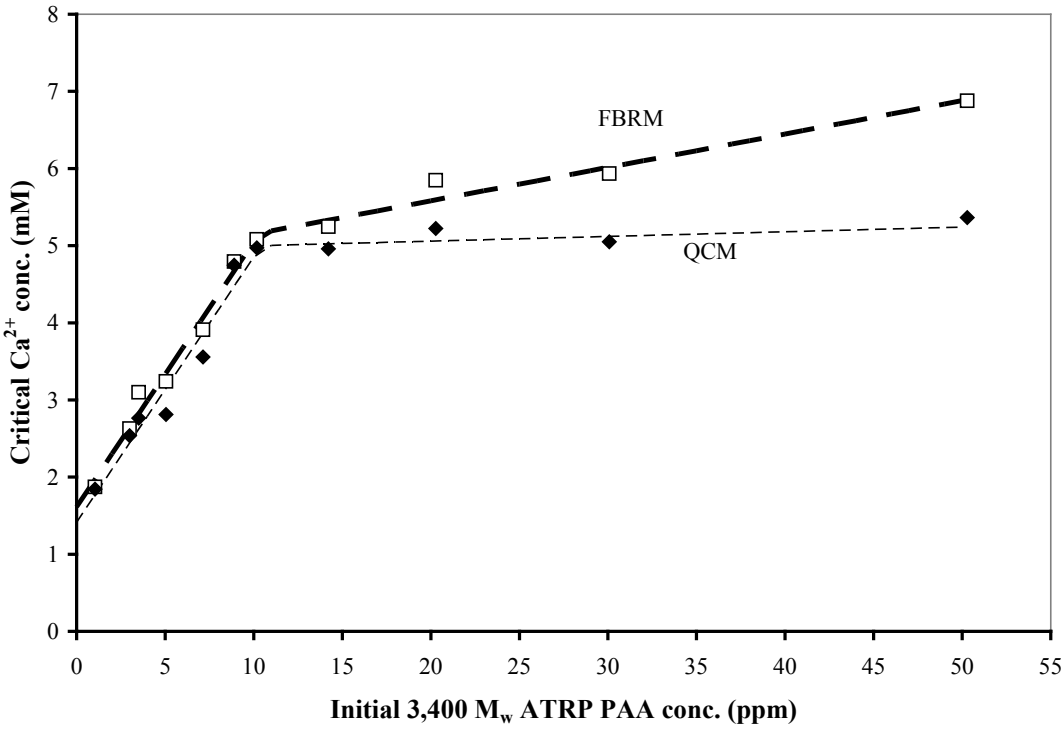

Figure 6.4 $CaCO_3$ scale inhibition performance curves for varying initial concentrations of 3,400 M_w ATRP PAA via FBRM (□) and QCM (♦) monitoring techniques. Dashed lines represent the change in the linear fitting of data points around ~10 ppm.

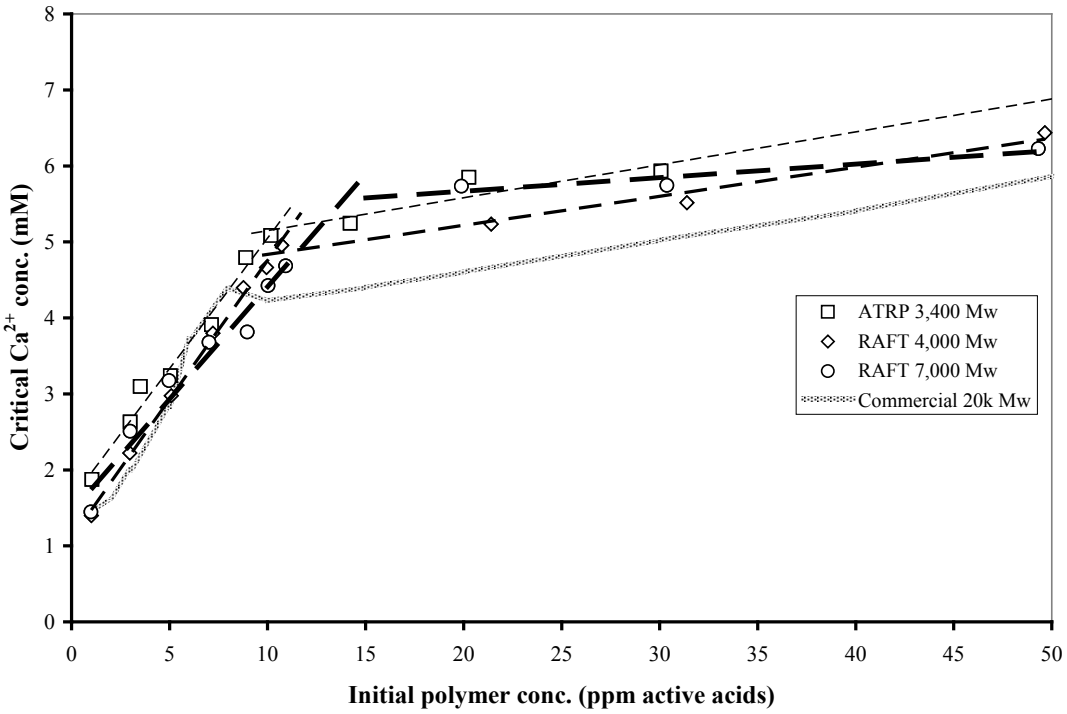

Figure 6.5 Critical calcium levels (as determined via FBRM) relative to the initial polymer concentration for the lower MW PAA and Na-PAA low PDI samples. 3,400 M_w ATRP PAA (□), 4,000 and 7,000 M_w RAFT Na-PAA sample (◊ and ○ respectively) are shown with the commercial 20k M_w Na-PAA (solid gray line) for reference. Linear regression fits of concentrations below and above ~10 ppm are shown as dashed lines.

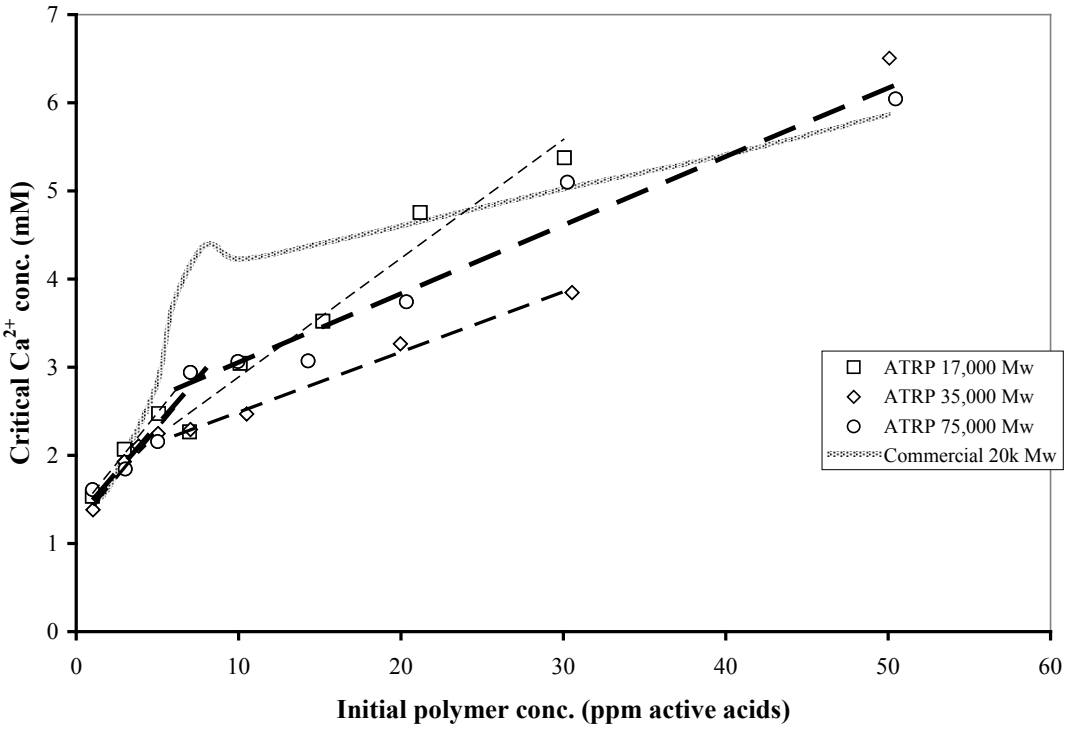

Figure 6.6 Critical calcium levels (as determined via FBRM) relative to the initial polymer concentration for the higher MW ATRP PAA (low PDI) samples. 17,000 M_w (□), 35,000 M_w (◊), and 75,000 M_w (○) are shown with the commercial 20k M_w Na-PAA (solid gray line) for reference. Linear regression fits of concentrations below and above ~8 ppm are shown as dashed lines.

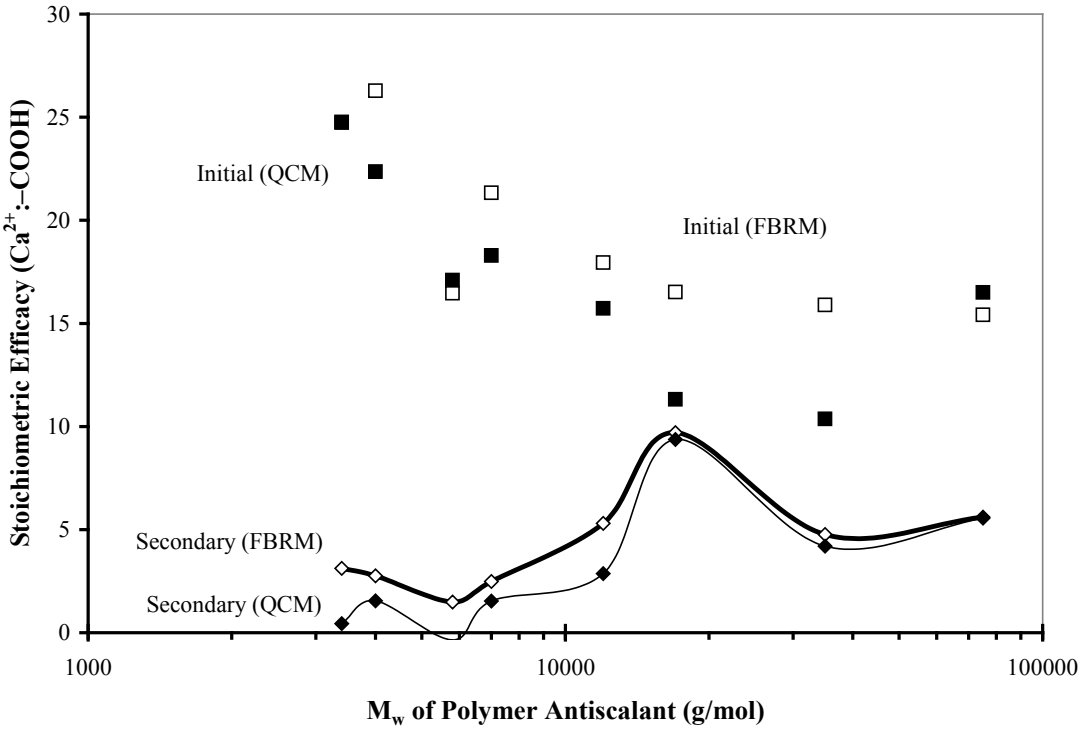

Figure 6.7 Efficacies of the various low PDI PAA/Na-PAA antiscalants. Initial and secondary slopes (□ and ◊ respectively) of Figures 6.4 and 6.5 converted into the moles of $CaCO_3$ inhibited per additional mole of carboxylic acid group added in the form of varying MW PAA/Na-PAA samples are plotted versus the polymer MW. Corresponding initial and secondary slopes as determined via QCM are shown as solid symbols (■ and ♦ respectively).

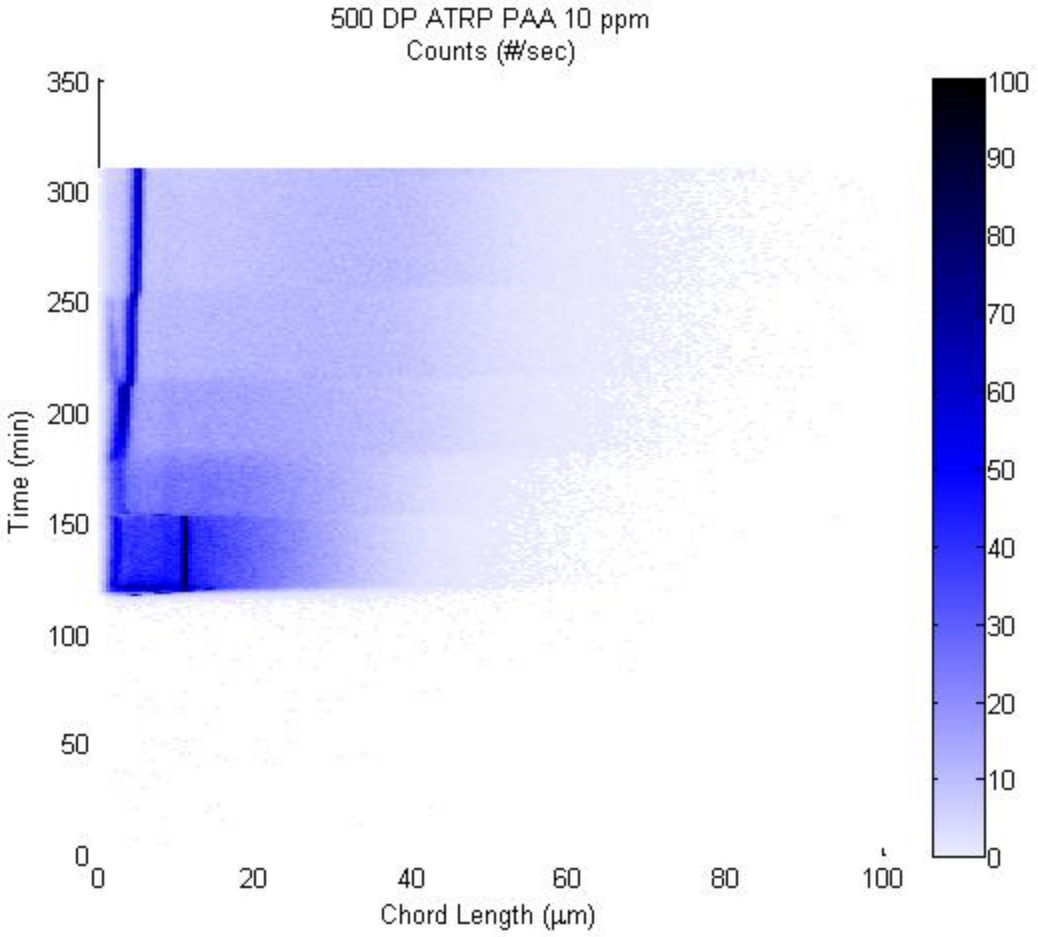

Figure 6.8 FBRM collected CLDs during crystallization experiment using 75,000 M_w ATRP PAA at 10 ppm as inhibitor. The slight changes in chord length counts across all chord lengths suggest sudden growth of crystals suspended in solution.

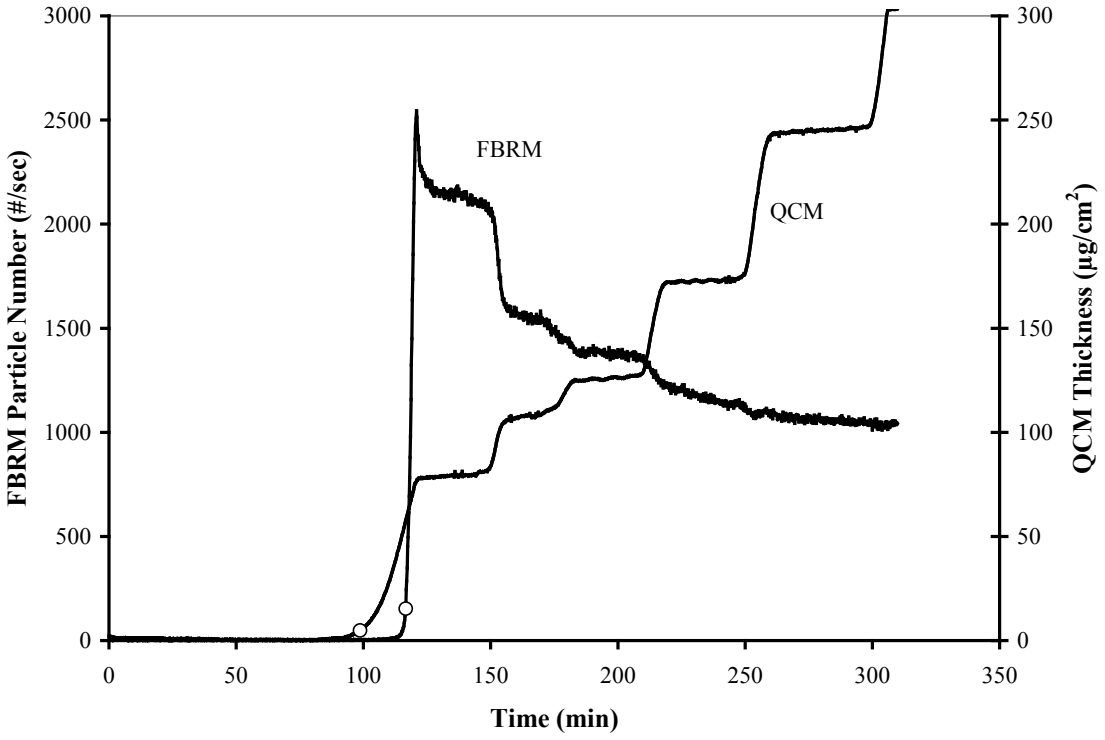

Figure 6.9 The FBRM total chord length counts/sec (primary ordinate) and QCM thickness (secondary ordinate) during crystallization experiment using 75,000 M_w ATRP PAA at 10 ppm as inhibitor, correlating to Figure 6.7 expressing sudden crystal growth on surfaces alongside decreases in particle numbers suspended in solution. Open circles (○) on plots denote the point at which nucleation was defined for each respective instrument.

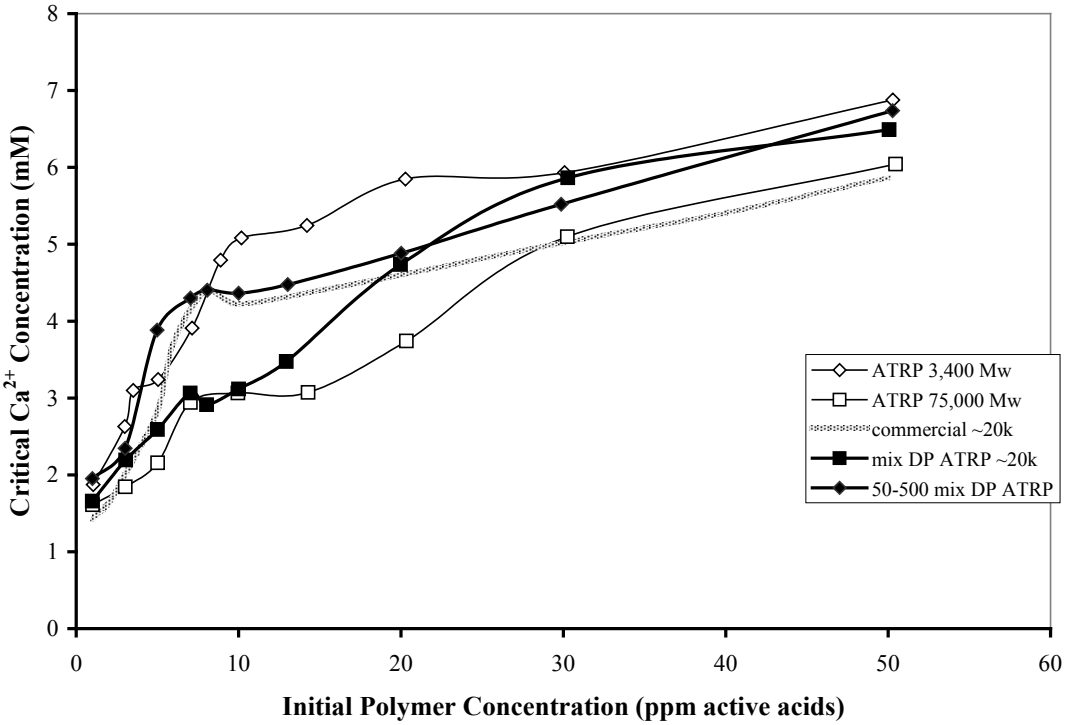

Figure 6.10 Dose-performance curves for ATRP PAA mixtures, their components, and the referenced commercial ~20k Na-PAA sample.

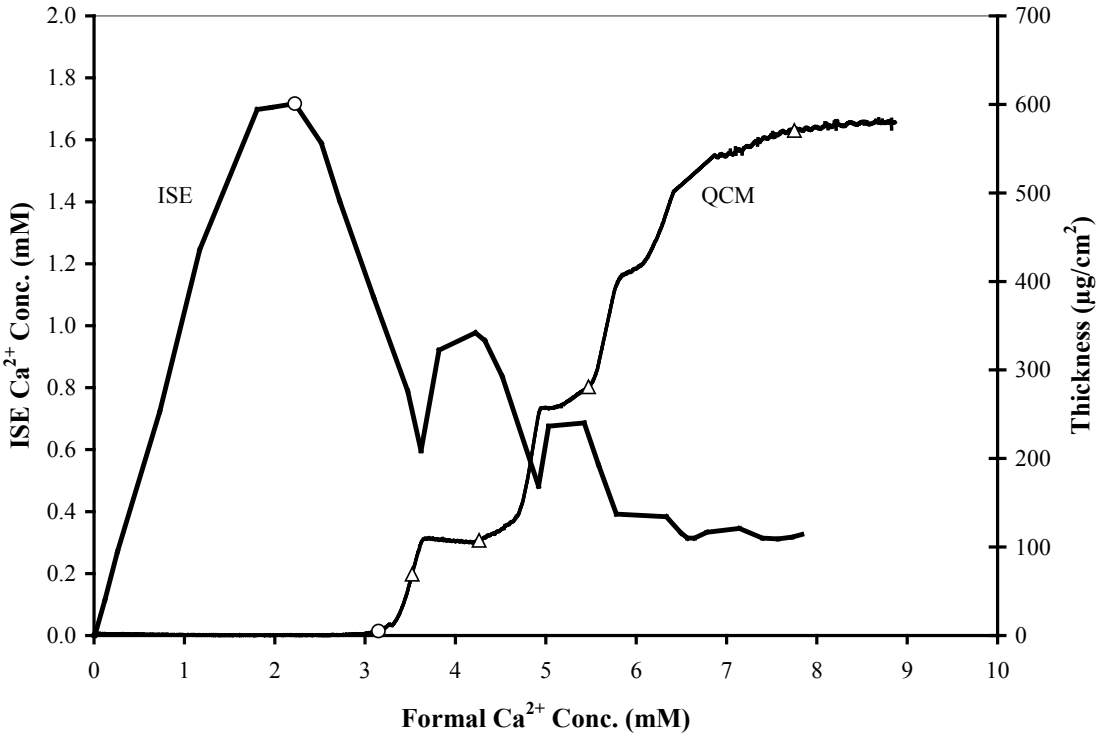

Figure 6.11 Dissolved Ca^{2+} concentration as determined via the ISE probe in a crystal growth experiment using 8ppm of 50:50 3,400:75,000 M_w ATRP PAA mixture as inhibitor. QCM thickness measurement is shown for reference on secondary axis. Points at which SEM samples were taken (and shown in Figure 6.13) are denoted by open triangles (Δ). Critical calcium concentrations as determined using the two different monitoring methods are shown as open circles(○) on their corresponding plots.

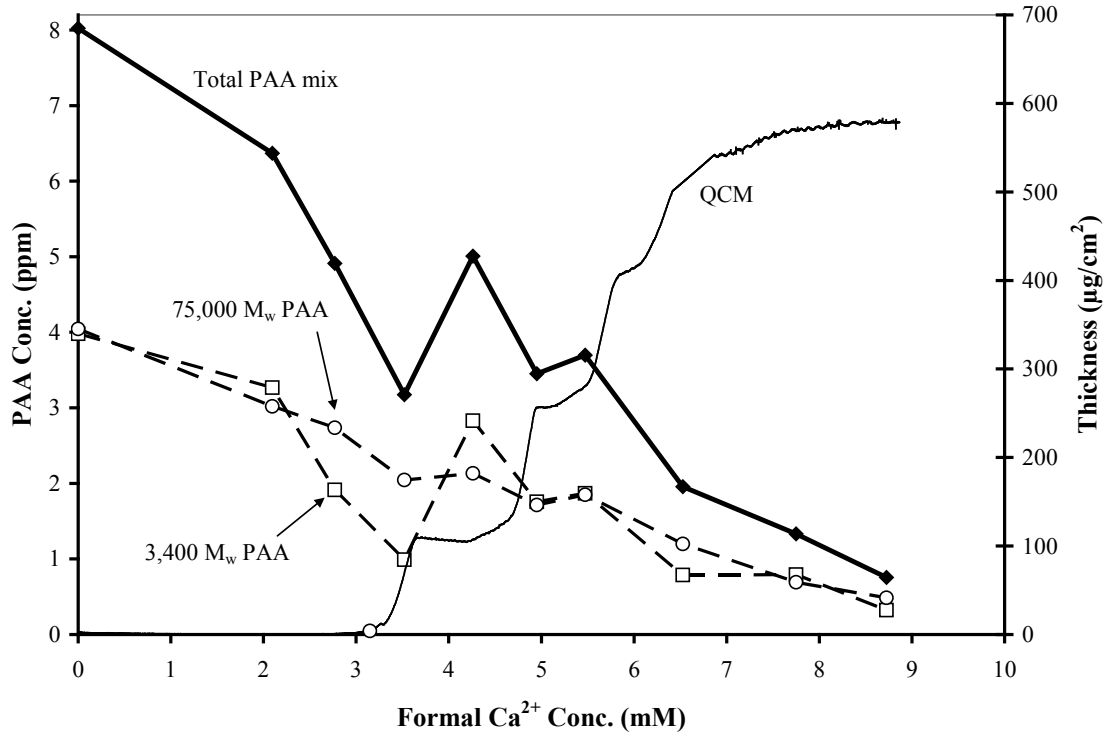

Figure 6.12 Dissolved PAA concentrations as determined via SEC in crystal growth experiment using 8ppm of 50:50 3,400:75,000 M_w ATRP PAA mixture as inhibitor. Total PAA (♦) along with the individual 3,400 (□) and 75,000 (○) M_w PAA concentrations are shown with respect to formal Ca^{2+} concentration. The QCM data is shown for reference.

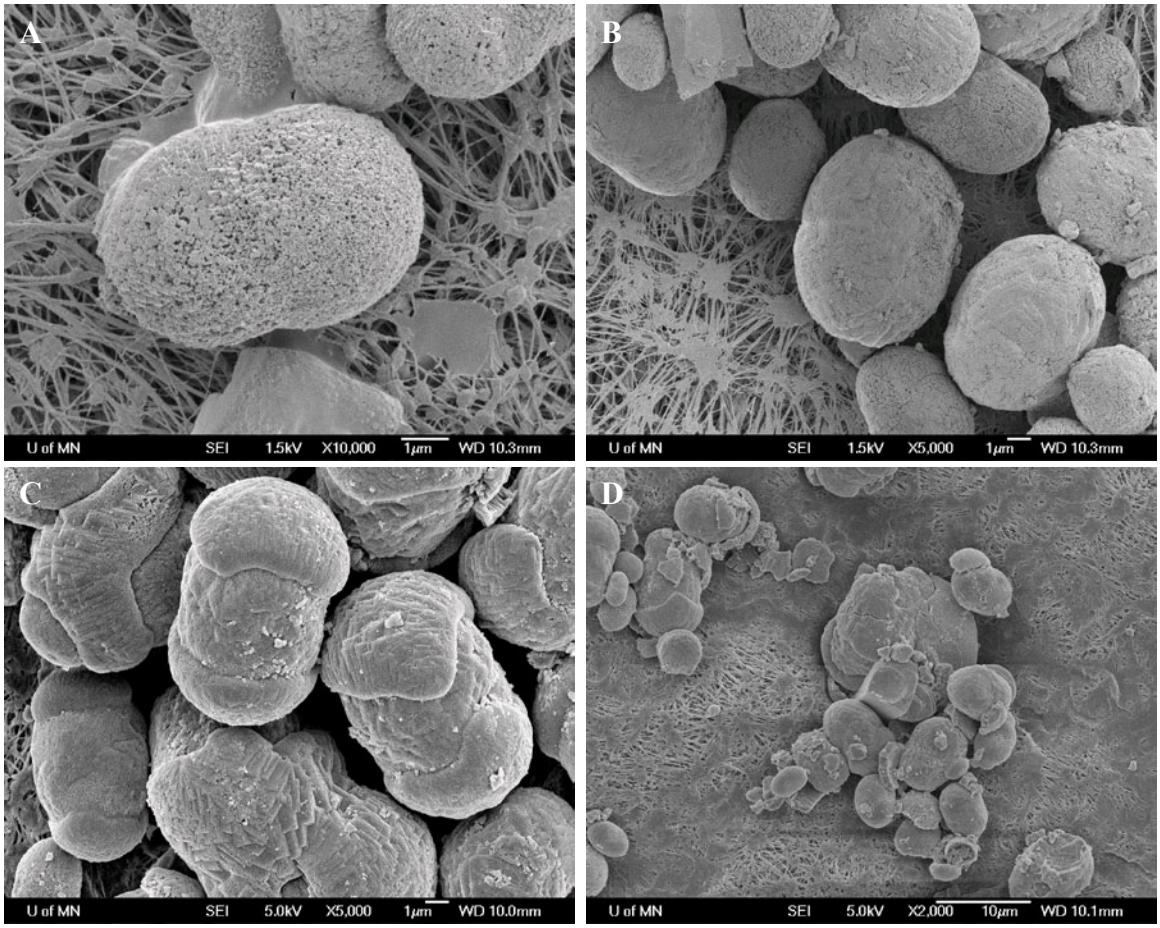

Figure 6.13 SEM images of $CaCO_3$ crystals present at Ca^{2+} formal concentrations of 3.5 (A), 4.3 (B), 5.5 (C), and 7.8 (D) mM from Figures 6.12 & 6.13.

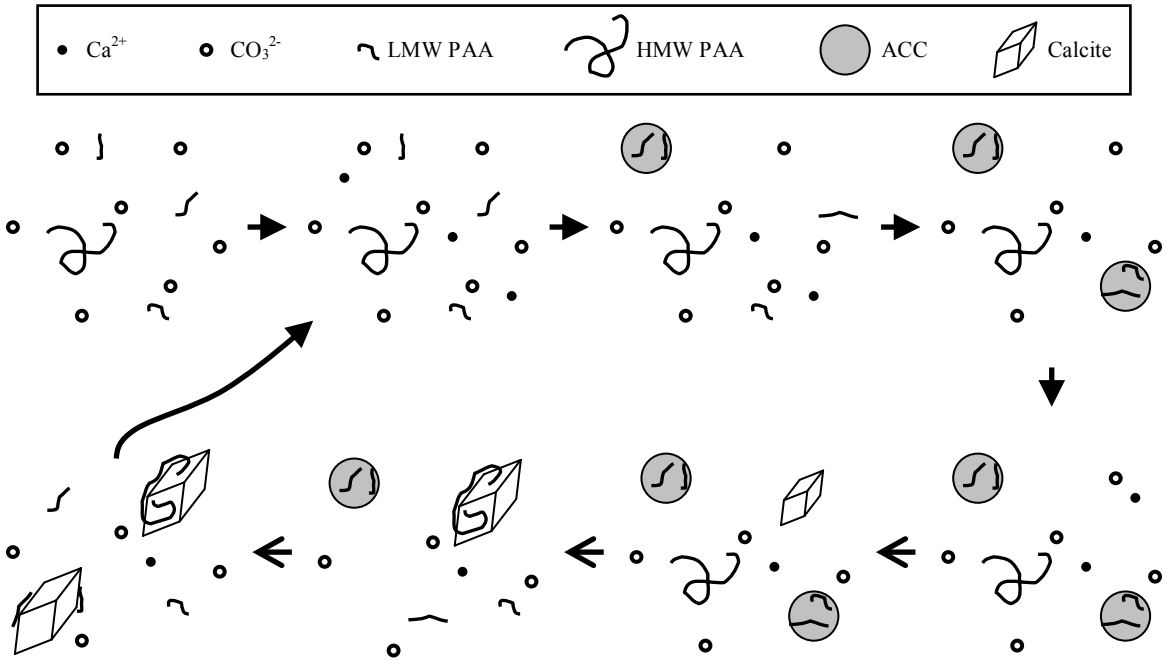

Figure 6.14 Proposed schematic of nucleation and growth of calcite phase at the expense of the ACC phase. Top row proceeds with addition of Ca^{2+} to the solution (forming stabilized ACC). Bottom row (denoted by open arrows) does not necessarily require Ca^{2+} addition in order to proceed. Once the calcite phase has depleted the calcium from the ACC phase and the solution returns to only saturated levels, the cycle can repeat.

Chapter 7 – Final Conclusions and Future Work

Summary

The basis for this thesis work was definitely grounded in the specific application of poly(acrylic acid) (PAA) as an antiscalant in the wood chip digestion and black liquor evaporation process units of the kraft pulping process. In particular, the molecular weight effect of the PAA in terms of inhibition performance was investigated over a broad range of practical and fundamental experiments. The synergistic tie between industrial scale inhibition and biomineralization research was also discussed and utilized by the end of this manuscript.

Empirically determined polymeric antiscalants already in use by the pulp and paper industry (commonly employing monomer residues with carboxylic acid functional groups) were used in batch pulping experiments closely resembling actual conditions in the kraft pulping mills. A molecular weight dependence of these polymeric antiscalants was found to be one of the more important aspects upon $CaCO_3$ scale inhibition at these high pH, temperature, and chemical concentration levels. An optimal M_w around 10,000 g/mol was observed for the antiscalant products in these kraft digester conditions. Slightly simpler Parr bomb experiments where the number and concentration of chemical components was decreased from the digester experiments yielded similar results. These experiments mimicking the temperature profile seen by black liquor in the condensers expressed an optimal M_w value of around and below 20,000 g/mol. It became clear that it was necessary to focus on the typical copolymer base, PAA, in order to distinguish molecular weight effects from effects due to changing the polymer composition.

Nucleation and crystal growth experiments using focused beam reflectance microscopy (FBRM) were utilized with a series of Na-PAA/PAA homopolymer commercial samples. Again, the optimal M_w range of 10,000 g/mol was observed although resulting dose-performance curves suggested an averaging effect of different MW species in these polydisperse samples. It was also shown that a noticeable difference in the mechanism of inhibition (or at least in form of nucleation expression)

occurred around an initial dosage concentration of 8 mg/L of PAA (active acid). At concentrations above this critical concentration, crystals nucleated and remained dispersed in the solution. It now became clear that monodispersed PAA samples were needed along with more fundamental adsorption studies in order to elucidate the mechanism by which the PAA inhibited $CaCO_3$ precipitation.

Relatively monodisperse PAA samples (with nominal PDI $\leq$ 1.3) were synthesized using atom transfer radical polymerization (ATRP) of poly(*t*-butyl acrylate) (PtBA) samples which were then hydrolyzed to PAA. Complete conversion of PtBA to PAA proved difficult due to the large change in lyophilicity upon removing the protective *t*-butyl "cap" but was eventually accomplished via multiple hydrolysis reactions with trifluoroacetic acid (TFA) in dichloromethane (DCM). Final PAA samples spanned a range of M_w values from less than 3,000 to more than 100,000 g/mol.

Isotherm studies involving the adsorption of polydisperse Na-PAA/PAA and relatively monodisperse ATRP PAA onto calcite surfaces in high pH (pH = 12) were conducted in order to isolate their adsorption behavior from nucleation and growth inhibition behavior. It was shown that independent of crystal growth (static surfaces) PAA adsorbs to calcite faces without dependence on MW. The high affinity adsorption isotherms yield plateau concentrations (after 24 hours) of 0.43 mg/m^2 which suggests that the PAA adsorbs in a flat conformation with each monomer residual occupying 27.8 Å^2 of calcite surface. The only conclusive effect of MW observed in the adsorption process was the preference for lower MW species to adsorb when competition of a polydisperse sample's MW species were present. This preference was found to be reversible in the sense that prolonged periods of time (~ 4 days) allowed for the more energetically favorable case of higher MW species adsorption to begin replacing the lower MW species on the surface with pieces of the higher MW species. This replacement of lower MW species with higher MW species was shown to proceed on a 1-to-1 molecular basis. The accumulation of these isotherm results suggested that the MW effects upon $CaCO_3$ inhibition were not necessarily due to differences in adsorption rates of the different species, but at least due to adsorption preference (of the lower MW species). More information on the scale-

prone system as a whole was required to further investigate the mechanisms involved in the MW dependence.

In addition to the FBRM monitored $CaCO_3$ nucleation and growth experiments conducted on the polydisperse commercial samples discussed earlier, a quartz crystal microbalance (QCM) was added for monitoring scale deposits. Also, the relatively monodisperse samples were examined with regards to inhibition performance. The results clearly expressed a distinction between high and low (distinction at 10,000 g/mol) MW performance along with a change in efficacy located at ~8 ppm initial dosage concentration of PAA. Particularly, the change in efficacy from a relatively high to low rate at the critical concentration level suggested a change in the mechanism of inhibition. This mechanism shift was explored with the aid of a number of different techniques used to track the changes not only in the solids content of the system, but also the PAA and Ca^{2+} concentrations in the solution phase throughout growth of substantial amounts of $CaCO_3$ particles. The results suggested the presence of a separate $CaCO_3$ phase prior to the precipitation of the larger calcite particles typically seen in scale formations. This precursor phase was attributed to PAA stabilized ACC which could then remain dispersed in solution but eventually decreased the amount and efficacy (due to the lower MW preference for ACC) of the polymer antiscalant left in solution. It was proposed that this decrease in the inhibitory effect of the solution phase PAA then allowed for calcite nucleation and growth with the use of the ACC/PAA particles as reservoirs of Ca^{2+} for the more energetically stable calcite particles.

This outlook on both the effects of MW and the change its influence has on inhibition mechanisms are useful not only for the application and design of polymer antiscalants in the kraft pulping industry but also to the antiscalant industry as a whole and even the biomineralization field which focuses on the control of crystal growth rather than simply the inhibition of it.

Future work

1. Investigate the influence of additional monomer residues on scale inhibition and their *independence* upon adsorption to calcite surfaces.

2. Determine if the addition of a templating polymer additive to a slurry of ACC/PAA can begin templated (and organized) precipitation of the more stable polymorphs of $CaCO_3$ such as aragonite or calcite to develop composite materials mimicking nacre.

Bibliography

1. Biermann, Christopher J.; In *Essentials of Pulping and Papermaking*; Academic Press, Inc.: San Diego, CA, 1993.
2. Green, R. P.; Hough, G., Eds.; In *Chemical Recovery in the Alkaline Pulping Processes;* TAPPI PRESS: Atlanta, GA 30348-5113, USA, 1992; , pp 196.
3. Berry, L. *Tappi J.* **1966**, *49* (4), 68A.
4. Hartler, N.; Libert, J. *Sven. Papperstidn.* **1972**, *75* (2), 65.
5. Hartler, N.; Libert, J. *Sven. Papperstidn.* **1973**, *76* (9), 12.
6. Markham, L. D.; Bryce, J. R. In *Formation of Calcium Carbonate Scale in a Kamyr Digester*, Proceedings of the Pulping Conference; TAPPI Press: Atlanta, GA, 1979.
7. Markham, L. D.; Bryce, J. R. *Tappi J.* **1980**, *63* (4), 125.
8. Schmidl, W.; Frederick, W. J. In *Current Trends in Evaporator Fouling*, Proceedings of the International Chemical Recovery Conference, Tampa, FL, June 1-4, 1998; TAPPI Press: Atlanta, GA, 1998.
9. Weyl, P. K. *Geochim. Cosmochim. Acta* **1959**, *17*, 214.
10. Cowan, J. C.; Weintritt, D. J. In *Water-Formed Scale Deposits;* Gulf Publishing Company: Houston, Texas, 1976; , pp 8, 93, 255-257, 261-262, 596.
11. Payen, A. *Dinglers Polytech. J.* **1823**, *10*, 254.
12. Hatch, G. B.; Rice, O. *Ind. Eng. Chem.* **1939***, 31*, 51.
13. McKenna, B. J.; Waite, H.; Stucky, G. D. *Cryst. Growth Des.* **2009**, *9* (10), 4335.
14. Guo, J.; Severtson, S. J. *Ind. Eng. Chem. Res.* **2003***, 42*, 3480.
15. Mann, S.; Didymus, J. M.; Sanderson, N. P.; Heywood, B. R. *J. Chem. Soc., Faraday Trans.* **1990***, 86* (10), 1873.
16. Didymus, J. M.; Mann, S. *Langmuir* **1995***, 11*, 3130.
17. Didymus, J. M.; Oliver, P.; Mann, S.; Hauschka, P. V.; Westbroek, P. *J. Chem. Soc., Faraday Trans.* **1993***, 89* (15), 2891.
18. Heywood, B. R.; Rajam, S.; Mann, S. *J. Chem. Soc., Faraday Trans.* **1991***, 87*, 735.
19. Rajam, S.; Heywood, B. R.; Walker, Justin B. A.; Mann, S. *J. Chem. Soc., Faraday Trans.* **1991***, 87*, 727.
20. Gill, J. S.; Varsanik, R. G. *J. Cryst. Growth* **1986***, 76*, 57.
21. Kitano, Y.; Hood, D. W. *Geochim. Cosmochim. Acta* **1965***, 29*, 29.
22. Wilken, G. *Desalination* **1980**, *33* (2), 201.
23. Öner, M.; Do, Ö.; Öner, G. *J. Cryst. Growth* **1998**, *186* (3), 427.
24. Severtson, S.; Guo, J. *J. Colloid Interf. Sci.* **2002**, *249*, 423.
25. Plummer, L. N.; Busenberg, E. *Geochim. Cosmochim. Acta* **1982**, *46*, 1011.
26. Somerdijk, N. A. J. M.; de With, G. *Chem. Rev. (Washington, DC, U. S.)* **2008**, *108* (11), 4499.
27. Pichon, B. P.; Bomans, P. H. H.; Frederik, P. M.; Sommerdijk, N. A. J. M. *J. Am. Chem. Soc.* **2008**, *130* (12), 4034.

28. Addadi, L.; Raz, S.; Weiner, S. *Adv. Mater. (Weinheim, Ger.)* **2003**, *15* (12), 959.
29. Mann, S. In *Biomineralization: Principles and Concepts in Bioinorganic Materials Chemistry;* Oxford University Press, New York, p 63.
30. Tompa, A. S.; Watabe, N. *Calcif. Tissue Res.* **1976**, *22* (1), 159.
31. Hartler, N.; Libert, J. *Sven. Papperstidn.* **1973,** *76* (12), 454.
32. Adams, T. *Tappi J.* **2001**, *84* (6), 70.
33. Severtson, S. J.; Duggirala, P. Y.; Carter, P. W.; Reed, P. E. *Tappi J.* **1999**, *82* (6), 167.
34. Westervelt, H. H.; Frederick, W. J.; Malcolm, E. W.; Easty, D. B. *Tappi J.* **1982**, *65* (5), 179.
35. Guo, J. Inhibition of Calcium Carbonate Nucleation with Organic Additives. Ph. D. Thesis, University of Minnesota, 2004.
36. Koch, P., Ed. *Utilization of the Southern Pines* (Agric. Handbook 420); Vol. 1, US Department of Agriculture: Washington, DC, 1972; pp 501, 220.
37. Koch, P., Ed. *Utilization Hardwoods Growing on Southern Pine Sites* (Agric. Handbook 605); Vol. 1, US Department of Agriculture: Washington, DC, 1985; pp 443-445.
38. Guo, J.; Severtson, S. J. *Tappi J.* **2002**, *1* (8), 21.
39. Guo, J.; Severtson, S. J. *Ind. Eng. Chem. Res.* **2004**, *43* (17), 5411.
40. Dirksen, J. A.; Ring, T. A. *Chem. Eng. Sci.* **1991**, *46*, 2389.
41. Mulin, J. W. *Crystallization*, 4th ed.; Butterworth Heinemann: Oxford, 2001; Chapter 5.
42. Smith, B. R.; Sweet, F. *Desalination* **1971**, *9*, 277.
43. Reddy, M. M.; Nancollas, G. H. *Desalination* **1973**, *12*, 61.
44. Loy, J. E.; Guo, J.; Severtson, S. J. *Ind. Eng. Chem. Res.* **2004**, *43*, 1882.
45. Silbey, R. J.; Alberty, R. A.; In *Physical Chemistry*, 3rd ed.; John Wiley & Sons, Inc.: New York, 2001; Chapter 18.
46. Persinski, L. J.; Walker, J. L.; Boffardi, B. P. U. S. Patent 4,640,793, February 13, 1987.
47. Duggirala, P. Y.; Morris, J. D.; Reed, P. E.; Severtson, S. J. U. S. Patent 6,146,495, November 14, 2000.
48. Duggirala, P. Y.; Morris, J. D.; Reed, P. E.; Severtson, S. J. U. S. Patent Application 9/799,285, Mar 5, 2001.
49. Duggirala, P. Y.; Morris, J. D.; Reed, P. E.; Severtson, S. J. U. S. Patent 6,232,419, May 15, 2001.
50. Duggirala, P. Y.; Morris, J. D.; Reed, P. E.; Severtson, S. J. U. S. Patent 6,235,152, May 22, 2001.
51. Gurkaynak, A.; Tubert, F.; Yang, J.; Matyas, J; Spencer, J. L.; Gryte, C. C. *J. Polym. Sci., Part A: Polym. Chem.* **1996**, *34*, 349.
52. Shaheen, E. I.; Dixit, S. N. S. *Desalination* **1973**, *13* (2), 187.
53. Yuchi, A.; Gotoh, Y.; Itoh, S. *Anal. Chim. Acta* **2007**, *594* (2), 199.
54. Vill, W. A. *Pulp Pap.* **1967**, *41* (13), 42.
55. Ruf, A.; Worlitschek, J.; Mazzotti, M. *Part. Part. Syst. Charact.* **2000**, *17*, 167.

56. Worlitschek, J.; Mazzotti, M. *Cryst. Growth Des.* **2004**, *4* (5), 891.
57. Worlitschek, J.; Hocker, T.; Mazzotti. M. *Part. Part. Syst. Charact.* **2005**, *22*, 81.
58. Li, M.; Wilkinson, D. *Chem. Eng. Sci.* **2005**, *60* (12), 3251.
59. Li, M.; Wilkinson, D. *Chem. Eng. Sci.* **2005**, *60* (18), 4992.
60. Li, M.; Wilkinson, D.; Patchigolla, K. *Part. Part. Syst. Charact.* **2006**, *23*, 170.
61. Worlitschek, J.; Mazzotti, M. *Part. Part. Syst. Charact.* **2003**, *20*, 12.
62. Shukla, A.; Prakash, A.; Rohani, S. *Chem. Eng. Sci.* **2010**, *65* (10), 3072.
63. Sperling. L. H. Molecular Weights and Sizes. In *Introduction to Physical Polymer Science*, 3rd ed.; John Wiley & Sons: New York, NY, 2001.
64. Hiemenz, P. C. Addition or Chain-Growth Polymerization. In *Polymer Chemistry: The Basic Concepts*; Marcel Dekker, Inc.: New York, NY, 1984.
65. Nicholas, P. P.; Amjad, Z. U. S. Patent 5,658,465, August 19, 1997.
66. Nicholas, P. P.; Amjad, Z. European Patent EP0881991, May 3, 2000.
67. Matyjaszewski, K.; Xia, J. *Chem. Rev. (Washington, DC, U. S.)* **2001**, *101* (9), 2921.
68. Kamigaito, M.; Ando, T.; Sawamoto, M. *Chem. Rev. (Washington, DC, U. S.)* **2001**, *101* (12), 3689.
69. Loiseau, J.; Doërr, N.; Suau, J. M.; Egraz, J. B.; Llauro, M. F.; Ladavière, C.; Claverie, J. *Macromolecules (Washington, DC, U. S.)* **2003**, *36*, 3066.
70. Chiefari, J.; Chong, Y. K.; Ercole, F.; Krstina, J.; Jeffery, J.; Le, T. P. T.; Mayadunne, R. T. A.; Meijs, G. F.; Moad, C. L.; Moad, G.; Rizzardo, E.; Thang, S. H. *Macromolecules (Washington, DC, U. S.)* **1998**, *31*, 5559.
71. Benoit, D.; Chaplinski, V.; Braslau, R.; Hawker, C. J. *J. Am. Chem. Soc.* **1999**, *121*, 3904.
72. Colombani, O.; Ruppel, M.; Schubert, F.; Zettl, H.; Pergushov, D.; Müller, A. *Macromolecules (Washington, DC, U. S.)* **2007**, *40*, 4338.
73. He, L.; Zhang, Y.; Ren, L.; Chen, Y.; Wei, H.; Wang, D. *Macromol. Chem. Phys.* **2006**, *207*, 684.
74. Hou, S.; Chaikof, E. L.; Taton, D.; Gnanou, Y. *Macromolecules (Washington, DC, U. S.)* **2003**, *36*, 3874.
75. Liu, C.; Wang, G.; Zhang, Y.; Huang, J. *J. Appl. Polym. Sci.* **2008**, *108*, 777.
76. Rathfon, J. M.; Tew, G. N. *Polymer* **2008**, *49*, 1761.
77. Yang, H.; Su, Y.; Zhu, H.; Zhu, H.; Xie, B.; Zhao, Y.; Chen, Y.; Wang, D. *Polymer* **2007**, *48*, 4344.
78. Ma, Q.; Wooley, K. L. *J. Pol. Sci. Pol. Chem.* **2000**, *38*, 4805.
79. Ladavière, C.; Dörr, N.; Claverie, J. *Macromolecules (Washington, DC, U. S.)* **2001**, *34*, 5370.
80. Kawabe, H.; Yanagita, M.; *Bull. Chem. Soc. Jpn.* **1971**, *44* (2), 310.
81. Li, P.; Li, Z.; Huang, J. *Macromolecules (Washington, DC, U. S.)* **2007**, *40*, 491.
82. Järnström, L. *Nord. Pulp Pap. Res. J.* **1993**, *8* (1), 27.
83. Mäkinen, M.; Laakso, A.; Oy, J. *Nord. Pulp Pap. Res. J.* **1993**, *8* (1), 59.

84. Geffroy, C.; Persello, J.; Foissy, A.; Cabane, B.; Tournilhac, F. *Oil Gas Sci. Technol.* **1997**, *52* (2), 183.
85. de Vreugd, C. H.; ter Horst, J. H.; Durville, P. F. M.; Witkamp, G. J.; van Rosmalen, G. M. *Colloids Surf., A* **1999**, *154*, 259.
86. Fleer, G. J.; Cohen Stuart, M. A.; Scheutjens, J. M. H. M.; Cosgrove, T.; Vincent, B. In *Polymers at Interfaces;* Chapman & Hall: London, UK, 1993.
87. Rouquerol, F.; Rouquerol, J.; Sing, K. In *Adsorption by Powders and Porous Solids*; Academic Press: San Diego, CA, 1999.
88. Cohen Stuart, M. A.; *Nord. Pulp Pap. Res. J.* **1993**, *8* (1), 10.
89. Dijt, J. C.; Cohen Stuart, M. A.; Fleer, G. J. *Macromolecules (Washington, DC, U. S.)* **1994**, *27* (12), 3219.
90. Dijt, J. C.; Cohen Stuart, M. A.; Fleer, G. J. *Macromolecules (Washington, DC, U. S.)* **1992**, *25* (20), 5416.
91. Dijt, J. C.; Cohen Stuart, M. A.; Fleer, G. J. *Macromolecules (Washington, DC, U. S.)* **1994**, *27* (12), 3207.
92. Zuman, P.; Szafranski, W. *Anal. Chem. (Washington, DC, U. S.)* **1976**, *48* (14), 2162.
93. Koopal, L. K. *J. Colloid Interf. Sci.* **1981**, *83* (1), 116.
94. Hlady, V.; Lyklema, J.; Fleer, G. J. *J. Colloid Interf. Sci.* **1982**, *87* (2), 395.
95. Cohen Stuart, M. A.; Fleer, G. J.; Lyklema, J.; Norde, W.; Scheutjens, J. M. H. M. *Adv. Colloid Interface Sci.* **1991***, 34*, 477.
96. Kunjappu, J. T.; Somasundaran, P.; Sivadasan, K. *Colloids Surf., A* **1995**, *97*, 101.
97. Tjipangandjara, K.; Huang, Y.; Somasundaran, P.; Turro, N. *Colloids Surf.* **1990***, 44*, 229.
98. Giannimaras, E. K.; Koutsoukos, P. G. *J. Colloid Interf. Sci.* **1987**, *116* (2), 423.
99. Huang, S.; Naka, K.; Chujo, Y. *Langmuir* **2007**, *23* (24), 12086.
100. Xu, X.; Cai, A.; Liu, R.; Pan, H.; Tang, R.; Cho, K. *J. Cryst. Growth* **2008**, *310* (16), 3779.
101. Donners, J. J. J. M.; Heywood, B. R.; Meijer, E. W.; Nolte, R. J. M.; Roman, C. Schenning, A. P. H. J.; Sommerdijk, N. A. J. M. *Chem. Commun. (Cambridge, U. K.)* **2000**, 1937.
102. Yu, S.; Cölfen, H. *J. Mater. Chem.* **2004**, *14* (14), 2124.
103. Xu, X.; Han, J. T.; Cho, K. *Langmuir* **2005**, *21* (11), 4801.
104. Faatz, M.; Gröhn, F.; Wegner, G. *Adv. Mater. (Weinheim, Ger.)* **2004**, *16* (12), 996.
105. Benes, E.; Schmid, M.; Thorn, G. *Thin Solid Films* **1989**, *174* (1), 307.
106. Lu, C. *J. Vac. Sci. Technol. (N. Y., NY, U. S.)* **1975**, *12* (1), 578.
107. Sauerbrey, G. *Z. Physik* **1959**, *155*, 206.
108. Lu, C.; Lewis, O. *J. Appl. Phys.* **1972**, *43* (11), 4385.
109. Addadi, L.; Joester, D.; Nudelman, F.; Weiner, S. *Chem. --Eur. J.* **2006**, *12* (4), 980.